Orbital orientations of exoplanets

Stellar spin-orbit angles as a window to planet formation and evolution

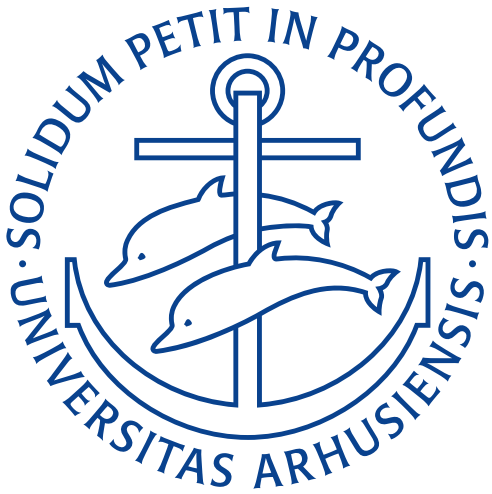

Maria Hjorth

PhD Thesis
2nd September 2019

Supervisor: Simon Albrecht

Stellar Astrophysics Centre
Department of Physics and Astronomy
Aarhus University

Til Henrik

Preface

In this thesis I present the work and research carried out during my PhD studies. These studies have mainly taken place at the Stellar Astrophysics Centre at Aarhus University, with a three-month interim at Tokyo Institute of Technology in Japan. Through my three years as a PhD-student I have had the good fortune of working with some amazing people, and have learned a great deal about science, academia and life. Though I am not continuing my career in academia, I am very grateful to have had the opportunity to perform research and contributing to the scientific field of exoplanets. I would like to thank all the people who have made this a reality.

First I would like to thank my thesis supervisor Simon. Thank you for always having your door open for discussions and problem solving, and for helping me whenever I have gotten stuck in my work. I am very grateful to you for always striving to better me and encourage me at times when academia or life as a PhD-student has been tough. You have not only advised me on research topics, but also taken an active interest in my life and future. Thank you for guiding me through the sometimes convoluted path of a PhD.

I would also like to thank Teru; my host in Japan. Since I started my studies on spin-orbit angles I have always admired you and your research, and felt very lucky when the opportunity to work with you arose. You are not only a great scientist, but also a great person, who has helped me with my research and helped me feel at home in Japan. Thank you.

I am very grateful to you Caro for being my mentor and friend throughout my academic career. You have always been there to lend an ear whenever I have had something on my mind, be it professional or personal. I am very grateful for your support, guidance and friendship.

I am very happy to have been an employee at the Stellar Astrophysics Centre. Thank you to all of my colleagues for an excellent work environment. Our daily coffee breaks, Friday bars and biweekly pub quizzes have made for a fun and enjoyable workplace. I also wish to thank my former and current office mates – both at SAC and at Tokyo Tech – for making it a joy to come to work each morning. Thank you to CLOC for keeping me as a member of the Christmas

Office; it has been a delight planning and organising the annual Christmas Lunch with you. I would also like to thank my exoplanet-colleagues; it has been very rewarding to be a part of the Exoplanet Group of SAC and the Sato-san Group at Tokyo Tech. A special thanks to Emil, Andreas, Anders and Lee, who have travelled to remote locations to conduct astronomical observations on my behalf or assisted me during such trips.

Thank you to my friends outside of work. In particular I would like to thank Simone, Helene, Anne Mette, Jani, Bodil and Jonatan: I really appreciate your support of me and your understanding of the time constraints a PhD can put on a social life. Thank you to the people of Morgenmadsministeriet for being a social pillar and for keeping me sane during the thesis writing process.

Mor, far, Maiken, Michelle og Palle: Tusind tak for jeres store støtte og kærlighed. Tak fordi I altid har været der for mig, for jeres ubetingede opbakning og for at lytte til mig, selv når jeg snakker om uforståelige astronomi-emner. Jeg er ubeskrivelig taknemmelig for alt jeres hjælp.

Henrik, my love. I am forever grateful for your huge amount of help and encouragement throughout my PhD, and for all of your hard work during both my stay in Japan and the thesis writing process. I could not have completed my thesis without your love and support. Thank you for being my rock, and for always having faith in me, even when I doubt myself.

Abstract

A quarter of a century ago the first planet outside of the Solar System was detected. With an orbital period of a few days, this discovery immediately puzzled astronomers. How could such a large gas giant be formed so close to the violent environment of it's host star? This thesis attempts to illuminate the secrets of planet formation by studying the orbital orientation of several different system configurations. Today we believe that these "hot Jupiters" formed further out, but then migrated inwards to their current location. However, the history behind this relocation is still a mystery, with two major contenders: disk migration and/or high-eccentricity migration. A way to distinguishing between these two origin scenarios is to measure the spin-orbit angle of Jupiters with hot host stars, multi-planet systems or planetary systems containing warm Jupiters.

The first few chapters contain a general introduction to the scientific field of exoplanets, as well as an explanation of the current state of the research into planet formation. It is presented how spin-orbit observations can be used to reveal the dynamic history of giant planets, and how this is measured in practice through the Rossiter-McLaughlin effect. The use of the Rossiter-McLaughlin effect is demonstrated on MASCARA-3, a system containing a hot Jupiter orbiting a hot host star. We report the detection of this system, and use a combination of the Doppler shadow and velocity anomaly techniques to establish it's alignment. The hot nature of it's host star combined with the low spin-orbit angle points towards the planet originating from disk migration. We also introduce the discovery and characterisation of K2-290, which is a triple-star, multi-planet system consisting of a mini-Neptune and a warm Jupiter. We present observations of the velocity anomaly for both planets, introducing the first case of obtaining the Rossiter-McLaughlin signal for several planets in the same system. The data reveals the first retrograde multi-planet system, and provides the first direct evidence of a planet originating from a primordial misaligned proto-planetary disk. Finally we display the Rossiter-McLaughlin measurements of three planets in the M-dwarf system of Trappist-1, all transiting on the same night. The data indicates an aligned system, and we show how a preliminary investigation suggests our velocity anomaly model also applies to M-dwarf systems. Lastly we conclude that disk migration might be an alternative explanation for the misalignment of some giant planets, and discuss the bright future of spin-orbit and formation studies.

Resumé

Det er et kvart århundrede siden vi opdagede den første planet uden for Solsystemet. Med en omløbstid på få dage, forundrede denne straks astronomer. Hvordan kunne en gasplanet dannes så tæt på stjernens voldsomme omgivelser? Denne afhandling forsøger at kaste lys på hemmelighederne bag planetdannelse ved at studere banerne af forskellige planetsystemer. I dag tror vi at disse "hede Jupitere" blev dannet længere væk, for sidenhen at migrere indad til deres nuværende placering. Historien bag deres udflytning er stadigvæk et mysterium, men med to forslag: migration gennem den protoplanetare disk og migration pga. en høj eccentricitet. En måde at skelne på, er at studere banen af Jupitere omkring varme stjerner, såvel som fler-planetsystemer og systemer med en varm Jupiter.

De første kapitler indeholder en introduktion til exoplanetvidenskab og en præsentation af den nuværende forskning i planetdannelse. Det bliver præsenteret hvordan observationer af rotation-bane-vinkler kan bruges til at afsløre dynamikhistorien for gasplaneter, og hvordan denne måles gennem Rossiter-McLaughlin-effekten. Brugen af denne effekt demonstreres på MASCARA-3; et system med en hed Jupiter kredsende om en varm stjerne. Vi beretter om dennes opdagelse, og viser at planeten bevæger sig i samme retning som sin stjernes rotation. Dette – kombineret med stjernens høje temperatur – tyder på at planeten stammer fra migration gennem sin disk. Vi introducerer også opdagelsen og karakteriseringen af K2-290; et tripel-stjernesystem med en mini-Neptun og en varm Jupiter. Vi præsenterer observationer af den spektroskopiske formørkelse for begge planeter; det første eksempel på målinger af Rossiter-McLaughlin-effekten for flere planeter i det samme planetsystem. Dataene afslører for første gang et fler-planetsystem der bevæger sig modsat stjernens rotation, og vi retfærdiggører at dette er det første direkte bevis på en planet som stammer fra en skæv proto-planetarisk disk. Endeligt viser vi Rossiter-McLaughlin-målinger af tre planeter i det røde dværgsystem Trappist-1, som alle formørkede stjernen den samme nat. Dataene viser at planeterne bevæger sig i samme retning som stjernens rotation. Vi viser desuden hvordan foreløbige beregninger tyder på at vores modeller også gælder for planeter om røde dværge. Til sidst konkluderer vi at migration gennem en protoplanetar disk kan være en alternativ forklaring på skævheden af nogle gasplanetsystemer, og vi diskuterer fremtiden for forskning indenfor rotation-bane-vinkler og planetdannelse, såvel som exoplanetvidenskab i det hele taget.

Contents

1

Introduction

Gazing at the night sky, you cannot help but feel a sense of calm. The stars, the Moon, the planets; all appear to be ever-present and their orbits never-changing. Even after we are gone, they will keep illuminating the darkness; day after day, decade after decade. As the stars trail across the sky, the cosmos seems peaceful and static. In reality, the Universe is anything but calm: Everyday galaxies are merging, stars are dying, planets are forming. Dynamical interactions continuously sculpts the inhabitants of space; be it the collapse of a molecular cloud giving birth to stars, or the collision of planetesimals creating planetary systems. Both during and after their construction, dynamics might continue to influence the shape and orbit of these extra-solar planets or *exoplanets*.

Exoplanets are worlds outside our Solar System. Their existence was long pondered by philosophers and scientists alike: while ancient Greeks like Epicurus freely debated the possibility of an infinite number of worlds, the same notion proved fatal for Renaissance philosopher Giordano Bruno (Bruno, 1584), who was burned at the stake as a heretic. During the Age of Enlightenment Newton argued for the presence of planetary systems similar to our own (Newton, 1713), and by the 19$^{\text{th}}$ Century modern astronomers were actively searching for exoplanets (Jacob, 1855). Though the presence of an exoplanet could in hindsight be inferred from 1917-observations of a white dwarf (Zuckerman, 2015), it was not until 1992 that we saw the first definite confirmation of the existence of extra-solar worlds, with the discovery of two planets orbiting a pulsar (Wolszczan and Frail, 1992). A few years later, the research field of exoplanets kicked off with the detection of 51 Peg b – the first discovery of an exoplanet orbiting a main-sequence star (Mayor and Queloz, 1995).

While the search for planets was ongoing throughout the 20$^{\text{th}}$ century, it was restricted by the technological limitations on telescopes and their instruments. Though the first 1992 detection was made by taking advantage of the precise timing of pulsars, subsequent discoveries were made through primarily photometry and spectroscopy observations. It was not until the 1970's invention of the CCD and the use of gas cell for wavelength calibration in spectrographs, that significant advancements were made (see Seager and Lissauer, 2010, for a brief historic review). This progress accelerated after the first discoveries, leading to

both major constructions and upgrades of ground-based spectrographs and observatories and to the launch of large-scaled exoplanet-focused space telescopes. These have not only played a large part in the detection of exoplanets, but also in their characterisation.

Discovery and characterisation of exoplanets

Today we know of 4044 planets distributed in 3004 planetary systems[1]. Since stars greatly outshine their planets, a vast majority of these have been detected through indirect methods. With the launch of space mission surveys such as *CoRoT*, *Kepler*, *K2* and *TESS*, the photometric transit method has become the most numerous technique, resulting in the discovery of more than 3/4th of the known planets. In this approach, the planet passing in front of its star will diminish the amount of light we receive. The shape, depth and duration of the resulting transit light curve can reveal e.g. the orbital inclination and the planetary radius. If we would like to know it's mass or orbital eccentricity, we can combine it with the radial-velocity (RV) method, of which a majority of the remaining planets have been discovered through. Here, we take advantage of the gravitational influence the planet has on its star, causing it to orbit their common center-of-mass. Due to the Doppler effect, the movement in our line-of-sight (the radial direction) leads to the displacement of the stellar spectral lines. Measurements of sub-meter precision shifts (i.e. Earth-like planets and orbits) have been made possible with the upgrade and invention of state-of-the-art spectrographs such as HARPS, HARPS-N, SUBARU and ESPRESSO.

The above techniques are not only applicable in the detection of exoplanets, but can also be used to characterise e.g. their host star, the planetary atmosphere and the orbital architecture. Combining knowledge on the individual systems with population studies has revealed a great deal about exoplanets in general: to name a few, we now know that almost all sun-like stars have planetary systems (Dressing and Charbonneau, 2013) and that small planets in multi-planet systems have low eccentricities (Van Eylen and Albrecht, 2015). In addition, the orbital orientation has been revealed for more than 100 planets[2], and can be deduced by e.g. performing spectroscopy during transit. This information is crucial for understanding the formation and evolution history of the planetary system, and will play a large part of this thesis.

Exoplanets and the Solar System

The Solar System contains eight planets: four inner rocky worlds and four outer gas giants. While the search for exoplanets has revealed Earthly worlds like Proxima b (Anglada-Escudé et al., 2016) – orbiting the closest star to Earth – and the seven planets in the Trappist-1 system (Gillon et al., 2016), it has also resulted in the detection of planets very different than what we know from

[1] exoplanets.nasa.gov, accessed 2019-09-02.
[2] https://www.astro.keele.ac.uk/jkt/tepcat/obliquity.html

the Solar system. Indeed, examining the distribution of these foreign worlds[3], the most common exoplanets discovered are super-Earths and mini-Neptunes, not present in our own neighbourhood. Another example is the very first 1995 exoplanet around a main-sequence star; a hot Jupiter. Though the Solar System contains the gas giants Jupiter and Saturn, they have orbital periods of 12 and 29 *years*, while 51 Peg b has an orbital period of 4 *days*. Today we know of almost 500 hot Jupiters, and have also discovered a few dozen of their colder relatives, the so-called warm Jupiters.

Even though astronomer Otto Struve already speculated the presence of such close in gas giants in the 1950's (Struve, 1952), the short orbital periods of the first exoplanets came as quite a surprise for the scientific community, which believed that systems with Jupiter-like exoplanets would resemble that of our own Solar System (Seager and Lissauer, 2010). This surprise arose mainly from the fact, that it is hard to explain how a gas giant could form in such close proximity to their host star. While we today believe they mostly formed further away from their star, *how* they arrived at their observed location is still a mystery. This question in particular and the topic of planet formation in general is one of the main motivations of the PhD thesis presented here, which has aimed at enhancing the knowledge on this by studying it's connection to orbital architecture. This has been done by obtaining spin-orbit (mis-)alignments in multi-planet, hot and warm Jupiter systems.

Thesis outline

In this thesis topics surrounding planet formation and orbital architecture is attempted illuminated by measuring the spin-orbit angle of different kind of exoplanetary systems through observations of the Rossiter-McLaughlin effect. This is done by focusing particular on systems with Jupiter-like planets as well as different multi-planet configurations.

In Chapter 2 details of the different planet formations and migration scenarios are presented. The general consensus of how giant planets are formed is explained, as well as a brief description of the basic physics and ideas behind disk migration and high-eccentricity migration. The scientific background behind the interest in the spin-orbit alignment is also given, with a detailed explanation of the connection between spin-orbit studies and migration methods. It is presented how extra observations of multi-planet or hot Jupiter systems might hold the key to understand the origin of hot Jupiters.

Chapter 3 deals with the technical aspects of obtaining the spin-orbit angle of a planetary system. It is explained how the Rossiter-McLaughlin effect can reveal the (mis-)alignment of systems through the velocity anomaly and Doppler Tomography techniques, and how these two approaches are modelled in practise. These models are put to the test in Chapter 4, which presents the discovery, characterisation and orbital architecture of the hot Jupiter system MASCARA-3.

[3] using e.g. `http://exoplanet.eu`.

A simultaneous expansion of both the multi-planet and warm Jupiter population is given in Chapter 5. Here the discovery and characterisation of K2-290 is introduced; a triple-star, multi-planet system containing a warm Jupiter and a mini-Neptune. Spin-orbit measurements of this system is presented in Chapter 6, which shows the first direct evidence of primordial misalignment together with the first Rossiter-McLaughlin publication of several planets in the same system and the first multi-planet system found to be retrograde.

Chapter 7 is about the very frontier of spin-orbit measurements. It deals with observations of spin-orbit angles of planets orbiting M-dwarfs in general and Trappist-1 in particular. Trappist-1 contains seven Earth-sized planets orbiting a slowly rotating M-dwarf. We show observations enclosing the Rossiter-McLaughlin signal for three of these planets during a single night, suggesting an aligned system and presents us with the smallest planets having a measured spin-orbit angle. We also show a preliminary numerical simulation of the Rossiter-McLaughlin effect in the Trappist-1 host star, showing that the analytic model from Chapter 3 is also suited for describing the signal in line-rich M-dwarfs.

An overall conclusion on the research carried out during this PhD is given in Chapter 8, which puts the findings into the context of orbital orientations measurements, planet formation and the origin of hot Jupiters. In addition, future prospects of alignment studies are presented, as well as the future of research into warm and hot Jupiters.

The basis of Chapter 4 and 5 are manuscripts which have been accepted in peer-reviewed journals (though the latter is not yet published), with only minor deviations (see each chapter for more details). Chapter 6 builds from an almost complete draft, which will be submitted in the near future. In accordance with GSST rules, parts of this thesis was also used in the progress report for the qualifying examination.

2

Formation and migration

2.1 Hot and warm Jupiters

Before describing the work done during this PhD, it will be beneficial to first present the terminology and examine the current scientific consensus on the origin of hot Jupiters. These planets are commonly defined as gas giants with masses $0.25 > M/M_{\rm Jup} > 13$ and with an orbital period < 10 days (Boss et al., 2003; Dawson and Johnson, 2018), which will also be the case in this work. The lower and upper mass limits corresponds to approximate boundaries of which the Jupiter becomes a super-Neptune or a brown dwarf, respectively. Gas giants with orbital periods $10 > P/\text{days} > 200$ are referred to as warm Jupiters, and are due to their larger orbits harder to detect than their hotter counterparts.

Hot and warm Jupiters have differences besides their periods like their occurrence rates (e.g. Santerne et al., 2016), eccentricity distribution (e.g. Petrovich and Tremaine, 2016) and companionships (Huang et al., 2016). Despite these differences, some part of the warm Jupiter population might serve as current or failed proto-hot Jupiters. If hot and warm Jupiters have a common origin, examining warm Jupiters might be the key to solve the origin mystery of hot Jupiters.

2.2 Classical formation theories

Before the discoveries of the first exoplanets, the theories of planet formation – built on observations of the Solar System – were thought to be well-established for several decades (Safronov, 1972): Stars are born in collapsing, rotating molecular clouds, forming together with circumstellar disks. These disks are flat due to angular momentum preservation and consist of gas and dust. Gas giants can be formed in these proto-planetary disks at and beyond the ”snow line”; a sweet-spot far away from the star, where the temperature is cool enough for ice and dust to be highly abundant. This is thought to happen either by the collapse of fragmented parts of the disk (disk instability) or by the capturing of gas by a proto-planetary core (core accretion). However, the former mechanism seems unlikely in the context of hot Jupiter formation, due to it's imposed temperature and density constraints on the gas (see e.g. the review papers Chabrier et al.

(2014) and Dawson and Johnson (2018)).

In the core accretion scenario, the planetary core is created first, followed by the accretion of gas. In short, the core is produced first by dust grains colliding and growing larger and larger, forming pebbles, rocks and planetesimals. When these reach sizes of 1 km s^{-1} (de Pater and Lissauer, 2015), their growth to several Earth-mass sized proto-planetary cores will continue by a combination of collisions and gravitational focusing. If gas has not yet been depleted at the core's location, it can then attract a gaseous envelope from the disk by first growing hydrostatic, and then through runaway gas accretion (Pollack et al., 1996) before the gas has evaporated. This is illustrated in Fig. 2.1.

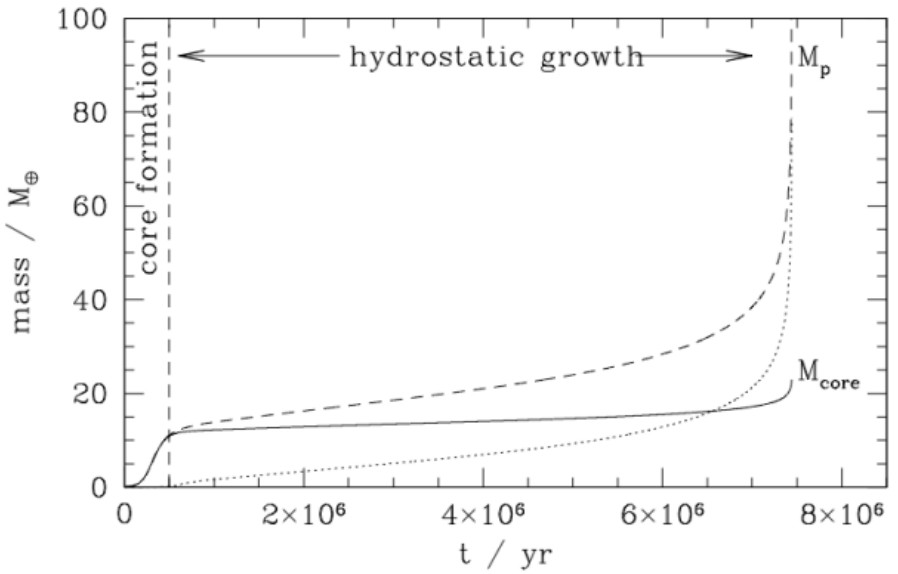

Figure 2.1: The growth in time of a giant planet through core-accretion. When the core has been formed, the initial gas accretion happens first through hydrostatic growth and then through runaway gas accretion. This figure is an adaption of figures in Pollack et al. (1996), made and modified by Phil Armitage (`www.solarsystemorigins.wordpress.com/2013/11/10/lecture-12-giant-planet-formation/`).

If planets remained static after their formation, the above picture would not be sufficient to explain the presence of hot Jupiters. While the formation of the proto-planets might happen at a location close to the star (e.g. the rocky planets in our Solar System), their growth is in most cases simply too slow to reach the planetary core stage before the evaporation of most of the gas from the inner part of the protoplanetary disk due to stellar radiation (see however Batygin et al. (2016) for special cases allowing this). Because of this rapid depletion, it therefore seems impossible that hot Jupiters formed *in situ*.

2.3 Migration mechanisms

Hot Jupiters either originate from *in situ* formation or migration (see Fig. 2.2). Because of the in-situ complications just mentioned, it is presently believed that most hot Jupiters form very far from their star, and then migrate inwards (Dawson and Johnson, 2018). However, the mechanism of this orbital evolution is greatly debated. The two main theories are disk migration (Goldreich and Tremaine, 1980; Lin and Papaloizou, 1986) and high-eccentricity migration (Rasio and Ford, 1996). In both cases, the end-product is a hot Jupiter, but distinguishing between which of these two are behind their creation is not straight-forward. In the following, the general concept of the two mechanisms are discussed, as well as possibilities to determine the most probable from observations.

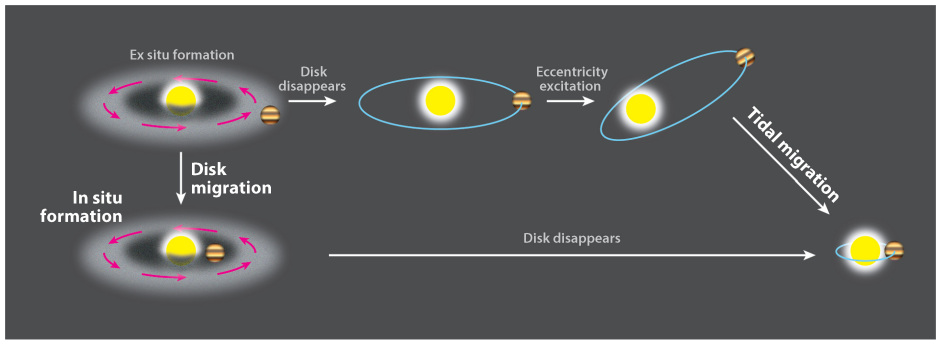

Figure 2.2: Sketch from Dawson and Johnson (2018) illustrating the three hot Jupiter origin scenarios; 1) *in situ* formation, 2) disk migration and 3) high-eccentricity migration.

2.3.1 Disk migration

Disk migration is the in- or outwards movement of the planet through the protoplanetary disk due to angular momentum exchanges between the two. This mechanism is typically divided into three categories; Type-I, Type-II and Type-III. Here a simplified explanation of the three is given, but see e.g. Nelson (2018) for a more comprehensive review. In the Type-I scenario (Goldreich and Tremaine, 1980) resonance torques will excite spiral density waves in the gas of the disk, which in return will exert unequal torques on the planet, making it move in the radial direction towards or away from the star. For the Type-III case (Masset and Papaloizou, 2003) or runaway migration, asymmetrical co-orbital torques – exerted by gas close to the planet – can cause rapid migration and create a feedback-loop for planets in high-mass and high-density disks. Both Type-I and Type-III migration happen for planets with masses smaller than Saturn and smaller than Jupiter, respectively. Though these might affect the planet at the core-creation stage, they therefore cannot be responsible for the inwards migration of the finished Jupiter-sized planets (Heller, 2019).

In Type-II migration (Lin and Papaloizou, 1986) tidal torques from a massive planet makes radical changes to the disk by clearing an annular gap in its orbit. Locked in this gap, the planet will move inwards as the gas in the disk accretes onto the star. Historically, this mechanism had (in isolation) problems stopping the migration and avoiding hot Jupiters from being consumed by their star. However, several possible solutions have been proposed to slow down the planet, including planet-star tidal interactions and the stellar magnetic field curtailing the inner part of the proto-planetary disk (Lin et al., 1996), possibly in combination with the planet arriving in specific resonances with the disk (Rice et al., 2008). The rate might also be decoupled from the vicious accretion, by being slowed down (or sped up) through Type-I migration if material is able to cross the gap; an action caused by the movement of the planet that changes the equilibrium of the outside gas (Hasegawa and Ida, 2013; Duffell et al., 2014). The rate and strength of this depends on the disk environment, but seems unimportant for disks with low viscosity (Robert et al., 2018).

A few direct images of circumstellar disks have indicated the presence of gaps caused by Type-II disk migration (see e.g. the HL Tauri system: ALMA Partnership et al., 2015; Akiyama et al., 2016). In addition, indirect methods of testing the prevalence of this mechanism as a hot Jupiter origin process might be possible by studying the spin-orbit (mis-)alignment distribution of hot and warm Jupiters: if most close-in giants were thought to stem from disk migration, we would (naively) expect alignment between the stellar equator and planetary orbit. In Sec. 2.5 it will be discussed in detail why this is more complicated than it appears.

2.3.2 *High-eccentricity migration*

An alternative to disk migration is high-eccentricity migration. Here, the planet does not arrive at its present location until *after* the gas disk has either been accreted or dissipated. Instead, the migration happens when the eccentricity and semi-major axis of the planetary orbit gets perturbed by dynamical interactions. Following these perturbations, the eccentricity and spin-orbit angle of the system might have changed. If the orbit has become highly eccentric (> 0.9, Dawson and Johnson, 2018), it's periastron distance will also decrease drastically, achieving a semi-major axis comparable to that of hot Jupiters. Though the planet in this orbit only spends very little time closest to it's host star, it will here be affected by tidal forces exerted by the star. This causes the orbit to lose energy, leading to a slight decrease in speed, orbital shrinking and eventually orbital circulation. The end result is a hot Jupiter in an approximately circular orbit.

The initial perturbations of the planetary orbit can happen either via scattering mechanisms (Rasio and Ford, 1996) and/or secular interactions (Wu and Lithwick, 2011; Petrovich, 2015). In the case of scattering, the Jupiter and a close-by third body – such as an additional planet or star – might cross paths and interact with each other. These interactions rarely result in collisions, but instead gravitational scattering, leading to changes in the eccentricity and the semi-major

axis for the planet, and an ejection or new orbit for the perturber. Though it has long been questioned whether eccentricities of > 0.9 can be reached by this mechanism alone (see e.g. Ford et al., 2001; Petrovich et al., 2014), new simulation studies reproduce systems with eccentricities of $e > 0.99$, suggesting that there is no upper limit through this mechanism (Carrera et al., 2019). However, even if gravitational scattering was not sufficient in driving the eccentricity to large enough values, it can serve as a starting point to perturbations by secular interactions.

Secular interactions are changes which take place on large time scales, and can happen in systems containing two or more bodies. Here the planet(s) (or additional companion stars) begin with a significant eccentricity and/or inclination, and exchange angular momentum between each other. These exchanges are either periodic (Petrovich, 2015) – happening through e.g. the Kozai mechanism (Kozai, 1962) between the Jupiter and another planet(s) (Naoz et al., 2011) or star(s) (Wu and Murray, 2003) in the system – or chaotic (Wu and Lithwick, 2011), with the exchange happening between three or more planets or stars. In both cases, the deficit in angular momentum compared to circular and co-planar orbits, leads to loss of angular momentum in the Jupiter's orbit, which then becomes progressively more eccentric and/or inclined.

Because high-eccentricity migration originally not only changes the eccentricity, but also might change the spin-orbit angle, and since these changes are suppressed in the stellar disk (Kley and Nelson, 2012), we would intuitively believe that large misalignments indicate a dynamical origin as opposed to disk migration. This is examined in more detail in the following sections.

2.4 Migration and spin-orbit studies

Many different approaches have been applied to figure out whether disk or high-eccentricity is the most dominant migration mechanism. The most explored procedure has been to examine the obliquity or spin-orbit angle of hot Jupiter systems (Fabrycky and Winn, 2009). This is the angle between the planetary orbital plane and the stellar equator. It is worth to note, that due to the way the obliquity is usually observed (see Chapter 3), the obtained quantity is often the *projected* angle λ, instead of being the three-dimensional value ψ.

If the star and proto-planetary disk were aligned at formation, the disk migration mechanism should lead to aligned hot Jupiter systems, i.e. with spin-orbit alignments and obliquity angles of zero. In contrast, if the planetary orbit is perturbed in the high-eccentricity mechanism, the hot Jupiter system could achieve large obliquity value, and will thus be misaligned. The validity of these assumptions and statements are examined in detail in the next section.

The first spin-orbit measurement of an exoplanet was performed at the beginning of this millennium (Queloz et al., 2000), and with two decades of observations we

now know the obliquity of 154 planets[1], including prograde, polar and retrograde systems. A large amount of systems are misaligned which points to the migration origin being high-eccentricity. But what about the aligned systems? Several population studies have been performed on the combined sample of systems with measured spin-orbit angles, including Winn et al. (2010) and Albrecht et al. (2012). In these studies, it was shown that systems with hot host stars have high obliquities, while systems with cool hosts show low obliquities.

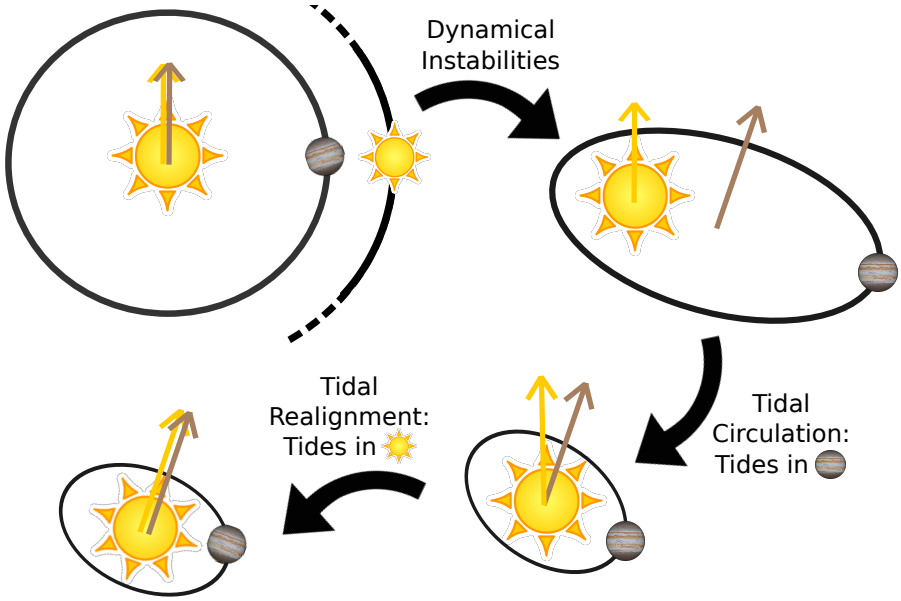

Figure 2.3: Sketch showing the phases of the high-eccentricity migration mechanism: A planet experiences dynamical instabilities by e.g. another star. This can make the planetary orbit highly eccentric, causing the star to tidally affect the planet. Following this, the orbit will become tidally circulated, resulting in a Hot Jupiter system. At timescales depending on e.g. the scaled orbital distance and the temperature of the star, the planet can in return tidally affect the star and realign the stellar equator with the orbital plane. In this sketch planet-star scattering is the reason behind the orbital change, but this might also happen due to e.g. secular interactions.

These observations of misaligned systems and their relationship with stellar temperature, were explained by the high-eccentricity migration happening in three steps (see Fig. 2.3): 1) the orbit of Jupiters near the snow line become perturbed, leading to highly eccentric, possibly misaligned orbits, 2) the planetary orbits shrink and become circularised through stellar tides dissipated in the planet leading to hot Jupiters and 3) planetary tides dissipated in the star realign the stellar equator with the planetary orbit, with an rate depending on the stellar

[1] www.astro.keele.ac.uk/jkt/tepcat/obliquity.html, accessed 2019-09-02.

effective temperature. This rate is thought to be connected to the Kraft break via the tides' ability to dissipate in convective vs. radiative stellar envelopes, providing an explanation for the temperature dependence (see e.g. Winn et al., 2010; Albrecht et al., 2012; Dawson, 2014). High-eccentricity migration followed by tidal realignment could therefore explain the existence of both aligned and misaligned systems in unison, lending further credibility to the origin of hot Jupiters being explained by this mechanism. But, even though these studies at first glance seemed to solve this long-standing puzzle, the interpretations faced several problems. First of all, it is theoretically hard to keep the hot Jupiter from decaying and subsequently perishing into it's host star, since the realignment happens at the expense of the planet's orbital angular momentum. Secondly, initial assumptions such as primordial spin-orbit alignment being the only outcome for the disk migration scenario deserves a closer inspection. The former problem was addressed in e.g. Lai (2012), suggesting the orbital decay happens on a much slower timescale than the realignment. The latter problem and possible solutions are addressed in the next section.

2.5 Tilted disks, warm Jupiters and multi-planet systems

At first glance, the obliquity observations seemed to resolve the hot Jupiter origin in favour of the high-eccentricity mechanism, since the initial conditions for secular interactions are thought to be unlikely to occur in the protoplanetary disk, as the orbits here are driven to low eccentricities and inclinations (see e.g. Kley and Nelson, 2012). However, arguing that disk migration cannot lead to misaligned systems hinges on one important assumption: The proto-planetary disk and stellar equator were primordially aligned. Several misaligned circumstellar disks have already been discovered (see e.g. Brinch et al., 2016), and theoretical studies suggests that stars and their disks are frequently misaligned at an early stage for reasons unrelated to planets: Proposed mechanisms include chaotic star formation (Bate et al., 2010) and torques due to neighbouring stars (Batygin, 2012), but these fail to explain the distinction between observed obliquities of cool and hot stars (as discussed in e.g. Dai and Winn (2017)). However, relatively recently a disk-torquing mechanism tilting the disk and simultaneously depending on stellar temperatures was presented (Spalding and Batygin, 2015). Here the inner edge of the proto-planetary disks of hot massive stars are tilted due to magnetic interactions, followed by disk migration of the resulting misaligned planets.

Several approaches have been suggested to try to distinguish between primordial misalignments due to tilted disks or misalignments happening due to high-eccentricity migration caused by dynamical interactions. This includes studying tilted disks, eccentric binaries, multiplanetary systems or warm Jupiters (see e.g. Albrecht et al., 2012). Though the realignment of hot Jupiter systems first appeared to support the high-eccentricity migration scenario, it also pollutes the original distribution of spin-orbit angles, making it complicated to study the origin further. It is therefore crucial to obtain a sample not sculpted by the re-

alignment. The realignment timescale is believed to scale very steeply with the scaled distance between the star and planet $a/R_\star$, in addition to the planet-star mass ratio $M_p/M_\star$. Using the same relations as in Albrecht et al. (2012), the orbital synchronisation timescale behave in the following way (Zahn, 1977):

$$t_C \propto \left(\frac{M_p}{M_\star}\right)^{-2} \left(\frac{a}{R_\star}\right)^{6} \tag{2.1}$$

$$t_R \propto \left(\frac{M_p}{M_\star}\right)^{-2} \left(1+\frac{M_p}{M_\star}\right)^{-5/6} \left(\frac{a}{R_\star}\right)^{17/2} \tag{2.2}$$

where the C and R subscripts refer to stars with convective and radiative envelopes, respectively. For cold stars with a convective envelope and hot Jupiters, this timescale is relatively short, and most observed systems of this type show alignment. By obtaining a large sample of 1) hot stars with radiative envelopes, or cold stars with 2) small-sized planets or 3) warm Jupiters, it is possible to study the original spin-orbit angle, avoiding the polluted, realigned population.

Warm Jupiters are located at the outer edge of the disk, not affected by the tilt presented in Spalding and Batygin (2015). If high-eccentricity migration is the dominant mechanism behind hot Jupiters – and warm Jupiters are precursors for these planets – warm Jupiter systems should show large obliquities. On the contrary, if hot Jupiters originate from a tilted inner disk followed by disk migration, warm Jupiters should never have become misaligned in the first place, and we expect these to have low obliquities. Thus, if warm Jupiter systems are in general found to be aligned, we would expect hot Jupiters to originate from disk migration, while if they are mainly found to be misaligned, we would expect them to originate from high-eccentricity migration.

Another possibility in differentiating between the two origin channels is to study misaligned multi-planet systems. If the hot Jupiter originate from a tilted disk and disk migration, we expect all planets to be similar misaligned. In contrast, in the high-eccentricity migration scenario, we could imagine that the inclination of all planets in the system are affected differently by e.g. scattering events. Significant mutual inclinations would therefore point towards high-eccentricity migration opposed to disk migration. Here it is important to keep in mind that secular interactions from a third body might also act to change the orbital architecture *after* the migration of the hot Jupiter, independent of whether the planet originates from disk or high-eccentricity migration. This is thought to be the case for the two known misaligned multi-planet systems of Kepler-56 (Huber et al., 2013; Gratia and Fabrycky, 2017) and HD 3167c (Dalal et al., 2019).

Due to observational biases, the sample sizes for both warm Jupiters and multi-planet systems have so far been too small to draw any definite conclusions on the origin of hot Jupiters: We only know the spin-orbit angle of a few more than a dozen warm Jupiters, and the numbers are even worse for multi-planet systems, where only a handful have had their spin-orbit measured or inferred (see Fig. 2.4). Two of those show misalignment, but both can be explained by subsequent

secular interactions after their migration. During this PhD study, this has been attempted to be mitigated by targeting these type of systems for observational follow-up and analysis.

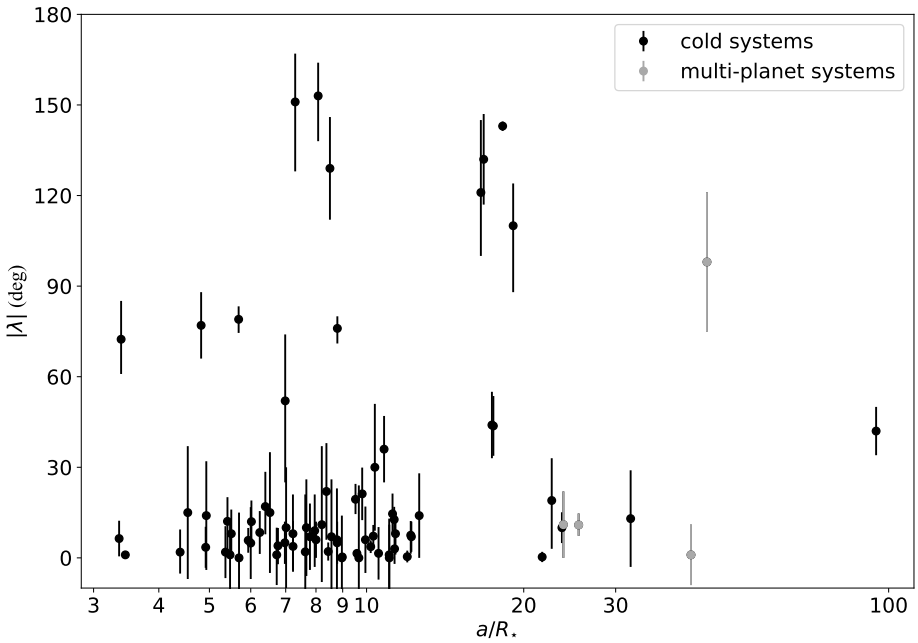

Figure 2.4: The projected absolute spin-orbit angle as a function of the scaled orbital separation for systems containing cold host stars ($T_{\rm eff} < 6250$ K). Compact multi-planet systems are marked with grey. We only include systems which have constrained λ to within 30 deg, and exclude systems with their spin-orbit inferred from estimation of the stellar inclination $i_\star$. The data is obtained from `www.astro.keele.ac.uk/jkt/tepcat/obliquity.html`

2.6 Several formation pathways?

It is important to keep in mind, that an alternative explanation for either outcome of the above observations could be that warm and/or hot Jupiters have more than one formation pathway. A recent population study proposed that 15 % of hot Jupiters originate from disk migration, while 85 % originate from high-eccentricity migration (Nelson et al., 2017). Examining hot Jupiters orbiting hot stars – which are believed to have very high tidal realignment timescales (See Eq. 2.2) – might be a way to study whether hot Jupiters form via two formation pathways, while avoiding getting the sample polluted by realigned systems. This was done in Winn et al. (2010), which found that these systems all have high obliquities, indicating formation by high-eccentricity migration only. However, revisiting the study using the now much expanded sample of hot Jupiter obliquities, the picture seems ambiguous: several of these systems show alignment, together with the original sample showing misalignment, as can be seen

in Fig. 2.5. The overabundance of aligned systems cannot be explained through current theories on high-eccentricity migration and tidal realignment. One explanation for the two populations is that we simply do not understand tides as well as we thought we did. Another possibility is that the two populations each have their own origin; the aligned systems formed through disk migration, while the misaligned systems formed via high-eccentricity migration. For warm Jupiters, two distinct populations has been supported by observations of eccentricities (Dong et al., 2014) and companionships (Huang et al., 2016). In the former, a picture similar to above is proposed: warm Jupiters with high eccentricities originate from high-eccentricity migration, while warm Jupiters with low eccentricities form in-situ or originate from disk migration. The loneliness of hot Jupiters have been explained theoretically by the giant planet migrating inwards through high-eccentricity migration, ejecting companions on the way (Mustill et al., 2015). However, if warm Jupiters are the progenitors for hot Jupiters, this is in conflict with the many companions observed to warm Jupiters, suggesting two different formation scenarios for these. Either way, the formation paths of both hot and warm Jupiters will be illuminated greatly by having a large sample of both studied in detail and with great accuracy.

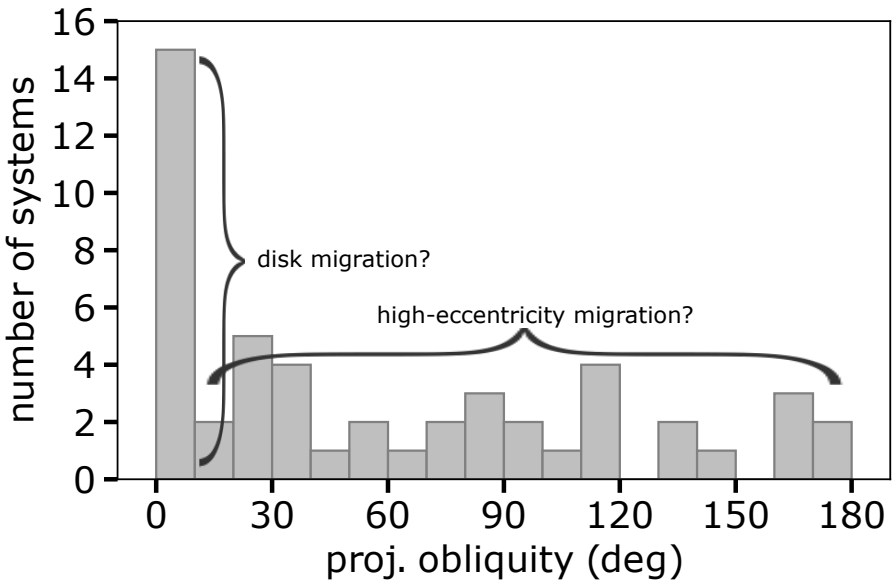

Figure 2.5: A histogram of the hot Jupiters orbiting hot stars with measured obliquities. In contrast with earlier studies (Winn et al., 2010), there seems to be a significant number of aligned systems, as well as misaligned. This might indicate, that hot Jupiters form via two formation pathways: the aligned by disk migration and the misaligned by high-eccentricity migration. By only using systems with hot stars, the sample is not biased by possible realignment of the stellar spin-axis. The data are extracted from the obliquity database of John Southworth (`www.astro.keele.ac.uk/jkt/tepcat/obliquity.html`).

3

Obtaining spin-orbit angles

3.1 Spin-orbit measurements

As discussed in the previous chapter, the spin-orbit angle – or obliquity – of a planetary system is the angle between the stellar equator and the planetary orbit. This is sketched in Fig. 3.1. Due to the spin-orbit angle being able to probe the origin of hot and warm Jupiters, several methods have been utilised to obtain it. These include studying the velocity anomaly due to the Rossiter-McLaughlin effect (Rossiter, 1924; McLaughlin, 1924), the related Doppler Tomography technique (Albrecht et al., 2007; Collier Cameron et al., 2010), examining starspots (Sanchis-Ojeda et al., 2011; Mazeh et al., 2015) and gravity darkening (Barnes, 2009). In this chapter, the theory on absorption line shapes necessary to describe the Rossiter-McLaughlin (RM) effect will be introduced (Sec. 3.2), and it will be presented how to acquire obliquities from the resulting velocity anomalies (Sec. 3.3) and the Doppler Tomography technique, even on low S/N data (Sec. 3.4).

Measuring the Rossiter-McLaughlin effect is the most commonly used method to obtain spin-orbit angles. Before the discovery of the first exoplanets, it was previously measured in binary systems. The technique traditionally takes advantage of the radial velocity of the star changing during a planetary transit. Another related approach is to directly study the changes by performing Doppler Tomography. This method utilises the underlying physics behind the Rossiter-McLaughlin effect, by examining the distortion of the stellar absorption lines due to the transiting planet. Doppler Tomography was first used on an exoplanetary system in Collier Cameron et al. (2010), and has since gained popularity, partly due to its success on systems with rapidly spinning stars (see e.g. Talens et al., 2017).

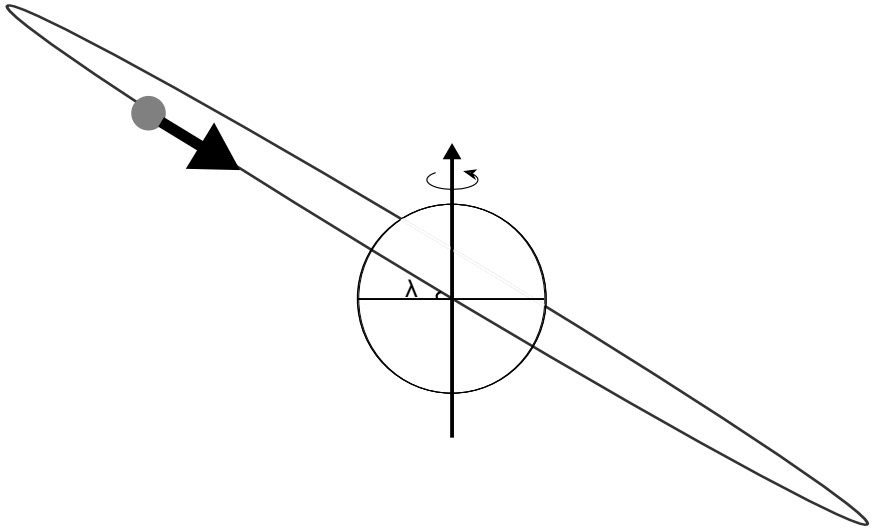

Figure 3.1: A sketch showing the definition of the spin-orbit angle; the angle between the stellar spin and the planetary orbit.

3.2 Line shape and broadening

To describe the theory behind the Rossiter-McLaughlin effect, it is necessary to construct an accurate model describing stellar lines both in- and outside of transit. In the following, the different physics behind the model will be explained, with a large part based on the description in Gray (2005).

3.2.1 Line formation

Stellar absorption lines are generated in the stellar photosphere, and stem from bound-bound molecular and atomic transitions. The line will not be sharp, but will instead extend over a range of wavelengths, due to different broadening mechanisms. Local broadening mechanisms include natural broadening, pressure broadening and thermal Doppler broadening. These can individually be described by Lorentzian, Gaussian and Voigt functions. However, if the lines are weak the convolution of all of these will be dominated by the thermal broadening, resulting in a line profile that can be assumed to be Gaussian (p. 430 Gray, 2005). In this thesis, the intrinsic stellar line profile is therefore assumed to be Gaussian in shape, as is also done in e.g. Collier Cameron et al. (2010). Besides the intrinsic line broadening, the shape of the absorption lines will also be affected by other phenomena. The model presented here includes limb darkening and stellar rotation as well as micro- and macroturbulence.

3.2.2 Limb darkening

Limb darkening is an effect which makes the limbs of the stellar disk appear dimmer than the center. This is because an optical depth of unity will probe further into the star at the center than at the limb. Throughout this thesis, a quadratic limb-darkening law will be used, with coefficients calculated from e.g. Claret (2000)[1]. The normalised intensity at a given point is then given as:

$$\frac{I}{I_0} = 1 - c_1(1-\mu) - c_2(1-\mu)^2 \tag{3.1}$$

where $\mu = \cos\theta$ with θ being the angle between the observer and the given point on the surface, when measuring from the stellar center. A limb-darkened modelled stellar disk can be seen on figure 3.2.

3.2.3 Stellar rotation

Because of the stellar rotation, the line will experience Doppler broadening: The preceding limb will broaden the line towards longer wavelengths, while the approaching limb will broaden the line towards shorter wavelengths. Since the equivalent width of the line must be conserved, the rotational broadening will lead to the line becoming more shallow than the intrinsic line profile (Gray, 2005, pp. 466-469).

The largest Doppler shift will occur at the limb. However, since the stellar poles might be inclined compared to the observer's line-of-sight with an angle $i_\star$, the limb-velocity is not necessarily the 3D rotational velocity, v. Instead, what is measured is the projected velocity, $v \sin i_\star$. Here it is assumed, that the star rotates as a rigid body. For Doppler Tomography, the stellar line distortion during transit can typically only be resolved for $v \sin i_\star > 5 - 10$ km/sec.

3.2.4 Microturbulence

Microturbulence describes the non-intrinsic small-scale motions of elements in the stellar photosphere. This motion is typically around 1-2 km/sec (Hirano et al., 2011), and leads to a Doppler-broadening of the spectral lines. Because this effect is small compared to e.g. stellar rotation and macroturbulence, it is impossible to disentangle it from the other broadening mechanisms and measure the shape of it. Therefore, it has become the standard procedure to assume it takes the form of an isotropic Gaussian (Gray, 2005, p. 430). To include it in our computation, the microturbulence profile should be convoluted with the intrinsic stellar line, which was also assumed Gaussian. Since the convolution of two Gaussians is a new Gaussian, the intrinsic line can be defined to automatically include microturbulence (Hirano et al., 2011):

$$G(v) = \frac{1}{\beta\sqrt{\pi}} \exp(-v^2/\beta^2) \tag{3.2}$$

[1] Using the software created by John Southworth, http://www.astro.keele.ac.uk/jkt/codes/jktld.html

where β is the dispersion parameter, including both the intrinsic thermal line broadening and microturbulence, and is given as

$$\beta = \sqrt{\left(\frac{2k_B T_{\text{eff}}}{\mu} + \xi^2\right)} \tag{3.3}$$

with k_B being the Boltzmann constant, μ the molecular mass, T_{eff} the effective stellar temperature and ξ the microturbulence parameter. If it is desired to include the broadening due to the instrumental profile in the computations, a possibility is to add the squared PSF width in the expression for β (as is done in Hirano et al., 2011).

An estimate of ξ (which can be used as a prior) can be calculated following the model from Coelho et al. (2005), which depends on the stellar surface gravity $\log g$.

3.2.5 Macroturbulence

Macroturbulence describes the large-scale motion of mass in the stellar photosphere. Large structures are usually defined in such a way, that photons remain in them from creation until they escape the stellar surface (p. 431 Gray, 2005). One example of macroturbulence is the convective motion in the outer envelope of cool stars. While the Sun's macro-cells can be resolved, this is (usually) not the case for other stars. Therefore, the individual spectrum for each macro-cell is observed simultaneous, and macroturbulence will lead to a broadening of the stellar line.

However, looking at the convective cells of the Sun, it is easily seen that this motion is not isotropic: near the center the motion will be radially, while it will be tangentially near the limb. This means, that a model describing macroturbulence will be more complicated than a simple Gaussian. In this thesis, the radial-tangential anisotropic model described in Gray (2005) pp. 433-434 is used, in which macroturbulence is described as a linear combination between the tangential and radial motion respectively:

$$M(v) = \frac{1}{2\sqrt{\pi}\zeta}\left(\frac{1}{\cos\theta}e^{-(\frac{v}{\zeta\cos\theta})^2} + \frac{1}{\sin\theta}e^{-(\frac{v}{\zeta\sin\theta})^2}\right) \tag{3.4}$$

where ζ is the macroturbulence parameter and it is assumed, that half of the stellar surface have radial motion, the other half tangential. As described previously, θ is also used when determining the limb darkening, and can be calculated using (Hirano et al., 2011):

$$\sin\theta = \frac{\sqrt{x^2+y^2}}{R_\star}, \quad \cos\theta = \sqrt{1 - \frac{x^2+y^2}{R_\star}} \tag{3.5}$$

where x and y are the stellar disk coordinates, and $R_\star$ is the stellar radius. The macroturbulence parameter ζ can be calculated using the relation between ζ and

T_{eff} given in Gray (1984) and Valenti and Fischer (2005). It is important to note, that the broadening due to macroturbulence is comparable to the broadening caused by stellar rotation in cool stars.

3.2.6 Computing a numerical stellar line

Constructing a stellar disk is the first step in numerically creating a modelled stellar absorption line. Each surface element (i.e. pixel) on this disk is assigned a certain value, which is then scaled in accordance with the quadratic limb-darkening. The velocity of the stellar disk can be seen as a number of vertical bands parallel to the projected rotation axis, with the Doppler shift increasing from the center towards the edge, until it reaches a value of $v \sin i_\star$ (as is nicely illustrated in Gray (2005), fig. 18.3 and fig. 18.5).

As discussed in Gray (2005, p. 436), it is not permitted to simply convolve the macroturbulence and rotation profiles, because of their non-isotropic nature. Instead the approach should in principle be to do full disk integration, by combining the Dopplershift caused by macroturbulence and rotation on the intensity value at each pixel on the modelled stellar disk and sum them up. However, looking at the radial-tangential model, it is apparent that the description is circular symmetric. Therefore, another procedure with less computations is to split the model stellar disk into rings, and calculate the rotational profile and macroturbulence for each ring. The value of μ will (approximately) be the same at every pixel in a given ring, and the macroturbulence will therefore also be the same at any pixel in a given ring. To get the rotational profile, each limb-darkened pixel of a ring can then be added in bands of the same velocity value. Creating the rotational profile in this way, ensures that limb darkening is automatically accounted for. For each ring, the line is then created by convolving the intrinsic line profile (including microturbulence) $S(v)$ with the rotational profile $R(v)$, and then convolving the resulting profile with the macroturbulence profile of the ring $M(v)$. The total stellar line profile can then be achieved by summing the profile for each ring:

$$F(v) = \sum^{N} F_{\text{ring}}(v) = \sum^{N} [S(v) * R(v) * M(v)] \tag{3.6}$$

where N is the number of rings, which depends on the resolution chosen for the model.

3.2.7 Planetary transit

So far, the focus has been on developing a model for the stellar absorption line applicable when outside of transit. However, implementing the planet is straightforward. To improve computational time the out-of-transit intrinsic line profile $S(v)$ is reused for each in-transit epoch: the planet is included by 1) calculating the planetary coordinates at any given epoch, 2) setting each surface element (pixel) on the modelled stellar disk which is covered by the planet to zero (i.e.

change the rotation profile $R(v)$ and macroturbulence profile $M(v)$), and 3) do the disk integration in rings as above.

The coordinates of a planet in a system with an obliquity of zero is in units of the stellar radius $R_\star$ given as (Winn, 2010, eq. 2 and 3)

$$\begin{aligned} x &= -\frac{r}{R_\star}\cos(\omega+\nu) \\ y &= -\frac{r}{R_\star}\sin(\omega+\nu)\cos i_{\mathrm{orb}} \end{aligned} \tag{3.7}$$

where $r/R_\star$ is the distance between the star and planet in units of the stellar radius, ω is the argument of periastron, ν is the true anomaly and i_{orb} is the system's orbital inclination. Here the coordinates is centred on the stellar disk, with x and y on the sky-plane. Using already established system parameters for the scaled distance $a/R_\star$, the eccentricity e and the impact parameter b, the value of $r/R_\star$ and i_{orb} can be calculated from Winn (2010), eq. 1 and 7 respectively. The value of ν at each epoch is calculated by numerically solving Kepler's equation using the procedure described in Murray and Correia (2010).

To include the projected obliquity in the model, the above coordinate system can be rotated by the obliquity angle λ, by applying the standard 2D rotation matrix. The resulting coordinates are:

$$\begin{aligned} x_{\mathrm{rot}} &= x\cos\lambda - y\sin\lambda \\ y_{\mathrm{rot}} &= x\sin\lambda + y\cos\lambda \end{aligned} \tag{3.8}$$

With these tools it is possible to track the planet's movement across the stellar disk, and amend the modelled stellar line during transit for each epoch. While this section has described the physical changes of the absorption line during a spectroscopic transit, the next section will be focused on the more intuitive way of thinking of the Rossiter-McLaughlin effect, namely as a velocity anomaly.

3.3 The Rossiter-McLaughlin effect as a velocity deviation

The Rossiter-McLaughlin effect is the change of the stellar spectroscopic signal during transit of its planet companion (or a binary stellar companion). The effect is caused by the planet blocking some of the stellar light: The blocked light will – due to the stellar rotation – be either blue- or redshifted (or both). When the planet moves across the stellar disk, different parts will be covered, which will appear as a velocity anomaly in the radial velocity or alternative as a change of shape in the stellar absorption lines.

The effect was first seen in binary stars, but have since been observed widely in exoplanetary systems. Here it was used for the first time on HD 209458 by measuring the velocity anomaly happening during transit (Queloz et al., 2000). From the shape and amplitude of this change in radial velocity it is possible to

extract different system parameters, most importantly the sky-projected stellar rotational velocity $v \sin i_\star$ and the projected obliquity angle λ.

For slow rotating stars, the amplitude of the velocity anomaly is approximately (see e.g. Triaud, 2018):

$$A \approx \frac{2}{3} \cdot v \sin i_\star \cdot \delta \cdot \sqrt{1 - b^2} \tag{3.9}$$

where δ is the transit depth and $2/3$ is an estimation of the amplitude reduction due to limb darkening. The impact parameter b is a measure of the distance between the center of the stellar disk and the planet during transit, ranging from zero (planet will cross disk center) to unity (planet will move at the very edge of the disk).

From eq. 3.9 it becomes clear that the amplitude is highest for planets with the largest transit depths, explaining why most Rossiter-McLaughlin measurements have been performed on Jupiter-sized planets. With the construction of larger ground-based telescopes and with the recent arrival of the *TESS* mission – which primarily finds planets orbiting M-dwarfs – the radius limit on spin-orbit measurements through the Rossiter-McLaughlin effect is expected to go down to nearly Earth-sized planets (see e.g. Johnson et al., 2019, for a white-paper on this subject). Preliminary results and implications of measurements of an M-dwarf planetary system, will be discussed further in Chapter 7 in the context of the seven-planet system of Trappist-1. From eq. 3.9 it also appears that stars with large $v \sin i_\star$ values should be favoured signal-wise. However, though the amplitude will be larger for rapid rotating stars, these have the drawback of fewer and broader metal lines, which translates to larger uncertainties when extracting the radial velocities from the spectra. For this type of star, the complications can be avoided by using the Doppler Tomography technique instead. In Chapter 4 the planetary system of MASCARA-3 will be presented, which lies in a sweet spot where both techniques can be applied.

3.3.1 Shape and symmetry considerations

Though the spin-orbit angle can range from -180 deg to +180 deg, $+\lambda$ is equivalent to $-\lambda$ with the stellar rotation axis flipped. For the rest of this section λ will refer to $|\lambda|$, ranging from 0 to 180 deg. While it is the amplitude of the velocity deviation that exposes the feasibility of measuring the spin-orbit angle, it is the shape and (a)symmetry which reveals the spin-direction. When the planet crosses the blueshifted part of the stellar disk, we will obtain an excess of redshifted light, equivalent to a positive radial velocity change. Vice versa, we will achieve a negative radial velocity change when it crosses the redshifted part. This means, that for prograde systems ($\lambda < 90$ deg) the signal will be positive-negative, and for retrograde systems ($\lambda > 90$ deg) it will be negative-positive. For completely polar orbits ($\lambda \sim 90$ deg) the signal will be *either* positive or negative (or disappear as the impact parameter approaches zero). An example of different shapes is illustrated in Fig. 3.2.

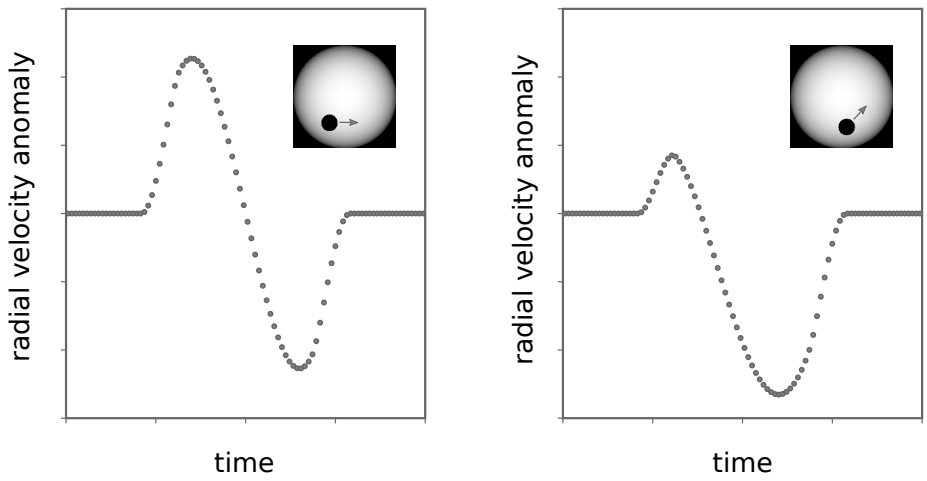

Figure 3.2: Schematic examples of the velocity anomaly in the stellar radial velocity during transit. Left: An aligned system (an obliquity of 0 deg). Right: A misaligned system (an obliquity of 40 deg). On the stellar disks, the projected stellar rotation axis is chosen as a vertical line down the middle of the star. In both cases the impact parameter b is significantly above 0.

It is important to once again emphasise, that because we often only know the stellar movement in the observer's line-of-sight, it is usually only possible to get the sky-projected obliquity λ from the Rossiter-McLaughlin effect and not the 3D spin-orbit angle ψ, unless the stellar inclination can be extracted from the stellar rotation period (as will be done for K2-290 in Chapter 6). However, it is worth to keep in mind that usually for systems with $\lambda < 90$ deg the 3D angle will be $\psi > \lambda$, and for $\lambda > 90$ deg the 3D angle will be $\psi < \lambda$ (Fabrycky and Winn, 2009).

Historically, measuring the velocity anomaly produced by the Rossiter-McLaughlin effect has been the favoured way to extract the obliquity of exoplanetary systems. However, when doing these measurements on systems with an impact parameter b close to or equal zero, different complication may arise.

One problem is the possible degeneracy between the projected rotation $v \sin i_\star$ and the spin-orbit angle λ when the impact parameter b vanishes: For a planet which travels across the central part of the disk, the signal will always be symmetric, no matter the value of λ. In other words, a small $v \sin i_\star$ and λ will produce a velocity anomaly amplitude equivalent to a large value for both. In Albrecht et al. (2011) these considerations were parameterised as the mean amplitude and the asymmetry between the maxima velocity anomalies on either side

of the signal:

$$\frac{1}{2} v \sin i_\star (x_2 + x_1) = \sqrt{1 - b^2}\, v \sin i_\star \cos \lambda \tag{3.10}$$

$$\frac{1}{2} v \sin i_\star (x_2 - x_1) = b v \sin i_\star \sin \lambda \tag{3.11}$$

where x_1 and x_2 are the distance from the projected stellar rotation axis at ingress and egress, as depicted in Fig. 3.3. From the amplitude it will in that case therefore not be possible to determine λ without prior information on $v \sin i_\star$, but only whether the system is pro- or retrograde from the sequence of positive or negative signal. As mentioned earlier and as also discussed in Albrecht et al. (2011), another complication from modelling the velocity anomaly appears if $b = 0$ with $\lambda = 90°$. In this case, equal parts of the Doppler-shifted stellar surface will be covered, making the amplitude of the signal approach zero.

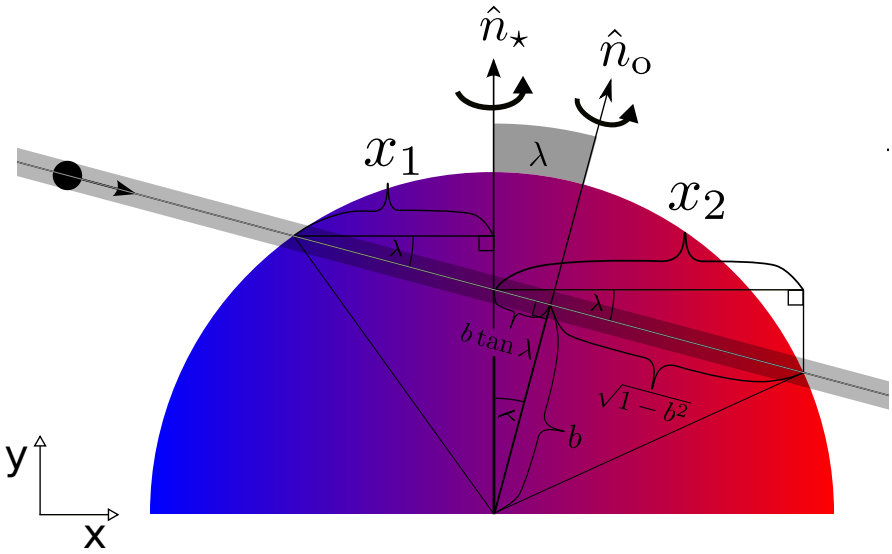

Figure 3.3: Sketch from Albrecht et al. (2011) illustrating the geometry of the transit used to describe the mean amplitude and asymmetry. $\hat{n}_\star$ and $\hat{n}_\mathrm{O}$ denote the unit vectors of the projected stellar spin and planetary orbit, respectively.

In addition, large values of b might also cause problems with low S/N data, which in Albrecht et al. (2011) was shown to have resulted in an erroneous spin-orbit angle of WASP-2 (Triaud et al., 2010). Here the fit will be biased towards the antisymmetric 0 and ±180 deg in favour of the symmetric 90 deg signal. As a sidenote, a similar effect can happen when fitting for the eccentricity e and the argument of periastron ω, for ω close to ±90 deg (Albrecht et al., 2012). This will be discussed further in Chapter 5. All of these effects are important to keep in mind when modelling the Rossiter-McLaughlin effect. Alternatively, these complications can be avoided or mitigated using the Doppler Tomography technique when dealing with rapid rotating stars.

3.3.2 Modelling the velocity anomaly

In order to obtain information to a greater extent than whether a planetary system is pro-/retrograde, it is necessary to compare spectroscopic transit radial velocity data to a model of the velocity anomaly. Some selected aspects of such a model is presented in this subsection. This is part of preliminary work which I have done at the supervision of Prof. Teruyuki Hirano, carried out at Tokyo Institute of Technology. The goal is to publish a velocity anomaly model, as to our knowledge, no software on this is currently publicly available.

Much of the theory behind constructing the semi-analytical model for the velocity anomaly has already been established in Sec. 3.2, where the model was made completely numerical. This includes the description of the stellar disk coordinates, the stellar rotation, the limb darkening and the micro- and macro-turbulence, with the definition of the parameters remaining the same here.

The development of the model is based on the work of primarily Hirano et al. (2011) – from where a thorough description and semi-analytical equations on the velocity anomaly is derived – but also on Hirano et al. (2010) and Hirano (2014). These were constructed as a response to inaccuracies discovered when comparing data to a simple velocity anomaly model derived in Ohta et al. (2005). Going through the calculations of the improved model is outside the scope of this dissertation, so here we focus on the more intuitive simple description, and discuss how and why it differs from the advanced version.

In the simple picture, the Rossiter-McLaughlin velocity anomaly Δv is given as (Ohta et al., 2005; Hirano et al., 2011):

$$\Delta v \approx -\frac{f}{1-f} v_p \tag{3.12}$$

where f is the instantaneous flux-loss caused by the planet transiting and v_p is the sub-planet velocity. The instantaneous flux-loss can be calculated through the following expression, integrated over the occulted portion of the stellar disk:

$$f = \iint_{\text{occ}} \frac{1 - c_1(1-\cos\theta) - c_2(1-\cos\theta)^2}{\pi(1 - c_1/3 - c_2/6)} \frac{dxdy}{R_\star^2} \tag{3.13}$$

Assuming v_p – which is the rotational velocity of the star below the area blocked by the planet – is constant under the occulted region. The sub-planet velocity can be describes as $v_p = xv \sin i_\star / R_\star$. Here x and y are the intensity-weighted stellar disk coordinates. These weighted coordinates only differ from the non-weighted coordinates X and Y by a scaling factor A during ingress and egress. The coordinates can be calculated from solving Kepler's equation to obtain the true anomaly, and depends on orbital parameters such as the impact parameter b (see Sec. 3.2.7). Using trigonometry the scaling A from X and Y to the intensity-weighted coordinates x and y can be shown to be given as:

$$A = \frac{R_p^2(\beta - \frac{1}{2}\sin(2\beta))}{R_\star^2(\alpha - \frac{1}{2}\sin(2\alpha)) + R_p^2(\beta - \frac{1}{2}\sin(2\beta)} \tag{3.14}$$

with the angles α and β depending on X, Y, R_p and $R_\star$, and given in Fig. 3.4. Besides describing the simple velocity anomaly model, eq. 3.13 and 3.14 are also used when constructing the concentrated Doppler shadow in Sec. 3.4.

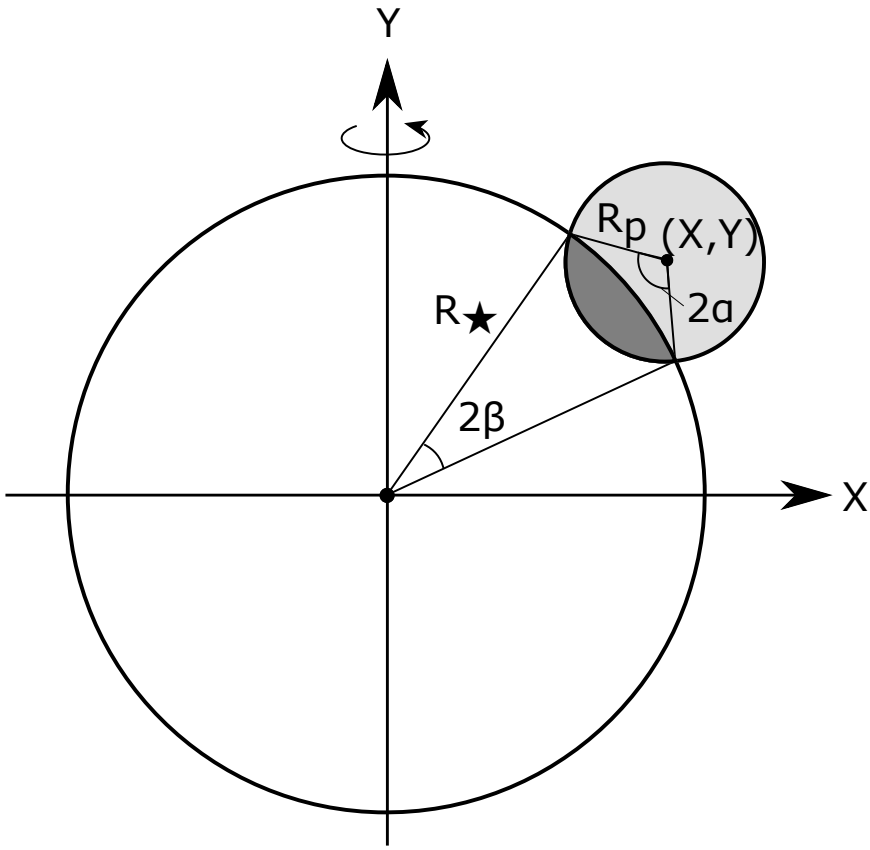

Figure 3.4: An adaption of Fig. 6 from Hirano et al. (2010) showing the coordinate system used to calculate the intensity-weighted coordinates (x,y) from the non-weighted coordinates (X,Y) at ingress and egress.

As also discussed in Hirano et al. (2010, 2011) the simple picture given by eq. 3.12 is independent of the stellar rotation velocity. This causes the model to underestimate the velocity anomaly, especially for rapid rotating stars. Another problem is different procedures for extracting the RVs, which might cause the shape and amplitude of the model to not match the data. To avoid these problems for the software which will be made publicly available, we are using the advanced model of Hirano et al. (2011) for iodine cell spectrographs which fit a template to observed spectra to obtain the RVs (e.g. SUBARU) and the model described in Hirano (2014) for spectrographs deploying the cross-correlation technique when extracting RVs (e.g. HARPS).

3.4 Doppler Tomography

The Doppler Tomography technique takes advantage of the Rossiter-McLaughlin effect, but instead of analysing the velocity anomaly, the examination is done on the underlying origin, namely the change in line shape because of the transiting planet. This method was developed for extracting the obliquity of eclipsing binaries (Albrecht et al., 2007), but was subsequently used to study exoplanetary systems (Collier Cameron et al., 2010).

The largest advantage of the Doppler Tomography method, is that it can remove the degeneracy between $v \sin i_\star$ and λ when $b = 0$ (see e.g. HD 189733 in Collier Cameron et al., 2010). This is because $v \sin i_\star$ will be constrained by both the shape of the planetary Doppler Shadow as it moves across the stellar disk, but also by the shape of the stellar absorption line outside of transit. Furthermore, even when the velocity anomaly vanishes at $b = 0$ with $\lambda = 90°$, the Doppler Shadow still remains (see e.g. WASP-76 in Brown et al., 2017). In these cases, the Doppler Tomography method is therefore superior, when it is possible to resolve the change in the stellar absorption line caused by the transiting planet, i.e. when the star is spinning sufficiently fast on our line of sight. For systems with $v \sin_\star < 5$ km s^{-1}, it might be more beneficial to examine the Rossiter-McLaughlin effect from the velocity anomaly, due to the difficulty in resolving the shadow. It is worth noting, that this anomaly in principle can be extracted directly from Doppler Tomography.

3.4.1 The Doppler shadow

For a single line, the change in line shape is small, and hardly detectable to the naked eye (see e.g. Kepler-25, Albrecht et al., 2013). However, when combining multiple stellar lines (e.g. through a cross-correlation function CCF or broadening function BF) the distortion of the stellar line can be resolved for systems with rapid rotating host stars. During transit, the planet's presence will appear as a "bump" in the stellar absorption line, travelling through the line as the planet moves across the stellar disk. The Doppler shadow is the CCF or BF at each epoch subtracted from an out-of-transit absorption line, constructed by e.g. taking an average of all out-of-transit absorption lines.

The system parameters are extracted by creating a model Doppler Shadow. This is likewise constructed by subtracting the out-of-transit absorption line model from the model lines at each epoch. At ingress the planet will appear as a dark distortion, creating a linear trail as the planet cross the disk, which disappears when reaching egress. An example of a Doppler shadow together with it's (exaggerated) corresponding modelled absorption line deformation can be seen in Fig. 3.5.

For slow rotating stars or for data with very low S/N, it can be difficult to extract the shadow signal. One workaround adopted here, is the technique first described in Johnson et al. (2014) of concentrating the signal. In this method, a 3D grid of

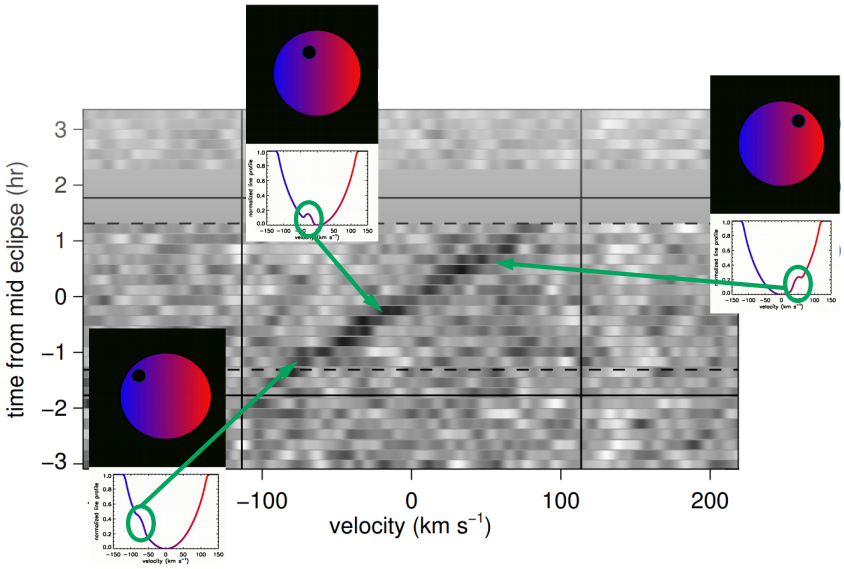

Figure 3.5: An example of how the Doppler shadow looks like, for an aligned planet trailing across the stellar disk. The data shown here are from the discovery paper of MASCARA-2 (Talens et al., 2018) measured using SONG. The inset stellar disks with their accompanying (exaggerated) distorted absorption lines are also from this specific system and is original generated by Marshall C. Johnson `http://www.astronomy.ohio-state.edu/~johnson.7240/`.

($v \sin i_\star$, λ, b) is constructed. For each of these $v \sin i_\star$, λ and b trial values, the absorption lines are shifted by the sup-planet velocity v_p, given in Sec. 3.3. The shifted shadow is then collapsed along the time-axis. This collapsed signal will be largest at a velocity of zero for values of $v \sin i_\star$, λ and b closest to the system parameters. This is illustrated in Fig. 3.6. A single representative value for the collapsed signal is found by fitting a Gaussian to it. Doing this, we can assign a value to the entire 3D grid, and then get posteriors for $v \sin i_\star$, λ and b by fitting a 3D Gaussian (an ellipsoid) to the grid. An example of this technique in action is given in the following chapter for the MASCARA-3 system.

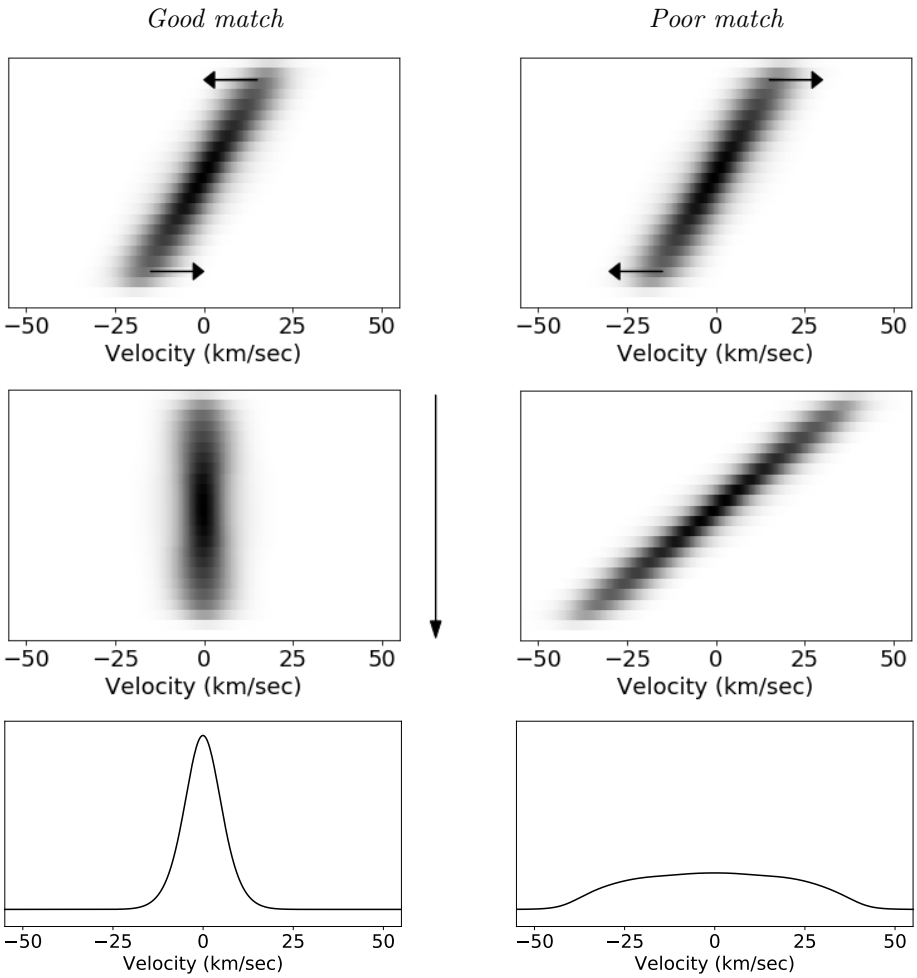

Figure 3.6: A sketch showing the principles of the shadow concentration technique first used in Johnson et al. (2014), which can be used in cases of slowly rotating stars or a low S/N. The left panel is for a good match between system parameters and the values of $v \sin i_\star$, λ and b at this specific place in the grid, while the right panel represents a location in the grid with a poor match. The top panel shows the shadow as-is, before the technique has been applied. The middle panel shows the concentrated or weakened shadow after it has been shifted by the sub-planet velocity at each time stamp. The lower panel shows the vertical collapse of the shifted shadow (collapsed along the time axis). Here, the best matching values of $v \sin i_\star$, λ and b will produce the highest signal value at a velocity of zero.

4

MASCARA-3b: a hot Jupiter transiting a bright F7 star in an aligned orbit

In the previous chapter the Rossiter-McLaughlin effect was introduced together with the two connected observational techniques; measuring the velocity anomaly and doing Doppler Tomography. It was mentioned how the former is best utilised when obtaining the obliquity for slow rotating stars, while the latter works best for rapid rotating stars. This is because slow rotating stars will have a shadow signal too small for the resolving power of most spectrographs, while rapid rotating stars in return will have very few and broad lines, making it hard to extract precise RVs. This chapter presents a rare example of a planetary system which is bright and lies in a $v \sin i_\star$ sweet spot: With a projected rotation of ~ 20 km s^{-1} me and my collaborators were able to measure both the velocity anomaly and Doppler shadow of the bright MASCARA-3 system. This meant that besides reporting the discovery and characterisation of MASCARA-3b and it's host star, we were also able to establish the alignment of the system. This chapter is with only minor alterations based on a manuscript (Hjorth et al., 2019)[1] accepted for publication in Astronomy & Astrophysics. I have written the manuscript and in addition done the majority of the analysis, with the exception of extracting the original light curve described in section 4.3.1 (done by co-author Talens), extracting the RVs, BFs and CCFs from the spectra (done by co-author Grundahl and Albrecht) as well as performing and writing about the stellar analysis presented in section 4.4 (done by co-author Justesen).

4.1 Summary

We report the discovery of MASCARA-3b, a hot Jupiter orbiting its late, bright ($V = 8.33$) F-type host every 5.55149 ± 0.00001 days in an almost circular orbit ($e = 0.050^{+0.020}_{-0.017}$). It is the fourth exoplanet discovered with the Multi-site

[1] Authors: Hjorth, M., Albrecht, S., Talens, G. J. J., Justesen, A. B., Otten, G. P. P. L., Antoci, V., Dorval, P., Foxell, E., Fredslund Andersen, M., Grundahl, F., Murgas, F., Palle, E., Stuik, R., Snellen, I. A. G. and Van Eylen, V.

All-Sky CAmeRA (MASCARA), and the first of these which orbits a late-type star. Follow-up spectroscopic measurements were obtained in and out of transit with the Hertzsprung SONG telescope. Combining the MASCARA photometry and SONG radial velocities reveals a radius and mass of 1.36 ± 0.05 $R_{\rm Jup}$ and 4.2 ± 0.2 $M_{\rm Jup}$. In addition, SONG spectroscopic transit observations were obtained on two separate nights. From analyzing the mean out-of-transit broadening function we obtain $v \sin i_\star = 20.4 \pm 0.4$ km s^{-1}. In addition, investigating the Rossiter-McLaughlin effect, as observed in the distortion of the stellar lines directly and through the velocity anomalies, we find the projected obliquity to be $\lambda = 1.2^{+8.2}_{-7.4}$ deg, consistent with alignment.

4.2 Introduction

With more than 4000[2] planets confirmed to date, the field of exoplanets has experienced a huge growth since its beginning two decades ago. This large number of discoveries has in particular been the product of extensive ground- and space-based transit photometry surveys, such as the missions of HAT (Bakos et al., 2004), WASP (Pollacco et al., 2006), CoRoT (Barge et al., 2008), Kepler (Borucki et al., 2010) and K2 (Howell et al., 2014). However, because of saturation limits, these surveys have for the most part been unable to monitor the brightest stars.

Transiting planets orbiting bright stars are important since they offer follow-up opportunities not available for fainter sources, allowing for detailed characterisation of their atmosphere and the system's orbital architecture. This includes the detection of e.g. water in the planetary atmosphere through high-resolution transmission spectroscopy (e.g. Snellen et al., 2010) and measurements of its spin-orbit angle through observations of the Rossiter-McLaughlin effect.

From space, the brightest exoplanet host stars are currently being probed thanks to the launch of *TESS* (Ricker et al., 2015), while ground-based projects doing the same include KELT (Pepper et al., 2007) and the MASCARA (the Multi-Site All-sky CAmeRA) survey (Talens et al., 2017). The latter aspires to find close-in transiting giant planets orbiting the bright stars well suited for detailed atmospheric characterisation. This has so far led to the discovery and characterisation of MASCARA-1, MASCARA-2 and MASCARA-4, three hot Jupiters orbiting A-type stars (Talens et al., 2017, 2018; Dorval et al., 2019).

Here we report the discovery, confirmation and characterisation of the MASCARA-3 system[3], the fourth planetary system found through the MASCARA survey. MASCARA-3b is a hot Jupiter with a 5.6 day period, and orbits a bright late F-type star ($V = 8.33$). In Sec. 4.3 the discovery observations from MASCARA and the spectroscopic follow-up observations with SONG (Stellar Observation Network Group, Andersen et al., 2014) are described. The analysis and results

[2] http://exoplanet.eu

[3] During the final preparations for the manuscript of which this chapter is based, we learned of the publication of the discovery of the same planetary system by the KELT-team; KELT-24 (Rodriguez et al., 2019)

on the host star are presented in Sec. 4.4, while Sec. 4.5 contains the investigation and characterisation of its planet. The results are presented and discussed in Sec. 4.6.

4.3 Observations

In this section two different kinds of observations are presented: the MASCARA photometry and the SONG spectroscopy (see Table 4.1).

4.3.1 MASCARA

The MASCARA survey is described in Talens et al. (2017). In short, it consists of two instruments: one covering the northern sky at the Observatory del Roque de los Muchachos (La Palma, Spain) and one targeting the southern hemisphere located at the European Southern Observatory (La Silla, Chile). Each instrument consists of five wide-field CCD's, which record images of the local sky throughout the night employing 6.4 sec exposure times. Aperture astrometry is performed on all known stars brighter than $V = 8.4$. The light curves are extracted from the raw flux following the procedure described in Talens et al. (2018), and transit events are searched for using the Box Least-Square (BLS) algorithm of Kovács et al. (2002). MASCARA-3 has been monitored since early 2015 by the northern instrument, totalling more than 27247 calibrated photometric data points, each consisting of 50 binned 6.4 second measurements (i.e. 320 sec per data point). A frequency analysis was performed on the light curve measurements by computing its BLS periodogram, revealing a peak at a period of 5.55149 days. Phasefolding the light curve using this period, we performed a preliminary analysis on the system, obtaining parameter values useful for spectroscopic follow-up (see Table 4.2). The resulting phasefolded lightcurve is shown in Fig. 4.1.

4.3.2 SONG

Succeeding the transit detection in the light curve of MASCARA-3, follow-up spectroscopy was executed using the robotic 1 meter Hertzsprung SONG telescope (Andersen et al., 2019) at Observatory del Teide (Tenerife, Spain). The observations were done in order to validate and characterise the planetary system. The telescope is equipped with a high-resolution echelle spectrograph which covers the wavelength range $4400 - 6900$Å. A total of 110 spectra were obtained between April 2018 and May 2019, employing a slit width of 1.2 arcsec resulting in a resolution of $R \sim 77,000$. The exposure times had been varied between 600 and 1800 sec. We used longer exposure times out-of-transits and shorter exposure times during transits to reduce phase smearing. 45 of the observations were gathered during two planetary transits occuring on May 29, 2018 and November 28, 2018. For the first transit our spectroscopic observations cover the entire transit. However, due to bad weather only a single spectrum was taken out-of-transit. On the second night we obtained a partial transit and post egress spectra.

Since we planned to analyse the RM effect in this system using only the Doppler Tomography technique, we did not use an iodine cell for observations taken during transit nights, but sandwiched each observation with ThAr exposures for wavelength calibration. From these spectra we obtained cross-correlation functions (CCFs) and Broadening Functions (BFs; Rucinski, 2002). Spectra not taken during transit nights were obtained with an iodine cell inserted into the light path for high RV precision.

The spectra and radial velocity (RV) extraction was performed following Grundahl et al. (2017). The RV data points are estimated to have internal instrumental uncertainties of ~ 31 m sec^{-1}. The resulting out-of-transit RVs and their uncertainties are listed in Table A1.

Table 4.1: Observation log of MASCARA-3 containing the different types of observation, instrument, no. of observations made and observing dates.

Type	Inst.	No. of obs.	Obs. date
Phot.	MASCARA	27247	February 2015 – March 2018
RV Spec.	SONG	65	April 2018 – May 2019
RM Spec.	SONG	23	May 29, 2018
RM Spec.	SONG	22	Nov 28, 2018

Table 4.2: Best fit values for the *initial* analysis of the MASCARA photometric data, with the eccentricity kept fixed at 0. Of these parameters, P and T_0 were used as priors in the joint fit between the spectroscopy and phasefolded photometry.

Parameter	Value
Orbital period, P (days)	5.55149 ± 0.00002
Time of mid-transit, T_0 (BJD)	$2458268.455^{+0.002}_{-0.003}$
Total transit duration, T_{14} (hr)	4.3 ± 0.1
Scaled planetary radius, $R_\mathrm{p}/R_\star$	0.091 ± 0.002
Scaled orbital distance, $a/R_\star$	$10.4^{+0.4}_{-1.0}$
Orbital inclination, i (deg)	88 ± 1.0
Impact parameter, b	0.3 ± 0.2

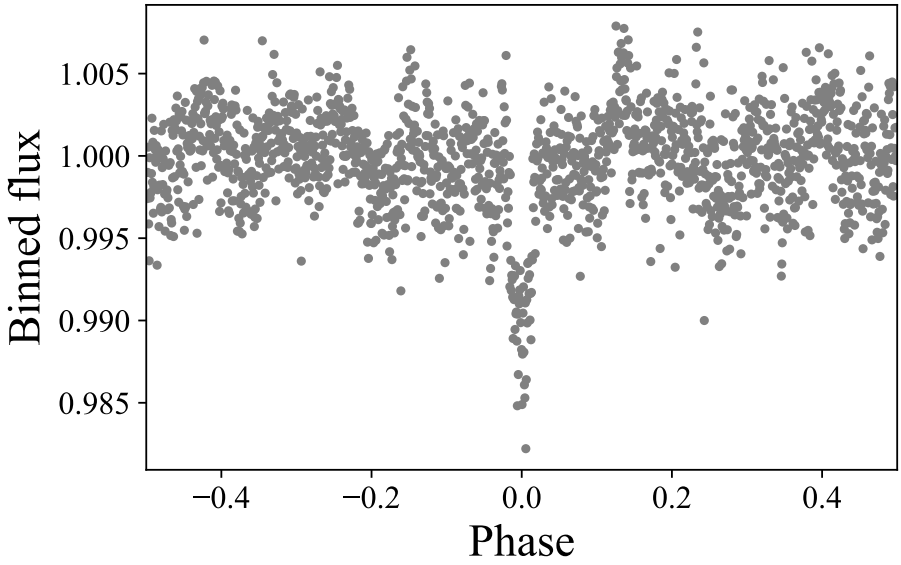

Figure 4.1: Calibrated and phasefolded MASCARA-3 photometry. The phase-folded data have been binned to 5 min. intervals, reducing the number of data points from 27247 to 1596. The period of 5.55149 days used in the phasefolding is the highest peak obtained from constructing the BLS periodogram of the data.

4.4 Stellar characterisation

We determined the spectroscopic effective temperature $T_{\rm eff} = 6415 \pm 110$ K and metallicity [Fe/H] $= 0.09 \pm 0.09$ dex using `SpecMatch-emp` (Yee et al., 2017), classifying it as an F7 star. `SpecMatch-emp` compares the observed spectrum with an empirical spectral library of well-characterised stars. Using the BAyesian STellar Algorithm `BASTA` (Silva Aguirre et al., 2015) with a grid of BaSTI isochrones (Pietrinferni et al., 2004; Hidalgo et al., 2018), we combined the spectroscopically derived $T_{\rm eff}$ and [Fe/H] with the 2MASS JHK magnitudes (see Table 4.3) and *Gaia* DR2 parallax ($\pi = 10.33 \pm 0.11$ mas) to obtain a final set of stellar parameters. Given the proximity of the star we assumed zero extinction along the line of sight. This way we derived a stellar mass $M_\star = 1.30^{+0.04}_{-0.03} M_\odot$, radius $R_\star = 1.52^{+0.03}_{-0.02} R_\odot$, and stellar age $= 2.8^{+0.5}_{-0.6}$ Gyr. We note that the uncertainties on the stellar parameters do not include systematic effects due to the choice of input physics in the stellar models. The model-dependent systematic uncertainties are at a few percent level.

Table 4.3: Literature and best-fit parameters for the stellar analysis of MASCARA-3. Sources: *Extracted from *Gaia* DR2 (Gaia Collaboration, 2018, https://gea.esac.esa.int/archive/). †Parameters from 2MASS (Cutri et al., 2003). ‡From the Tycho catalogue (Høg et al., 2000). The remaining parameter values are from this work.

Parameter	Value
Identifiers	HD 93148
Spectral type	F7
Right ascension, α (J2000.0)*	$10^{\rm h}\ 47^{\rm m}\ 38.351^{\rm s}$
Declination, δ (J2000.0)*	$+71^\circ\ 39'\ 21.16''$
Parallax, π (mas)*	10.3±0.1
Distance (pc)*	97±1
V-band mag., $V^\dagger$	8.33±0.01
J-band mag., $J^\ddagger$	7.41±0.02
H-band mag., $H^\ddagger$	7.20±0.04
K-band mag., $K^\ddagger$	7.15±0.02
Effective temperature, $T_{\rm eff,\star}$ (K)	6415 ± 110
Surface gravity $\log g_\star$ (cgs)	$4.18^{+0.01}_{-0.02}$
Metallicity, [Fe/H] (dex)	0.09 ± 0.09
Age (Gyr)	$2.8^{+0.5}_{-0.6}$
Stellar mass, $M_\star$ ($M_\odot$)	$1.30^{+0.04}_{-0.03}$
Stellar radius, $R_\star$ ($R_\odot$)	$1.52^{+0.03}_{-0.02}$
Stellar density, $\rho_\star$ (g cm^{-3})	$0.52^{+0.04}_{-0.03}$

4.5 Photometric and spectroscopic analysis

The overall analysis of the photometry and RV data is done in a similar fashion as for MASCARA-1b (Talens et al., 2017) and MASCARA-2b (Talens et al., 2018) and is outlined in the following section. Given the transit phase coverage and low Signal-to-Noise Ratio (SNR) of the RM detection we modified our analysis for this data set accordingly. We give details on that in Sec. 4.5.2.1 and 4.5.2.2.

4.5.1 Joint photometric and RV analysis

The binned, phasefolded MASCARA light curve is modelled employing the model by Mandel and Agol (2002), using a quadratic limb-darkening law. The free parameters for the transit model are the orbital period (P), a particular mid-transit time (T_0), the semi-major axis scaled by the stellar radius ($a/R_\star$), the scaled planetary radius ($R_p/R_\star$), the orbital inclination (i), the eccentricity (e) and the argument of periastron (ω) and finally the quadratic limb-darkening parameters (c_1) and (c_2). For efficiency, the inclination, eccentricity and argument of periastron are parameterized through $\cos i$, $\sqrt{e}\cos\omega$ and $\sqrt{e}\sin\omega$.

For the modelling of the RV observations, we only use spectra obtained with an iodine cell insert in the light path (Table A1). This excludes data taken during

transit nights. The RV data is compared to a Keplerian model where the stellar RV variations are caused by the transiting object. The additional parameters needed to describe the RV data are the RV semi-amplitude (K) and a linear offset in RV (γ). In addition, we allow for a linear drift of the RV data points, $\dot{\gamma}$, caused by e.g. a long-period unseen companion.

To characterise the planetary system we jointly model the light curve and the RVs. Since we fit to the *phasefolded* light curve, we impose Gaussian priors $P = 5.55149 \pm 0.00002$ days and $T_0 = 2458268.455^{+0.002}_{-0.003}$ BJD retrieved from the photometric analysis described in Sec. 4.3. In addition we impose Gaussian priors of $c_1 = 0.3797$ and $c_2 = 0.2998$ (Claret and Bloemen, 2011; Eastman et al., 2013) with a conservative uncertainties of 0.1. Furthermore, by using the spectroscopic value of the density $\rho_\star = 0.52^{+0.04}_{-0.03}$ g cm^{-3} as a prior, we can constrain the orbital shape and orientation (see e.g. Van Eylen and Albrecht, 2015, and references therein).

The log-likelihood for each data set is given as

$$\ln \mathcal{L} = -\frac{1}{2} \sum_{i=1}^{N} \left(\ln \left(2\pi \left[\sigma_i^2 + \sigma_{\rm jit}^2 \right] \right) + \frac{\left[O_i - C_i \right]^2}{\left[\sigma_i^2 + \sigma_{\rm jit}^2 \right]} \right) \tag{4.1}$$

with O_i and C_i being the i'th of N data and model points in each data set. For the two data sets we introduce two jitter terms $\sigma_{\rm jit,p}$ and $\sigma_{\rm jit,RV}$ to capture any unaccounted noise. These jitter terms are added in quadrature to the internal errors σ_i when calculating the maximum likelihood. The total log-likelihood is the sum of Eq. 4.1 for the photometry and RV together with an additional likelihood term accounting for priors.

The posterior distribution of the parameters are sampled through `emcee`, an MCMC multi-walker Python package (Foreman-Mackey et al., 2013). We initialize 200 walkers close to the maximum likelihood. They are evaluated for 10 000 steps, with a burn-in of 5000 steps which we disregard. By visually inspecting trace plots we have checked that the solutions have converged at that point. In Table 4.4 we report the maximum likelihood values of the MCMC sampling. The quoted uncertainty intervals represent the range that excludes 15.85% of the values on each side of the posterior distribution and encompass 68.3% of the probability. Figures 4.2 and 4.3 display the data and best-fit models for the joint analysis of the light curve and the RVs. We note that performing the same analysis without a prior on the stellar density reveals results consistent within 1σ.

4.5.2 Analysing the stellar absorption line

Modelling the stellar absorption lines is carried out in a similar way as was done in Albrecht et al. (2007) and Albrecht et al. (2013). However we modified our approach of comparing the model to the data. We did this because we found that BFs created from our data had a too low SNR to be useful in determining λ

Table 4.4: The best-fitting and derived stellar, planetary and system parameters for MASCARA-3. The parameters are extracted from the joint analysis on the photometry and RV (Sec. 4.5.1), the analysis on the mean out-of-transit BF (Sec. 4.5.2.1), the analysis on the grid of the shifted and binned Doppler shadow residuals (Sec. 4.5.2.2), and the analysis on the extracted RVs from the spectroscopic transit on the night of May 29, 2018 (Sec. 4.5.3).

Parameter	Value	Section
Fitting parameters		
Quadratic limb darkening (MASCARA), (c_1, c_2)	$(0.40 \pm 0.07, 0.31 \pm 0.07)$	4.5.1
Systemic velocity, γ (km s^{-1})	-5.63 ± 0.01	4.5.1
Linear trend in RV, $\dot{\gamma}$ (m s^{-1} yr^{-1})	61 ± 19	4.5.1
Orbital period, P (days)	5.55149 ± 0.00001	4.5.1
Time of mid-transit, T_0 (BJD)	2458268.455 ± 0.002	4.5.1
Scaled planetary radius, $R_\mathrm{p}/R_\star$	0.092 ± 0.003	4.5.1
Scaled orbital distance, $a/R_\star$	9.5 ± 0.2	4.5.1
RV semi-amplitude, $K_\star$ (m s^{-1})	415 ± 13	4.5.1
$\sqrt{e}\sin\omega$	$0.10^{+0.07}_{-0.09}$	4.5.1
$\sqrt{e}\cos\omega$	0.20 ± 0.04	4.5.1
$\cos i$	$0.042^{+0.012}_{-0.008}$	4.5.1
Jitter term phot., $\sigma_\mathrm{jit,p}$	0.0021 ± 0.0001	4.5.1
Jitter term RV, $\sigma_\mathrm{jit,RV}$ (km s^{-1})	0.060 ± 0.008	4.5.1
Quadratic limb darkening (SONG), ($c_\mathrm{1,s}$, $c_\mathrm{2,s}$)	$(0.66 \pm 0.09, 0.40 \pm 0.09)$	4.5.2.1
Microturbulence, β (km s^{-1})	4.3 ± 0.6	4.5.2.1
Macroturbulence, ζ (km s^{-1})	9.4 ± 0.4	4.5.2.1
Proj. rotation speed (BF), $v \sin i_\star$ (km s^{-1})	20.4 ± 0.4	4.5.2.2
Jitter term RM out-of-transit, $\sigma_\mathrm{jit,out}$ (m s^{-1})	0.003 ± 0.002	4.5.2.1
Proj. rotation speed (grid), $v \sin i_\star$ (km s^{-1})	20.9 ± 3.2	4.5.2.2
Projected obliquity (grid), λ (deg)	17.8 ± 20.0	4.5.2.2
Impact parameter (grid), b	0.30 ± 0.16	4.5.2.2
3D rotation angles (deg)	$(-1.4, -0.01, 0.002)$	4.5.2.2
Proj. rotation speed (RV-RM), $v \sin i_\star$ (km s^{-1})	20.3 ± 0.4	4.5.3
Projected obliquity (RV-RM), λ (deg)	$1.2^{+8.2}_{-7.4}$	4.5.3
Impact parameter (RV-RM), b	0.39 ± 0.08	4.5.3
RV offset on May 29, 2018, γ_RM (km/sec)	-15.181 ± 0.010	4.5.3
Derived parameters (from Sec. 4.5.1 results)		
Orbital eccentricity, e	$0.050^{+0.020}_{-0.017}$	
Argument of periastron, ω (deg)	27^{+38}_{-27}	
Orbital inclination, i (deg)	$87.6^{+1.0}_{-0.8}$	
Impact parameter, b	0.40 ± 0.10	
Total transit duration, T_{14} (hr)	4.55 ± 0.20	
Full transit duration, T_{23} (hr)	3.65 ± 0.23	
Semi-major axis, a (au)	0.067 ± 0.002	
Planetary mass, M_p (M_Jup)	4.2 ± 0.2	
Planetary radius, R_p (R_Jup)	1.36 ± 0.05	
Planetary mean density, ρ_p (g cm^{-3})	2.3 ± 0.3	
Equilibrium temperature, T_eq (K)	1473 ± 28	

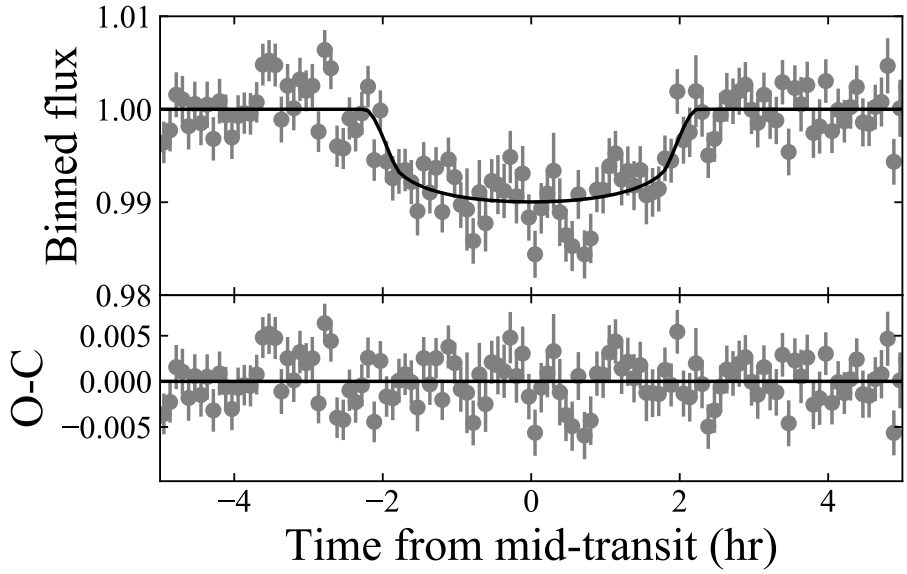

Figure 4.2: The phasefolded MASCARA-3 photometry data (grey) with the best-fit transit model (black) from the joint photometric and RV analysis. The corresponding best-fit parameters can be found in Table 4.4. The bottom plot displays the residuals.

through analysis of the RM effect. Nevertheless they more faithfully represent the width of the stellar absorption lines than the CCFs which have large "wings" (see Fig. 4.4). We have not been able to determine the exact underlying reason for this, but we suspect that the low SNR in the spectra is to blame. Determining the correct continuum level in low SNR high resolution spectra is extremely difficult. For the case of MASCARA-3, this problem is enlarged due to the fast stellar rotation and therefore wide stellar absorption lines. A mismatch in the continuum would lead to a low SNR in the derived BF. The same mismatch in the continuum correction would lead to enlarged "wings" in the CCFs. We therefore first obtained a measure for $v \sin i_\star$ by comparing our out-of-transit stellar line model to an average out-of-transit BF. We then analyze the planet shadow in the transit data.

Concerning the model for comparison to the out-of-transit and in transit data we did the following: We created a 201×201 grid containing a pixelated model of the stellar disk. The brightness of each pixel on the stellar disk is scaled according to a quadratic limb-darkening law with the parameters $c_{1,\mathrm{s}}$ and $c_{2,\mathrm{s}}$ and set to zero outside the stellar disk. Each pixel is also assigned a radial velocity assuming solid body rotation and a particular projected stellar rotation speed, $v \sin i_\star$. The RVs of each pixel are further modified following the model for turbulent stellar motion as described in Chapter 3. This model has two terms. A micro-turbulence term modelled by a convolution with a Gaussian, which σ-width we describe here with the parameter β. The second term in this model

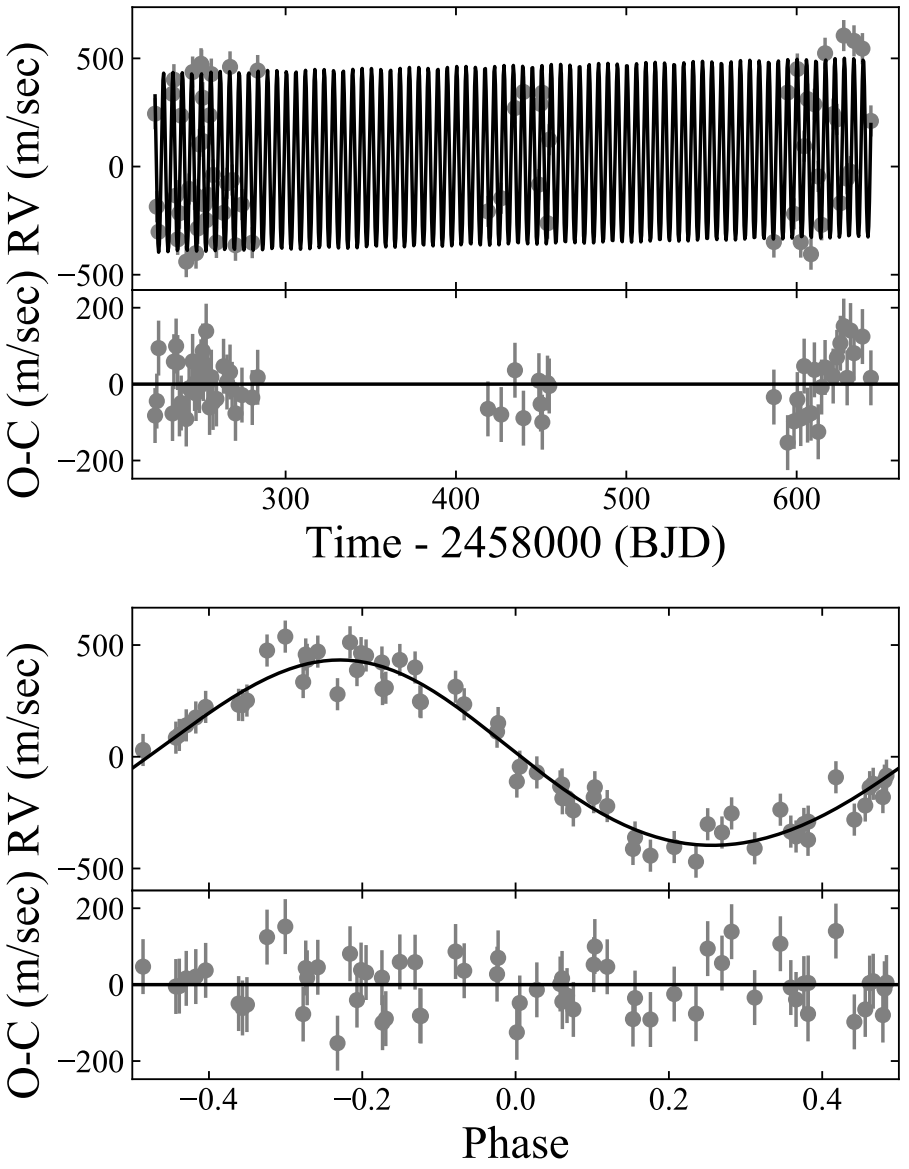

Figure 4.3: The RV data from the SONG telescope (grey) with the best-fit Keplerian model (black) from the joint photometric and RV analysis. The data is plotted as a function of time (upper plot) and phasefolded (lower plot), to highlight the fact that we allowed for the possibility of a linear trend in the RV. In the lower plot the best fitting RV trend was removed from the data and model. The best-fit parameters are displayed in Table 4.4. The bottom panel in both plots show the residuals.

encompasses radial and tangential macro turbulence surface motion. Its σ-width we assign the parameter ζ. The modelled stellar absorption line is then obtained by disk integration. Finally the Gaussian convolution also includes the Point Spread Function (PSF) of the spectrograph added in quadrature. Because of the low SNR of our spectra we do not include convective blueshift in our model.

4.5.2.1 *Out-of-transit stellar absorption line*

To measure $v \sin i_\star$ we compared our out-of-transit line model to the BFs taken out-of-transit. We used only data from the second transit night as little data was obtained out-of-transit during the first transit night (Fig. 4.5). In addition to the five model parameters, $c_{1,\mathrm{s}}$, $c_{2,\mathrm{s}}$, $v \sin i_\star$, β, and ζ, we also vary a jitter term $\sigma_{\mathrm{jit,out}}$ during the fitting routine. We impose Gaussian priors of $\beta = 2.7$ km sec^{-1} (Coelho et al., 2005) and $\zeta = 6.1$ km sec^{-1} (Gray, 1984), both with uncertainty widths of 0.5 km sec^{-1}. The best-fit parameters are again found by maximizing the log-likelihood from Eq. 4.1 using `emcee` in the same way as in Sec. 4.5.1. The best-fit parameters are given in Table 4.4, while the data and best-fit model are shown in Fig. 4.4.

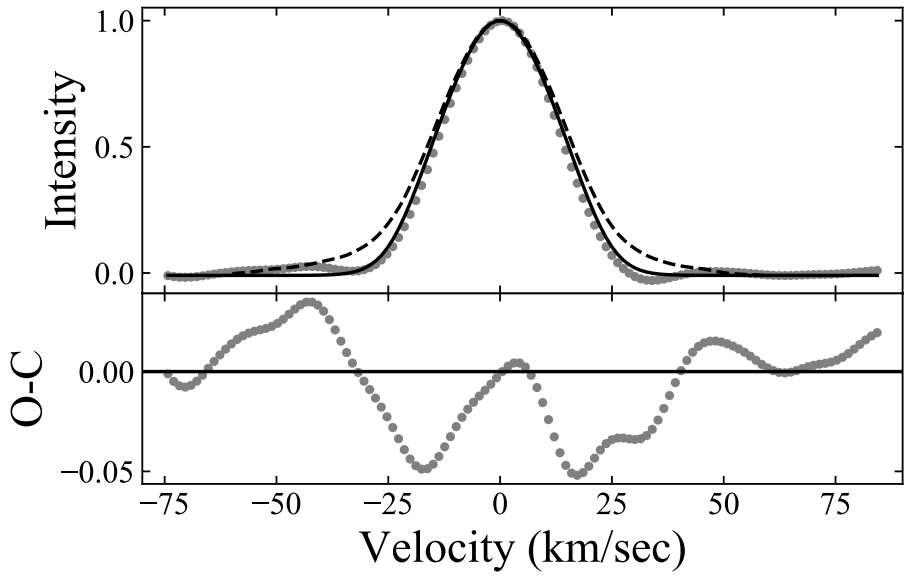

Figure 4.4: The mean out-of-transit BF (grey) with the best fitting stellar absorption line model (black). For comparison the dashed line shows the mean out-of-transit CCF, which erroneously leads to an enlarged line-width due to its "wings", which we assume are caused by a non-perfect normalisation of the low SNR spectra (see Sec. 4.5.2).

4.5.2.2 The Doppler shadow

We observed spectroscopic transits during the nights May 29, 2018 and Nov 28, 2018. This was done in order to validate the companion being a planet orbiting the host star and to obtain the projected spin-orbit angle λ of the system.

As described in Chapter 3, the planet will block some of the star during transit, deforming the absorption line by reducing the amount of blue- or red-shifted light visible to the observer at a particular phase of a transit. Subtracting the distorted in-transit absorption lines to the out-of-transit line will therefore reveal the planetary "shadow" cast onto the rotating stellar photosphere. For solid body rotation this shadow travels on a line in a time-velocity diagram and its zero point in velocity and orientation depends on the projected obliquity and projected stellar rotation speed, as well as the impact parameter (see Eq. 3.10 and 3.11). The planet shadows obtained during the two transit nights can be seen in Fig. 4.5. Here we have scaled and removed the average out-of-transit CCF from the second transit night from all observations. Clearly MASCARA-3 b travels on a prograde orbit. During the first half of the transit the distortion has negative RVs, and positive RVs during the second half of the transit. However as our detection of the planet shadow is of low SNR we do not strictly follow Albrecht et al. (2013) and Talens et al. (2017) in deriving λ. Rather we use an approach similar to the one pioneered by Johnson et al. (2014).

Sec. 3.4.1 gives a detailed description of this technique. In short, a dense 3D-grid is created consisting of $v \sin i_\star$, λ and the impact parameter b. For each of these ($v \sin i_\star$, λ, b) triples, we compute the RV rest frame of the sub-planetary point. For each observation the shadow data is then shifted into this RV rest frame. Subsequently the observations are collapsed and the signal from both nights is co-added. The closer the values for λ, $v \sin i_\star$ and b in the grid are to the actual values of these parameters, the more significant the peak will be. To illustrate this, Fig. 4.6 displays a 2D ($v \sin i_\star$, λ) contour plot with the peak values, using the best fit value of b from the analysis below.

To obtain the best-fit parameters for $v \sin i_\star$, λ and b, we now fit a 3D Gaussian to the 3D grid of peak values we have just obtained. For this 3D Gaussian fit we use, next to $v \sin i_\star$, λ and b, the width of the Gaussian in each direction $\sigma_{v \sin i_\star}$, σ_λ and σ_b, and nuisance rotation angles in each dimension. This way we obtain $v \sin i_\star = 20.9 \pm 3.2$ km s^{-1}, $\lambda = 17.8 \pm 20.0$ deg and $b = 0.30 \pm 0.16$, as reported in Table 4.4. When making the 3D grid, we kept the remaining shadow parameters fixed. At first sight this might suggest that we underestimate the uncertainties of $v \sin i_\star$, λ and b. However, for the remaining parameters, effects from their errors are negligible because they either 1) are of the order < 2 minutes, which is much smaller than the exposure time (P, T_0), 2) change only the RV offset of the shadow CCFs, which is accounted for when scaling and normalising it (e, ω, $K_\star$), 3) only introduce an overall normalisation offset or scaling of the 3D grid ($R_p/R_\star$, c_1, c_2), 4) are incorporated into b ($\cos i_\star$, $a/R_\star$). We are therefore confident of the obliquity being 17.8 deg within a 1σ uncertainty of 20.0 deg, but will in the

following section present how extractions of the RVs bring down this uncertainty. We prefer the $v \sin i_\star$ value obtained from the fit to the out-of-transit BF as our final value for the projected stellar rotation speed (Sec. 4.5.2.1), as it is hard to get a constraint on $v \sin i_\star$ from in-transit data alone.

4.5.3 Analysing the velocity anomaly

To obtain a better constraint on the obliquity than what was possible from the Doppler shadow, we examined the possibility of extracting the RVs from the spectroscopic transit observations. Despite getting large errors due to using ThAr during transit instead of an iodine cell, and though the RV errors are usually too high for this approach for rapid rotating stars, we were able to achieve an internal precision of 50 m s^{-1}. This precision coupled with the small baseline and low amount of data points meant that obtaining λ from the RVs was not possible for the transit night of Nov 28, 2018. However, it did prove sufficient for determining λ from the observations of the full transit on the night of May 29, 2018.

The RV anomaly due to the RM-effect was modelled following Hirano et al. (2011). During the fitting routine, we varied λ, $v \sin i_\star$ and b as well an RV offset for the specific night $\gamma_{\rm RM}$. We used the best-fitting values from the procedures described in Sec. 4.5.1 and 4.5.2 for the remaining parameters. We also applied a Gaussian prior of $v \sin i_\star = 20.4 \pm 0.4$ km s^{-1} from the analysis of the stellar absorption and a Gaussian prior of $b = 0.4 \pm 0.1$ from the RV and light curve analysis. We obtained $b = 0.39 \pm 0.08$, $v \sin i_\star = 20.3 \pm 0.4$ km s^{-1} and $\lambda = 1.2^{+8.2}_{-7.4}$ deg, consistent with the results from Sec. 4.5.2.2, but with a much better constraint on the spin-orbit angle. Due to the scarcity of out-of-transit data on the night of May 29, 2018, leaving K as an additional free parameter naturally made it poorly constrained, but nevertheless resulted in it being within 1σ of the results from Sec. 4.5.1. The RV-RM data are given in Table A2, and are shown in Fig. 4.7 together with the best-fit model. The best-fit parameter values are displayed in Table 4.4, and obtained in the same way as in the previous sections.

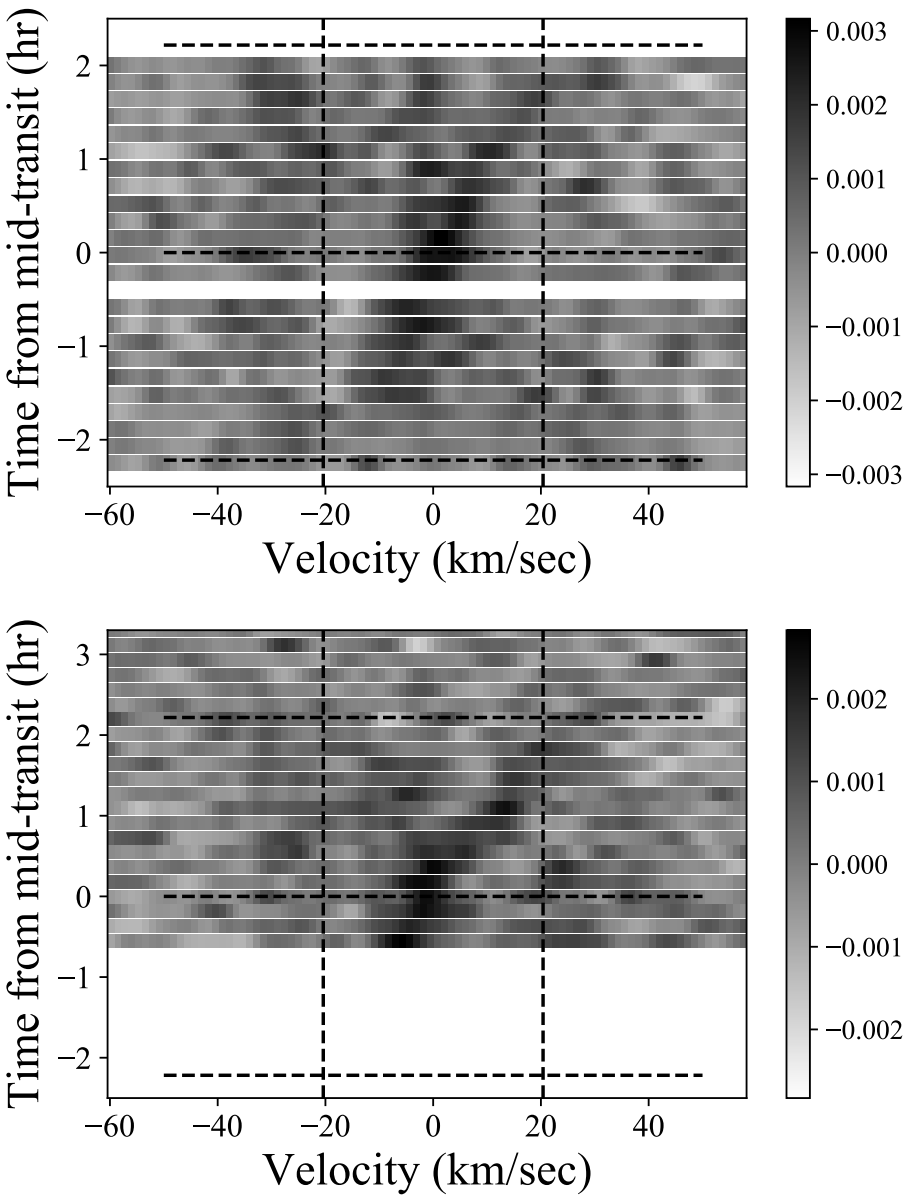

Figure 4.5: The spectroscopic transit of MASCARA-3 observed on the night of May 29, 2018 (upper plot) and Nov 28, 2018 (lower plot). Both plots show the observed CCFs, with the subtraction of the mean out-of-transit CCF obtained from the second night. Before subtraction, these CCFs are scaled and offset to their model-counterpart in intensity (all CCFs) and scaled in velocity-space (in-transit CCFs), in order to account for uneven normalisation due to differences in flux-levels and PSF changes. The vertical dashed lines mark the best-fit value of the $v \sin i_\star$ from the BF analysis, while the horizontal dashed lines mark the best-fit value for the transit ingress, mid-transit time and egress.

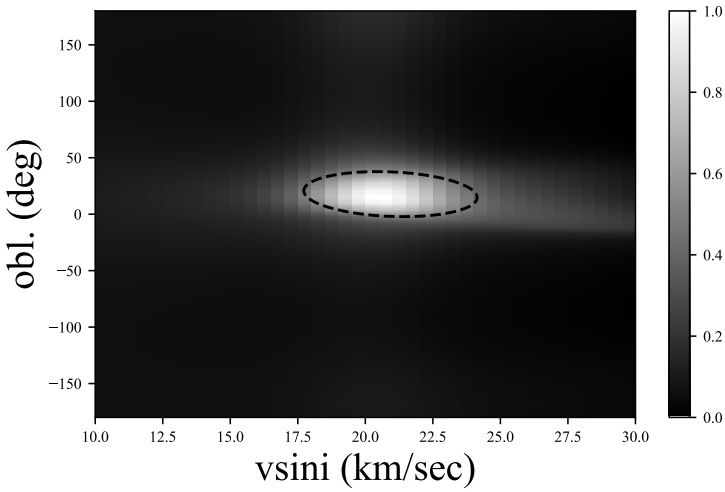

Figure 4.6: The concentration ($v \sin i_\star$, λ) grid for the best-fit value of b together with the best-fit 1σ 2D Gaussian model (dashed). For each ($v \sin i_\star$, λ, b) triple the grid values are constructed by shifting the model and shadow bump a corresponding amount, such that the model shadow bump is centered at zero. This is followed by collapsing the shifted data shadow in intensity space. The contour signal at a specific ($v \sin i_\star$, λ, b) value is then the resulting value of the collapsed, shifted data shadow at a velocity of zero.

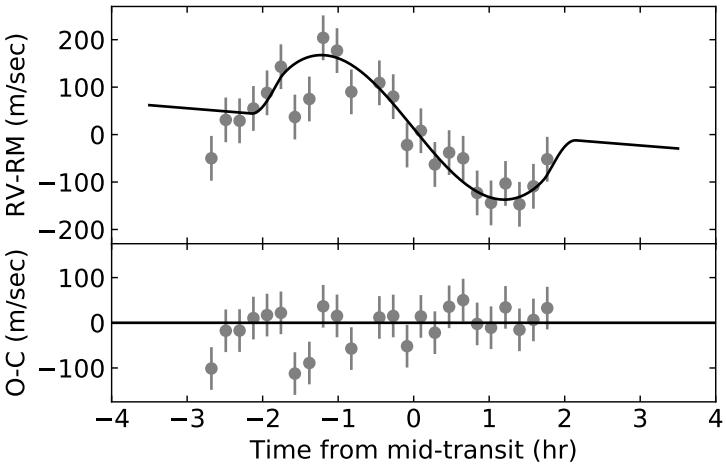

Figure 4.7: The radial velocities from the night of May 29, 2018 together with the best-fit model of the velocity anomaly. The uncertainties of ~ 50 m sec^{-1} are higher than those of Fig. 4.3 due to the calibrations during transit being performed with ThAr instead of the iodine cell.

4.6 Discussion and conclusions

From the joint photometry and RV analysis we obtain a planetary mass of $4.2 \pm 0.2\ M_{\rm Jup}$ and a planetary radius of $1.36 \pm 0.05\ R_{\rm Jup}$. The planet revolves around its host star in an almost circular orbit ($e = 0.085^{+0.023}_{-0.022}$) every 5.55149 ± 0.00001 days at a distance of 0.067 ± 0.002 au, making MASCARA-3b a hot Jupiter. With an incident flux of $F = (10.6 \pm 0.9) \cdot 10^8$ erg s^{-1} cm^{-2} above the inflation threshold of $F = 2 \cdot 10^8$ erg s^{-1} cm^{-2} (Demory and Seager, 2011), the planet might be affected by inflation mechanisms, despite having a mean density above that of Jupiter.

It is still unclear whether hot Jupiters primarily originate from high-eccentricity migration or disk migration (see Chapter 2). The former process would lead to at least occasionally large obliquities while the latter process would lead to low obliquities, assuming good alignment between stellar spin and angular momentum of the protoplanetary disks. However the interpretation of hot Jupiter obliquities might be more complicated than originally thought. This is because tidal interactions might have aligned the stellar spin and the orbital angular momentum in some of the systems, in particular in systems where the host stars have a convective envelope, leading to fast alignment of the planets orbital spin with the stellar rotation (Winn et al., 2010; Albrecht et al., 2012).

With an effective temperature of $T_{\rm eff,\star} = 6415 \pm 110$ K, MASCARA-3 will have a relatively slow alignment timescale for a hot Jupiter of its mass and distance. It is also interesting to note that the orbital eccentricity suggests a near circular orbit. MASCARA-3 b appears to belong to a dynamically cold population consistent with an arrival at its current orbit via disk migration instead of high-eccentricity migration.

While finalising the manuscript of which this chapter is based we learned of another paper reporting the discovery of this planet-star system published by the KELT team. Though no observations or analyses were shared, the planet and system parameters from each group are for the most part in agreement. The only major difference is the RV semi-amplitude, and thereby the derived planetary mass.

5

K2-290: a warm Jupiter and a mini-Neptune in a triple star system

With an example of the capabilities of the Rossiter-McLaughlin effect through both the velocity anomaly and Doppler Tomography techniques demonstrated in the previous chapter, the next step is to conduct further observations, which might help shed light on the origin of hot Jupiters. This can be done by testing the assumption of primordial spin-alignment of the disk in planetary systems. To do this, the first task is to expand the sample of warm Jupiters or multi-planet systems suited for Rossiter-McLaughlin observations (see Chapter 2). In this chapter *both* samples are expanded with the discovery and characterisation of K2-290. This is a multi-planet system containing a warm Jupiter and a mini-Neptune in addition to it's host star and two stellar companions. This chapter was published in Monthly Notices of the Royal Astronomical Society (Hjorth et al., 2019)[1], and is presented here with only minor changes. I have written the manuscript and in addition done the majority of the analysis, with the exception of extracting the RVs (done by co-author Gandolfi), analysing the AO imaging presented in section 5.3.3 and parts of section 5.4.2 (done by co-author Hirano) and doing an analysis of the three stars in the system in section 5.3.3 and parts of section 5.4.2 (done by co-author Justesen). In section 5.4.2 I did however perform the analysis presented in the last paragraph, showing that the companion stars are bound to the host star.

[1]Authors: Hjorth, M., Justesen, A. B., Hirano, T., Albrecht, S., Gandolfi, D., Dai, F., Alonso, R., Barragán, O., Esposito, M., Kuzuhara, M., Lam, K. W. F., Livingston, J. H., Montanes-Rodriguez, P., Narita, N., Nowak, G., Prieto-Arranz, J., Redfield, S., Rodler, F., Van Eylen, V., Winn, J. N., Antoniciello, G., Cabrera, J., Cochran, W. D., Csizmadia, Sz, de Leon, J., Deeg, H., Eigmüller, Ph, Endl, M., Erikson, A., Fridlund, M., Grziwa, S., Guenther, E., Hatzes, A. P., Heeren, P, Hidalgo, D., Korth, J., Luque, R., Nespral, D., Palle, E., Pätzold, M., Persson, C. M., Rauer, H., Smith, A. M. S., Trifonov, T.

5.1 Summary

We report the discovery and characterisation of two transiting planets orbiting K2-290 (EPIC 249624646), a bright (V=11.11) late F-type star residing in a triple star system. It was observed during Campaign 15 of the *K2* mission, and in order to confirm and characterise the system, follow-up spectroscopy and AO imaging were carried out using the FIES, HARPS, HARPS-N, and IRCS instruments. From AO imaging and *Gaia* data we identify two M-dwarf companions at a separation of 113 ± 2 AU and 2467^{+177}_{-155} AU. From radial velocities, *K2* photometry, and stellar characterisation of the host star, we find the inner planet to be a mini-Neptune with a radius of 3.06 ± 0.16 $R_\oplus$ and an orbital period of $P = 9.2$ days. The radius of the mini-Neptune suggests that the planet is located above the radius valley, and with an incident flux of $F \sim 400$ $F_\oplus$, it lies safely outside the super-Earth desert. The outer warm Jupiter has a mass of $0.774 \pm 0.047 M_J$ and a radius of $1.006 \pm 0.050 R_J$, and orbits the host star every 48.4 days on an orbit with an eccentricity $e < 0.241$. Its mild eccentricity and mini-Neptune sibling suggest that the warm Jupiter originates from *in situ* formation or disk migration.

5.2 Introduction

With the success of the *Kepler* mission (Borucki et al., 2010), exoplanetary science entered a new era. With the breakdown of its second reaction wheel in 2013, the spacecraft continued operating through the *K2* mission (Howell et al., 2014). Because of its monitoring of fields at the ecliptic in timeslots of $\sim$ 80 days, the *K*2 mission has been able to target an area of the sky, which will have limited coverage in the *TESS* mission (Ricker et al., 2015). Combined, *Kepler* and *K2* have to date discovered more than 2500 confirmed planets[2] – an essential achievement for our understanding of these new worlds.

Of the large number of exoplanets discovered, some are very different from the Solar System planets. This is e.g. the case for super-Earths and mini-Neptunes, which have sizes between Earth and Neptune, and for hot and warm Jupiters, which are Jupiter-sized planets with orbital periods of < 10 days and between 10 and ~ 200 days, respectively. As discussed in Chapter 2 our understanding of the formation of these planets is still limited. In the case of hot Jupiters it appears as if they formed at significantly larger orbits than where we find them now, but their migration mechanism(s) is yet to be determined . Planetary migration via angular momentum exchange with the protoplanetary disk (e.g. Lin et al., 1996) would lead to low eccentricity orbits roughly aligned with the disk midplane. Whereas high-eccentricity migration (e.g. Rasio and Ford, 1996) would lead to large eccentricities ($\gtrsim 0.2$) and orbits outside the disk midplane. Interpretation of these orbital parameters in the framework of planet formation and migration is however complicated by tidal damping of orbital eccentricities (e.g. Bonomo et al., 2017) and by tidal alignment of orbital and stellar spins (Winn et al., 2010;

[2] https://nasa.gov/mission_pages/kepler

Albrecht et al., 2012), the latter being under debate (see Zanazzi and Lai (2018a) and references therein).

Some warm Jupiters might be progenitors of hot Jupiters, but their orbits will be altered less by tidal damping due to the larger separations from the host stars (Petrovich and Tremaine, 2016). In addition, studying the eccentricity (Dong et al., 2014) and companionship (Huang et al., 2016) of warm Jupiter systems, it has been proposed that warm Jupiters originate from two different formation paths: high-eccentricity migration (i.e. as hot Jupiter progenitors) and *in situ* formation. If they originate from high-eccentricity migration these are predicted to have undergone secular eccentricity oscillations by the hand of an outer close-by high-mass companion and have high eccentricities (> 0.4; Dong et al., 2014; Petrovich and Tremaine, 2016) and no low-mass inner companions (Mustill et al., 2015), while if they form *in situ* they should have low eccentricities (< 0.2; Petrovich and Tremaine, 2016) and inner low-mass siblings with low mutual inclinations (Huang et al., 2016). Determinating companionship and orbital eccentricities should therefore shed light on the origin of both hot and warm Jupiters (see Dawson and Johnson, 2018, and references therein).

In the case of warm and hot Jupiters forming through dynamical pertubations of their orbits, the formation might be somewhat more efficient within a triple star system than in binary star systems (see Hamers, 2017, and references therein). However, only a couple dozens of planetary systems have been confirmed to be in triple star systems[3]. We are only aware of two of these having multiple planets: GJ 667C (Anglada-Escudé et al., 2012; Feroz and Hobson, 2014) and Kepler-444A (Campante et al., 2015), both of which contain no giant planets.

Here we present the discovery, confirmation and characterisation of the multi-transiting planet system K2-290 (EPIC 249624646) detected by the *K2* mission. K2-290b is a mini-Neptune on a ~ 9.2 day orbit, while K2-290c is a warm Jupiter with an orbital period of ~ 48.4 days. They both orbit the bright late F-type subgiant K2-290 ($V = 11.11$), which in turn have two stellar companions, probably as a member of a triple star system. We used a combination of *Kepler* photometry, high-resolution spectrocopy from FIES, HARPS and HARPS-N and AO imaging from IRCS to detect and characterise the planets and their orbits. This was done as part of the KESPRINT collaboration[4], which aims to confirm and characterise *K2* and *TESS* systems (see e.g. Van Eylen et al., 2018; Livingston et al., 2018; Johnson et al., 2018).

The next sections are structured in the following way: In section 5.3 the observational data consisting of photometry, spectroscopy and AO imaging are presented. The analysis of the host star and its two companions is presented in section 5.4, while section 5.5 deals with the planetary confirmation and characterisation of K2-290b and K2-290c. In section 5.6 our findings are discussed and put into context.

[3] Catalogue introduced in Schwarz et al. (2016)
[4] `https://iac.es/proyecto/kesprint/`

5.3 Observations

To detect, characterise and analyse the planets and stars in the system, we use several different types of observations. This includes photometry, high-resolution spectroscopy, and AO imaging. An overview of the data sources and data characteristics can be found in Table 5.1. A detailed description of the observations are given in this section.

Table 5.1: Observation log of K2-290 containing the different types of observation, instrument, instrument resolution, no. of observations made and observing dates. **Notes**:[1]The original no. of observations.

Type	Inst.	Spec. res.	No. of obs.	Obs. date
Phot.	*Kepler*	–	3909[1]	2017 8/23 – 11/20
Spec.	HARPS	115000	16	2018 2/23 – 5/12
	HARPS-N	115000	6	2018 2/20 –7/14
	FIES	47000	11	2018 5/12 – 7/13
Imaging	IRCS	–	2	2018 3/29 & 6/14

5.3.1 *K2* photometry

The star K2-290 was observed by the Kepler space telescope in Campaign 15[5] of the *K2* mission (Howell et al., 2014). A total of 3909 long-cadence observations (29.4 min integration time) were made of this target between August 23 and November 20 2017. For a detailed analysis, we downloaded the pre-processed lightcurve from MAST[6], which is reduced from the raw data following the procedure described in Vanderburg and Johnson (2014). The search method for transiting exoplanet candidates in the *K2* data is described in Dai et al. (2017), which follows a similar approach as Vanderburg and Johnson (2014).

Two transit signatures were detected in the lightcurve of K2-290 with periods of ~ 9.2 days and ~ 48.4 days and depths of $\sim 0.03\%$ and $\sim 0.5\%$, respectively (see Fig. 5.6). This is consistent with a mini-Neptune or super-Earth and a warm Jupiter orbiting a slightly evolved F8 star.

The out-of-transit signal is fairly quiet: we find no evidence of recurring stellar spots and in general no signs of any additional periodic signals in the lightcurve.

5.3.2 Spectroscopy

Spectroscopic observations of K2-290 were carried out between 2018/02/20 and 2018/08/28 using the FIES, HARPS, and HARPS-N spectrographs.

[5]Guest observer programmes GO15009_LC, GO15021_LC, GO028_LC and GO083_LC.
[6]https://archive.stsci.edu/prepds/k2sff

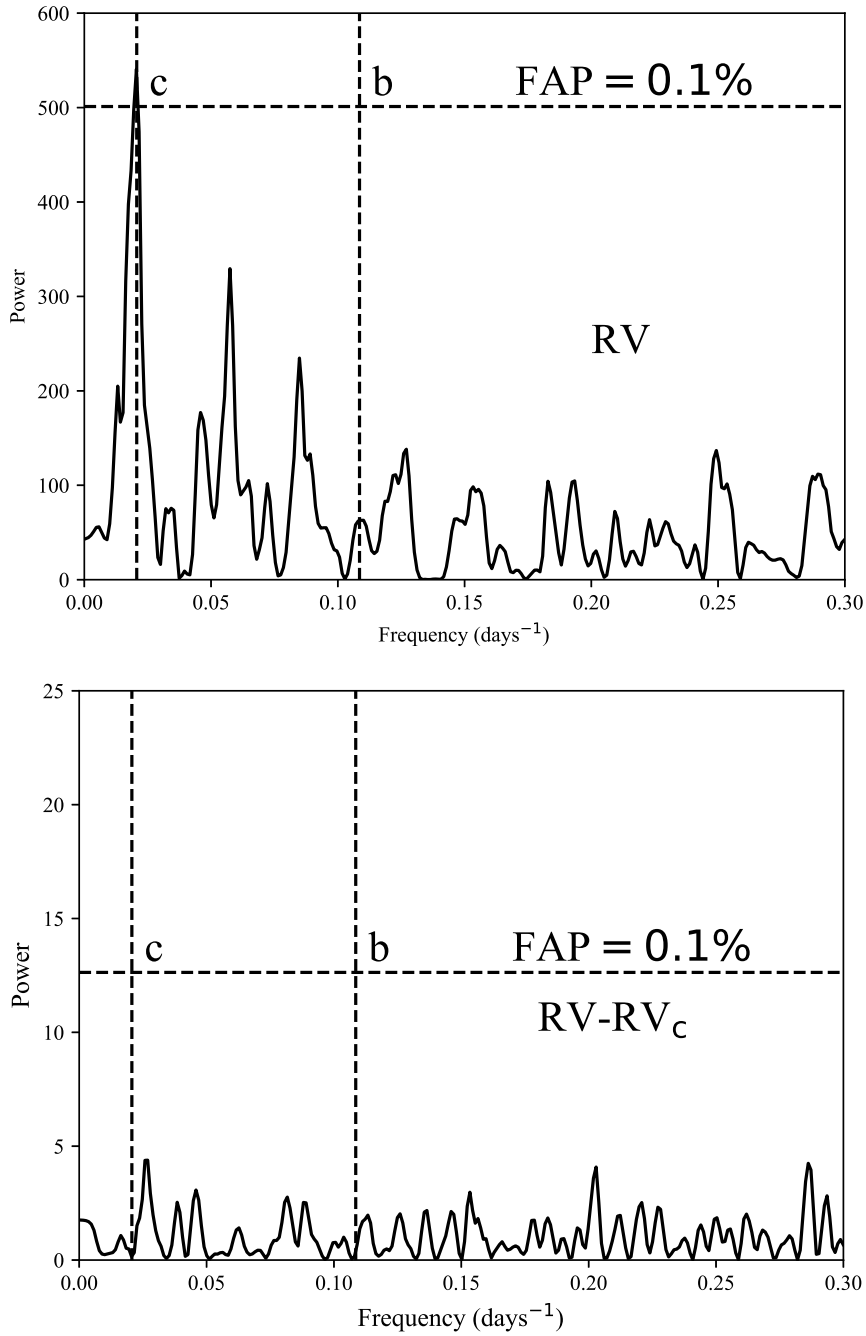

Figure 5.1: The GLS periodograms of the RVs using offsets subtracted data only (upper plot) and additionally the best-fitting keplerian model for planet c subtracted (lower plot). The dashed vertical lines mark the frequencies at which we expect to find the signals for planet b and c, given the orbital periods from the photometric data. The dashed horizontal lines indicate the respective 0.1% false alarm probabilities.

The FIES (Fiber-fed Echelle Spectrograph; Telting et al., 2014) spectra were gathered between 2018/05/12 and 2018/07/13 at the 2.56 m Nordic Optical Telescope (NOT) of Roque de los Muchachos Observatory, La Palma, Spain. We obtained 11 med-resolution spectra ($R \sim 47000$) as part of the Nordic and OPTICON programmes 57-015 and 2018A/044, using the observing strategy described in Gandolfi et al. (2013). The spectra were reduced using standard IRAF and IDL[7] routines, and radial velocities (RVs) were extracted through fitting Gaussians to multi-order cross-correlation functions (CCFs) using the stellar spectrum with the highest S/N as template.

Between February 23 and August 28 2018, we also obtained 16 high-resolution ($R \sim 115000$) spectra with the High Accuracy Radial velocity Planet Searcher spectrograph (HARPS; Mayor et al., 2003) mounted at the ESO 3.6 m telescope of La Silla observatory. The spectra were gathered in connection with the ESO programmes 0100.C-0808 and 0101.C-0829. The data were reduced using the offline HARPS pipeline. The RVs were extracted through cross-correlations of the processed spectra with a G2 numerical mask (Pepe et al., 2002).

We further used the HARPS-N spectrograph (Cosentino et al., 2012) installed at the 3.6 m Telescopio Nazionale Galileo (TNG) of the Roque de los Muchachos Observatory, La Palma, Spain. Here we collected 6 high-resolution ($R \sim 115000$) spectra between 2018/02/20 and 2018/07/14 as part of the Spanish and TAC programmes CAT17B_99, CAT18A_130, and A37TAC_37. The data were reduced and RVs extracted using the same procedure as done for the HARPS data.

In total, 33 spectra were obtained and reduced. In Table A3 we list the barycentric time of mid-exposure, the RVs, the RV uncertainties (σ_{RV}), the bisector span (BIS) and the full-width at half maximum (FWHM) of the CCFs, the exposure times, the signal-to-noise ratios (S/N) per pixel at 5500 Å, and the instrument used for a specific observation.

We performed a frequency analysis of the RV measurements to test whether the two transiting planet candidates are detectable in the spectroscopic data. This was done by computing the generalized Lomb-Scargle (GLS) periodogram (Zechmeister and Kürster, 2009) of the combined FIES, HARPS, and HARPS-N measurements. The RV data were first corrected for the instrument offsets using the values derived from the global analysis described in Sec. 5.5.4. The GLS periodogram (Fig. 5.1, upper plot) shows a significant peak at the orbital frequency of planet c (false alarm probability FAP $< 0.1\%$, calculated using the bootstrap method from Kuerster et al., 1997), indicating that we would have been able to detect planet c even in the absence of the K2 photometry. However, we do not see a significant peak at the frequency of planet b. Even subtracting the best-fitting Keplerian model for planet c (from the analysis described in Sec. 5.5.4), we see no signs of its small sibling (Fig. 5.1, lower plot).

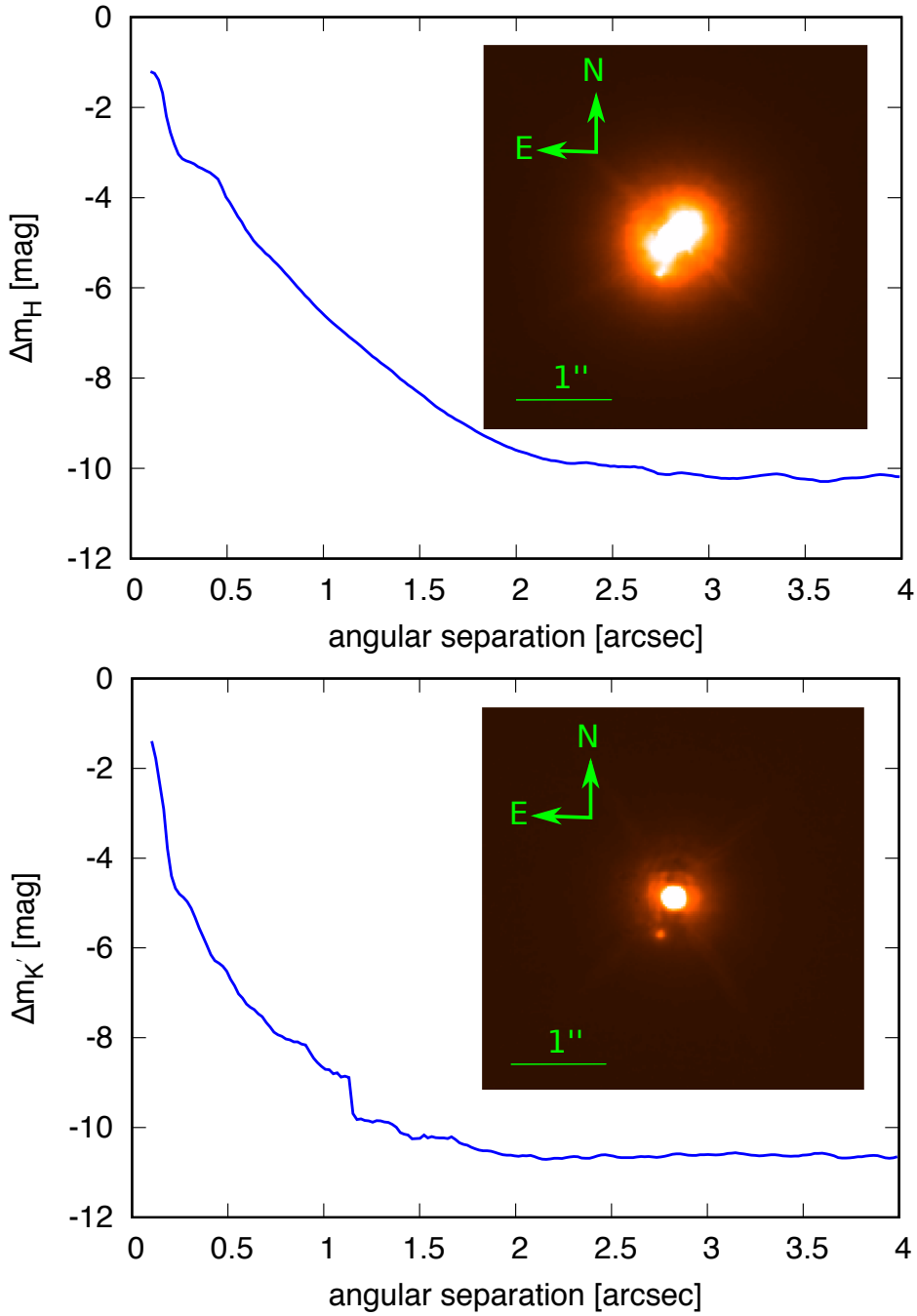

Figure 5.2: The 5-σ contrast curves and $4'' \times 4''$ Field-of-view AO images (inset) in the H band (upper plot) and K' band (lower plot) for observations done with the IRCS at the Subaru Telescope. With K2-290 in the center, the images reveal a faint neighbouring star about $0.4''$ away.

5.3.3 AO Imaging

We conducted adaptive optics (AO) imaging using IRCS (Infrared Camera and Spectrograph; Kobayashi et al., 2000; Hayano et al., 2010) on the 8.2 m Subaru Telescope at the Mauna Kea Observatory, Hawaii, US as part of the programme S18A-089. With these observations we aimed at ruling out a false positive transit signal caused by an eclipsing binary as well as to search for potential stellar companions of K2-290. We obtained H band observations on March 29 2018 and K' band observations on June 14 2018. For both observing bands we executed two sequences: one for saturated frames and the other for unsaturated, with a five-point dithering. Since the target image becomes saturated with the shortest integration (< 1 s), we used a neutral-density (ND) filter (transmittance $\sim 1\%$) for unsaturated frames. The total integration times for the saturated frames were 75 s and 37.5 s, for the H and K' bands, respectively. We used the target star itself as a natural guide star for AO. The images in both bands were reduced following the procedure described in Hirano et al. (2016). We describe our procedures for contrast analysis and aperture photometry in Sec. 5.4.2. The contrast curves and reduced AO images in both the H and K' bands are inset in Fig. 5.2. We note that the central part of the H band image is saturated and that it clearly displays a deformation. While we have not been able to pinpoint the exact cause, we assume here that it is related to the instrument or sky condition. However, the photometry uncertainty caused by this deformed PSF can be mitigated since we performed a relative photometry between the companion's Point Spread Functions (PSFs) observed in the saturated images and the parent star's PSF observed in the unsaturated images, which were obtained soon before the saturated frames.

The resulting AO images hints at the presence of a possible companion only $\sim 0.4''$ away and reveals another possible companion star at a distance of $\sim 10''$ (not displayed in the image, see Sec. 5.4.2). From now on, the potential inner companion will be referred to as star B, and the potential outer companion as star C.

5.4 Stellar characterisation

5.4.1 Host star properties

In the first step of the data analysis, we aimed to determine the absolute stellar parameters of K2-290. To this end, we created a high signal-to-noise (S/N) spectrum by co-adding the individual HARPS spectra having S/N ratios of 60 per spectral pixel at 5500 Å (see Table A3). This resulted in a co-added spectrum with a total S/N of ~ 150. We then used the iSpec framework (Blanco-Cuaresma et al., 2014) to fit synthetic stellar spectra computed using the SYNTHE (Kurucz, 1993) with MARCS model atmospheres (Gustafsson et al., 2008) to the high S/N spectrum. We assumed a Gaussian spectral PSF with a FWHM corresponding to $R = 115000$ over the spectral bandpass of the HARPS spectrograph. We

[7] https://idlastro.gsfc.nasa.gov/

Table 5.2: Identifiers, coordinates, kinematics and magnitudes of the host star K2-290. EPIC is the Ecliptic Plane Input Catalogue (`https://archive.stsci.edu/k2/epic/search.php`), while *Gaia* refer to parameters extracted from *Gaia* DR2 (Gaia Collaboration, 2018, `https://gea.esac.esa.int/archive/`). Besides the *Kepler* magnitude, the magnitudes from EPIC are collected from Høg et al. (2000) and Cutri et al. (2003). **Notes:** *As discussed in Sec. 5.5.1, the literature magnitudes reflect the *combined* magnitudes of the host star and star B. †Obtained from estimated *Sloan* r and g magitudes for star B, converted to *Kepler*-magnitude using Brown et al. (2011) (see Sec. 5.5.1). ‡Assuming the K'-band of IRCS is equal to the K-band of *2MASS*.

Parameter	Value	Source
K2	290	
EPIC	249624646	EPIC
TYC	6193-663-1	EPIC
Gaia DR2	6253844468882760832	*Gaia*
α (J2000.0)	$15^{\rm h}\ 39^{\rm m}\ 25.865^{\rm s}$	EPIC
δ (J2000.0)	$-20^\circ\ 11^{\rm m}\ 55.74^{\rm s}$	EPIC
parallax (mas)	3.636±0.050	*Gaia*
distance (pc)	275.0±3.8	*Gaia*
systemic RV (km s^{-1})	19.70±0.37	*Gaia*
μ_α (mas yr^{-1})	27.225±0.099	*Gaia*
μ_δ (mas yr^{-1})	-16.893±0.066	*Gaia*
*Combined mag.**		
G	10.8204±0.0004	*Gaia*
Kepler	10.784	EPIC
B	11.68±0.11	EPIC
V	11.11±0.11	EPIC
J	9.771±0.022	EPIC
H	9.477±0.022	EPIC
K	9.420±0.019	EPIC
g	11.179±0.030	EPIC
r	10.784±0.030	EPIC
i	10.614±0.020	EPIC
Derived host star mag.		
Kepler†	10.785	This work
H	9.494±0.022	This work
K‡	9.441±0.019	This work
Derived parameters		
$M_\star$ ($M_\odot$)	$1.194^{+0.067}_{-0.077}$	This work
$R_\star$ ($R_\odot$)	$1.511^{+0.075}_{-0.072}$	This work
$\rho_\star$ (g cm^{-3})	$0.485^{+0.074}_{-0.064}$	This work
$T_{\rm eff,\star}$ (K)	6302 ± 120	This work
$\log g_\star$ (cgs)	4.23 ± 0.10	This work
$v \sin i_\star$ (km s^{-1})	6.5 ± 1.0	This work
[Fe/H] (dex)	-0.06 ± 0.10	This work
age (Gyr)	$4.0^{+1.6}_{-0.8}$	This work

fitted the effective stellar temperature ($T_{\rm eff}$), surface gravity ($\log g$), metallicity ([Fe/H]) and projected stellar rotation speed ($v \sin i_\star$), while fixing the micro- and macroturbulence parameters ($v_{\rm mic}$ and $v_{\rm mac}$). We fixed $v_{\rm mic} = 1.3$ km s^{-1} and $v_{\rm mac} = 5.0$ km s^{-1} using the empirical relations calibrated for the *Gaia*-ESO Survey as implemented in iSpec (Blanco-Cuaresma et al., 2014). We have tested that fixing $v_{\rm mic}$ and $v_{\rm mac}$ do not significantly affect the derived spectroscopic parameters compared to keeping them free. Macroturbulence $v_{\rm mac}$ and rotational broadening $v \sin i_\star$ are degenerate at the resolution and S/N of our spectrum. The choice of $v_{\rm mac}$ therefore affects $v \sin i_\star$, but not other quantities. $v_{\rm mic}$ is similarly difficult to determine accurately from the spectrum, but only affects other quantities weakly. We have reanalysed the spectrum while keeping $v_{\rm mic}$ and $v_{\rm mac}$ free, and find parameters that agree within their uncertainties. After carrying out the fit we combined the information extracted from our spectroscopic analysis ($T_{\rm eff}$, $\log g$, and [Fe/H]) with the *Gaia* DR2 parallax (Gaia Collaboration, 2018) and apparent magnitude in the H-band (corrected for the contamination of the close companion, see Sec. 5.5.1). For the parallax error, 0.1 mas is added in quadrature to account for systematic uncertainties (Luri et al., 2018). We estimate an interstellar reddening using the dust map by Green et al. (2018). Reddening is transformed into extinction in the H-band using the relations by Casagrande and VandenBerg (2014, 2018). Using the recently updated isochrones from the BaSTI database (Hidalgo et al., 2018) and the BAyesian STellar Algorithm `BASTA` (Silva Aguirre et al., 2015) we obtain a stellar mass of $1.19^{+0.07}_{-0.08}$ $M_\odot$, a radius of $1.51^{+0.08}_{-0.07}$ $R_\odot$, and an age of $4.0^{+1.6}_{-0.8}$ Gyr. See Table 5.2 for a complete listing of the parameters. As a consistency check we use the reddening- and contamination-corrected V magnitude, the *Gaia* DR2 parallax and the spectroscopic $T_{\rm eff}$ to determine the stellar radius using the Torres (2010) bolometric correction. We derive a radius $R_\star = 1.42 \pm 0.1 R_\odot$, in agreement within 1σ of the radius derived using `BASTA`.

5.4.2 Stellar companions

In order to determine whether star B is a background star or physically associated with the planetary host star, we apply aperture photometry to the AO images. Saturation in the frames was corrected for by dividing the flux counts by the integration time for each image, in addition to taking the transmittance of the ND filter into account. However, because the potential companion is located in the halo of the host star in our observations, we have to deal with that first.

Because the asymmetric PSF could introduce systematic errors in the flux measurements if performed via radial-profile-subtraction of star A, we choose the following approach to estimate the flux ratio in the bands: The halo of the host star is suppressed by applying a high-pass filter with a width of 4 FWHM. The filter not only suppresses flux from the host star, but also reduces flux from star B. High-pass filtering introduces a flux loss of the companion, but the asymmetry in PSF has less impact on the companion's photometry since no specific shape is assumed for the targets radial profile. Following Hirano et al. (2016), the loss in flux is estimated by injecting an artificial stellar signal representing

Table 5.3: Available identifiers, coordinates, kinematics and magnitudes of the two stellar companions to K2-290, together with derived parameters from analysis of the AO images. *Gaia* refer to parameters extracted from *Gaia* DR2 (Gaia Collaboration, 2018, `https://gea.esac.esa.int/archive/`), while *2MASS* magnitudes are from Cutri et al. (2003). **Notes:** *Obtained from estimated *Sloan* r and g magitudes for star B, converted to *Kepler*-magnitude using Brown et al. (2011) (see Sec. 5.5.1). †Assuming the K'-band of IRCS is equal to the K-band of *2MASS*.

Parameter	Value	Source
Star B (Close-by component)		
AO imaging H-band		
ΔH	4.474±0.092	This work
ang. sep. (arcsec)	0.389±0.008	This work
pos. angle (degree)	160.1±1.4	This work
AO imaging K'-band		
$\Delta K'$	4.270±0.036	This work
ang. sep. (arcsec)	0.411±0.015	This work
pos. angle (degree)	159.2±2.8	This work
Derived mag.		
*Kepler**	17.981	This work
H	13.968±0.093	This work
$K^{\dagger}$	13.711±0.040	This work
Derived parameters		
$M_{\rm B}$ ($M_{\odot}$)	0.368 ± 0.021	This work
$R_{\rm B}$ ($R_{\odot}$)	0.354 ± 0.017	This work
$T_{\rm eff,B}$ (K)	3548 ± 70	This work
Star C (Far away component)		
Gaia DR2	6253844464585162880	*Gaia*
α (J2000.0)	$15^{\rm h}\ 39^{\rm m}\ 28.390^{\rm s}$	*Gaia*
δ (J2000.0)	$-20^{\circ}\ 12^{\rm m}\ 7.282^{\rm s}$	*Gaia*
parallax (mas)	4.053±0.271	*Gaia*
distance (pc)	247^{+18}_{-16}	*Gaia*
μ_{α} (mas yr^{-1})	27.224±0.099	*Gaia*
μ_{δ} (mas yr^{-1})	-16.484±0.370	*Gaia*
G	18.592 ± 0.0027	*Gaia*
J	15.400±0.060	*2MASS*
H	14.806±0.067	*2MASS*
K	14.534±0.061	*2MASS*
Derived parameters		
$M_{\rm C}$ ($M_{\odot}$)	0.253 ± 0.010	This work
$R_{\rm C}$ ($R_{\odot}$)	0.263 ± 0.010	This work
$T_{\rm eff,C}$ (K)	3397^{+77}_{-63}	This work

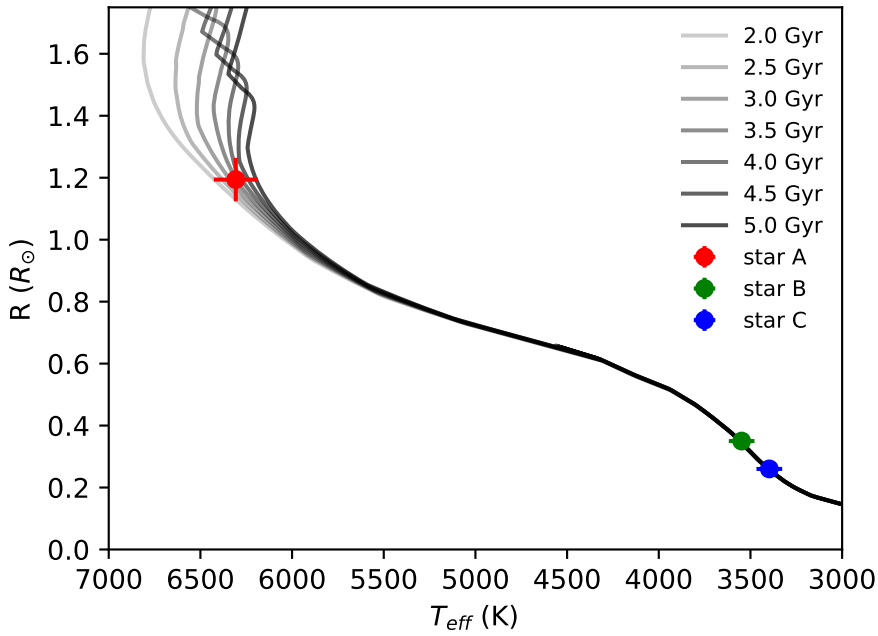

Figure 5.3: The H-R diagram for K2-290 (star A) and its two stellar companions (star B and star C) together with BaSTI isochrones ranging from 2.0 to 5.0 Gyr and with [Fe/H] = −0.1.

the possible companion into the original image, at an angular distance similar to the true signal. We found that the high-pass filter reduces the flux from the injected star by approximately 5%. Taking this into account, we derive magnitude differences for the host star and star B of $\Delta H_B = 4.474 \pm 0.092$ mag and $\Delta K'_B = 4.270 \pm 0.036$ mag.

After applying the high pass filter we employed aperture photometry and then fitted 2D Gaussians to estimate the location of the nearby companion for each band. We find angular separations of 0.389 ± 0.008 arcsec in the H-band and 0.411 ± 0.015 arcsec in the K'-band for the close-in companion.

As an additional consistency check for the photometric flux derivation we performed a photometry analysis in the K'-band on a radial-profile subtracted image. This revealed a magnitude difference of $\Delta K'_B = 4.256 \pm 0.008$ mag, consistent with the previous analysis, $\Delta K'_B = 4.270 \pm 0.036$ mag. Unfortunately due to the asymmetric PSF in the H-band, we could not perform such an analysis there. In the following we will use the latter value, such that our flux estimates for the H- and K'-bands are derived in a consistent way.

Contrast analysis and aperture photometry was not performed for the outer star

(star C), which is therefore not displayed in the inset images in fig. 5.2. This is because it is far enough away to not cause blending effects in the light curve of the host star, and because it was at the very edge of the detector in the AO images, complicating the contrast analysis. Furthermore, a sufficient number of literature values of the magnitudes is already available for a thorough stellar analysis of star C.

We derive fundamental parameters of star B and star C using `BASTA`. We assume a distance and metallicity similar to the host star. For star B, we fit the H magnitude computed using the magnitude difference ΔH from the AO analysis and the combined H magnitude of the host star and star B from 2MASS. An absolute value of the K' magnitude has not been measured for the two stars. We therefore use only the H band for extracting stellar parameters for star B[8]. For star C, we fit the 2MASS JHK magnitudes. The masses, radii and temperatures of the companions are reported in Table 5.3. We stress that the uncertainties on the derived parameters are internal to the BaSTI isochrones used. We place the three stars in an HR diagram, see Fig. 5.3. Star A is a slightly evolved F8 star while Star B and C are both M-dwarfs.

For the host star and companion C the *Gaia* DR2 catalogue provides parallaxes of 3.64 ± 0.05 mas and 4.05 ± 0.27 mas, respectively. These translate to line-of-sight distances of 275 ± 4 pc and 247^{+18}_{-15} pc, consistent with the analysis of the isochrones and our assumption of physical association. Star B is not resolved in the *Gaia* data. The angular separation of star B and C translates into separations of 113 ± 2 AU and 2467^{+177}_{-155} AU from K2-290, using the parallax of the host star. The close proximity of star B to star A makes it likely that the two stars are indeed also physically associated and that B is at the same distance from us as A and C. To quantify this statement we calculated the probability of a chance alignment for A and B making use of the `Besancon` Galactic population model[9] (Robin et al., 2003). The model is initialised at a 1 deg^2 area centered on the galactic coordinates of star A ($l = 348.0523$ deg, $b = +27.5996$ deg). We do the calculations without kinematics and use the dust map of Marshall et al. (2006) assuming no dispersion on the extinction. With these settings we calculate the number of background sources in a 10 kpc radius brighter than $H = 15$, which safely encompasses errors on the H-magnitude of star B. Doing this the model predicts 2413 background sources as bright or brighter than star B in a 1 deg^2 area surrounding star A. Scaling to an area just enclosing star A and B (i.e. with a radius of ~ 0.4 arcsec), the probability of chance alignment is $< 0.01\%$. Given this value we assume in the following that star B is physically associated with star A, and acknowledge that this association is based on a probability statement. This seems to also be the case for companion C, since it shares the same proper motion as the host star (see Tables 5.2 and 5.3). In conclusion, K2-290 is most likely a member of a triple star system.

[8] Even though the K' band of IRCS (1.95–2.30 μm) is similar to the K band of 2MASS (1.95–2.36 μm), we wanted to keep the analysis to bands in which we could strictly compare. However, assuming $K' = K$ and repeating the analysis gave the same results.

[9] `http://modele2016.obs-besancon.fr`

5.5 Planetary analysis

In this section we test whether the photometric transits are a result of a false positive scenario, in particular component B being an eclipsing binary. We then describe the transit model as well as our RV model, and how we jointly fit these to extract system parameters from the data.

5.5.1 *False positive analysis*

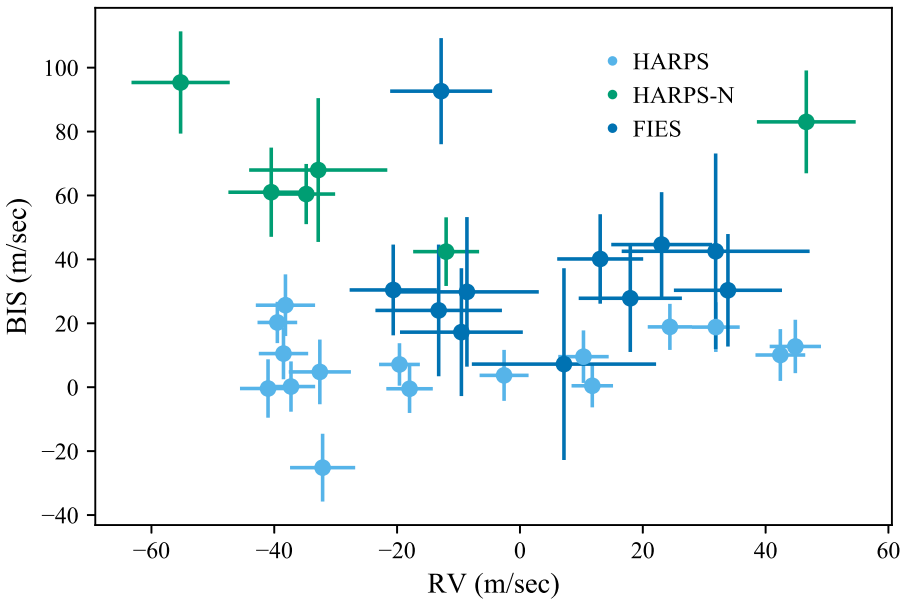

Figure 5.4: Correlation between the CCF bisector inverse slopes and the radial velocities from the HARPS, HARPS-N and FIES spectrographs. The offsets for each spectrographs has been subtracted, with the best-fitting values found during the global modelling of the photometry and spectroscopy as described in Sec. 5.5.4.

We test the scenarios in which the apparent transits do not originate from a planet occulting the host star, but instead from component B being a system of eclipsing binaries or being the host star of both planets. We do this because star B is not spatially resolved in the *K2* photometric lightcurve, due to its close proximity to the host star and pixel sizes of the spacecraft. The amount of flux received therefore also needs to be corrected, in order for the normalized transit to not appear too shallow. This is done by comparing the H[10] magnitude for the companion to BaSTI isochrones, assuming the reddening, metallicity and age is the same as for the planetary host star. From this we can obtain *Sloan* r and g magnitudes of star B, which can be converted to a Kepler magnitude using

[10] As mentioned previously, an absolute value of the K' magnitude has not been measured for the host star. We therefore use only the H band for comparison between the two stars.

the relation presented in Brown et al. (2011). This analysis reveals that the close-by companion is ~ 7.2 mag fainter in the Kepler band-pass, corresponding to a flux contribution of $\sim 0.1 - 0.2\%$ in the light curve. This indicates that the large planet must be orbiting the bright star, since star B is too faint and its light is too red to account for transits of the observed depths in the Kepler-band: Assuming the companion is totally eclipsed the blended transit depth will only be the afforementioned $\sim 0.1 - 0.2\%$. This is too shallow to produce the deepest transits, which have depths of 0.5%. If the smallest transit signals is due to the companion being an eclipsing binary diluting the signal, the transit depth of 0.03% would mean that $\sim 15 - 30\%$ of the companion should be covered during transit. This would lead to a V-shaped transit, which is inconsistent with what we observe (see upper plot of Fig. 5.6). Therefore, both planets are highly unlikely to be false positives. In the system analysis, the blending of the close companion is taken into account by subtracting its flux contribution from the photometric light curve.

Another analysis can be done by examining the asymmetry of the line profile, via investigating whether there is a correlation between the CCF bisector inverse slopes (BISs) and the RVs (e.g. Queloz et al., 2001). Fig. 5.4 displays the BIS as a function of the RV data, showing no signs of correlation – particularly if each instrument is considered separately. This suggests that the Doppler shifts of K2-290 are due to the orbital motion of the large planet, and not an astrophysical false positive.

A third false positive check can be performed by comparing stellar parameters from the analysis of the host star described in Sec. 5.4 with transit observables extracted as described in the following sections. Assuming circular orbits, we calculate stellar densities $\rho_{\star,\mathrm{circ}}$ of 0.51 ± 0.20 g cm^{-3} and 0.55 ± 0.07 g cm^{-3} using the best-fitting parameters for planet b and c from an analysis without a prior on the stellar spectrocopic density $\rho_\star$. With the exclusion of this prior, we assume that the best-fitting parameters of the transits are not strongly linked to the extracted stellar parameters. These densities agrees with the value from the stellar analysis of the host star $\rho_\star = 0.485 \pm 0.07$ g cm^{-3}. Using the values of R_B, R_C, M_B and M_C from the companion analysis in Sec. 5.4.2 we retrieve mean densities of the stars of $\rho_B = 12.2 \pm 2.2$ g cm^{-3} and $\rho_C = 20.1 \pm 2.4$ g cm^{-3}. These do not agree with the values obtained from the transit parameters, and are therefore inconsistent with the planets orbiting either of the two M dwarf companions, further verifying that both planets orbit star A.

5.5.2 Transit model

From the photometric data, each transit is isolated in a window spanning 15 hr on either side of the mid-transit time. The photometric uncertainty σ_P is estimated as the standard deviation of the normalized out-of-transit data in these windows. The transits are normalized individually by including a quadratic polynomial fit of the data to the transit model during the parameter evaluation described in Sec. 5.5.4. The transit lightcurve with a quadratic limb-darkening profile

is modeled using `batman` (Kreidberg, 2015), a Python package which calculates the lightcurve analytically based on the formalism of Mandel and Agol (2002). When modelling the light curve, the *Kepler* 29.4 min integration time is mimicked by integrating over 10 models which had been evaluated in a time interval of 29.4 min. The free parameters for each transiting planet are the orbital period P_k, the mid-transit time T_{0k}, the scaled planetary radius $R_{\mathrm{p}k}/R_\star$, the scaled orbital distance $a_k/R_\star$, and its orbital inclination i_k. The index k runs over planet b and c. For planet c, which influence we could identify in the RV data (see Sec. 5.3.2), we both investigate a circular and eccentric solution (see Sec. 5.5.5). In the latter, the orbital eccentricity e and the argument of periastron ω are treated as free parameters. For efficiency we step in $\sqrt{e}\cos\omega$ and $\sqrt{e}\sin\omega$ (Ford, 2006; Anderson et al., 2011). We find that we cannot sufficiently constrain the eccentricity of planet b, and we therefore assume the orbit of the small planet to be circular. This is consistent with Van Eylen and Albrecht (2015) and Van Eylen et al. (2019), which show that near-zero eccentricity is likely for a small planet in a system with multiple transiting planets, and that the eccentricity distribution of such planets can be described by the positive half of a Gaussian distribution, which peaks at zero eccentricity and has a width of $\sigma = 0.083^{+0.015}_{-0.020}$. Stellar limb darkening is modeled assuming a quadratic limb-darkening law with parameters c_1 and c_2. Finally we introduce an additional term σ_{K2} in an attempt to capture any unacccounted photometric noise (e.g. caused by planetary spot crossing), similar to the jitter term often used in the RV work. This is added in quadrature to the photometric errors. With the 735 photometric measurements considered here, the log-likelihood for the photometry alone then becomes:

$$\ln \mathcal{L}_P = -\frac{1}{2}\sum_{i=1}^{735}\left(\ln\left(2\pi\left[\sigma_i^2+\sigma_{\mathrm{K2}}^2\right]\right)+\frac{\left[P_i(O)-P_i(C)\right]^2}{\left[\sigma_P^2+\sigma_{\mathrm{K2}}^2\right]}\right) \tag{5.1}$$

where $P_i(O)$ and $P_i(C)$ are the observed and calculated values of the i'th photometric data point, $\sigma_P = 0.000056$ is the internal measurement uncertainty estimated from the out-of-transit lightcurve and σ_{K2} contains any additional photometric noise.

5.5.3 Radial velocity model

The radial velocity shifts of the host star due to the gravitational pull of the planets is modeled with a simple Keplerian model. Because we found no signs of planet b in the RV data (see Sec. 5.3.2), our RV model only includes planet c. The additonal parameters needed are the RV semi-amplitude K and RV offsets γ as well as jitter terms σ_{jit} for each spectrograph. The latter accounts for any stellar or instrumental noise not captured in the internal uncertainties and is

added in quadrature. The log-likelihood for the 33 RV data points is:

$$\ln \mathcal{L}_{RV} = -\frac{1}{2}\sum_{j=1}^{33}\left(\ln\left(2\pi\left[\sigma_j^2+\sigma_{\rm jit}^2\right]\right)+\frac{\left[RV_j(O)-RV_j(C)-\gamma\right]^2}{\left[\sigma_j^2+\sigma_{\rm jit}^2\right]}\right) \tag{5.2}$$

where j indexes the 33 observations. $RV_j(O)$ and $RV_j(C)$ are the observed and calculated values of the j'th RV data point at time t_j, with the corresponding internal measurement uncertainty σ_j, while γ and $\sigma_{\rm jit}$ are the RV offset and jitter parameters, which differ for each spectrograph.

5.5.4 Comparing models and data

To determine the parameters and their posterior distribution, we model the photometric and RV data together, fitting them jointly. In summary, the fitting parameters of the joint analysis are for each planet the orbital period P, the mid-transit time T_0, the scaled planetary radius $R_{\rm p}/R_\star$, the scaled orbital distance $a/R_\star$, and its orbital inclination i. For planet c, we also fit for the RV semi-amplitude K and in addition we experiment with both a circular solution, as well as an eccentric analysis via the parametrization $\sqrt{e}\cos\omega$ and $\sqrt{e}\sin\omega$. The fitting parameters connected to the star are the quadratic limb-darkening parameters c_1 and c_2. The fitting parameters for the instruments are the noise/jitter terms σ and systemic RV velocities γ.

For the limb-darkening coefficients we impose a Gaussian prior using the values $c_1 = 0.31$ and $c_2 = 0.30$ from an interpolation of the Kepler-band tables in Claret and Bloemen (2011) obtained via Eastman et al. (2013)[11], and with an uncertainty width of 0.1. From the spectroscopic analysis we obtained a mean stellar density of the star $\rho_\star = 0.485 \pm 0.07\,\mathrm{g\,cm^{-3}}$. With a well-determined orbital period, we can use this information as an additional prior in our analysis, as photometric data also constrains the stellar density for particular orbital shapes and orientations (see Van Eylen and Albrecht, 2015, and references therein). Therefore, we use this prior information and the transit photometry to support the e and ω measurements from the RV data when exploring the eccentric model. The rest of the parameters are uniformly sampled. The priors on $\rho_\star$, c_1 and c_2 have a log-likelihood $\ln\mathcal{L}_{\rm prior}$. The total log-likelihood is the sum of eq. 5.1, 5.2 and $\ln\mathcal{L}_{\rm prior}$:

$$\ln\mathcal{L} = \ln\mathcal{L}_P + \ln\mathcal{L}_{RV} + \ln\mathcal{L}_{\rm prior}. \tag{5.3}$$

The posterior distribution of the fitting parameters are sampled using the MCMC Python package `emcee` (Foreman-Mackey et al., 2013). We initalize 220 walkers near the maximum likelihood result, advancing them for 10000 steps and abandoning the 5000 first steps as the burnt-in sample, at which point the walkers have converged.

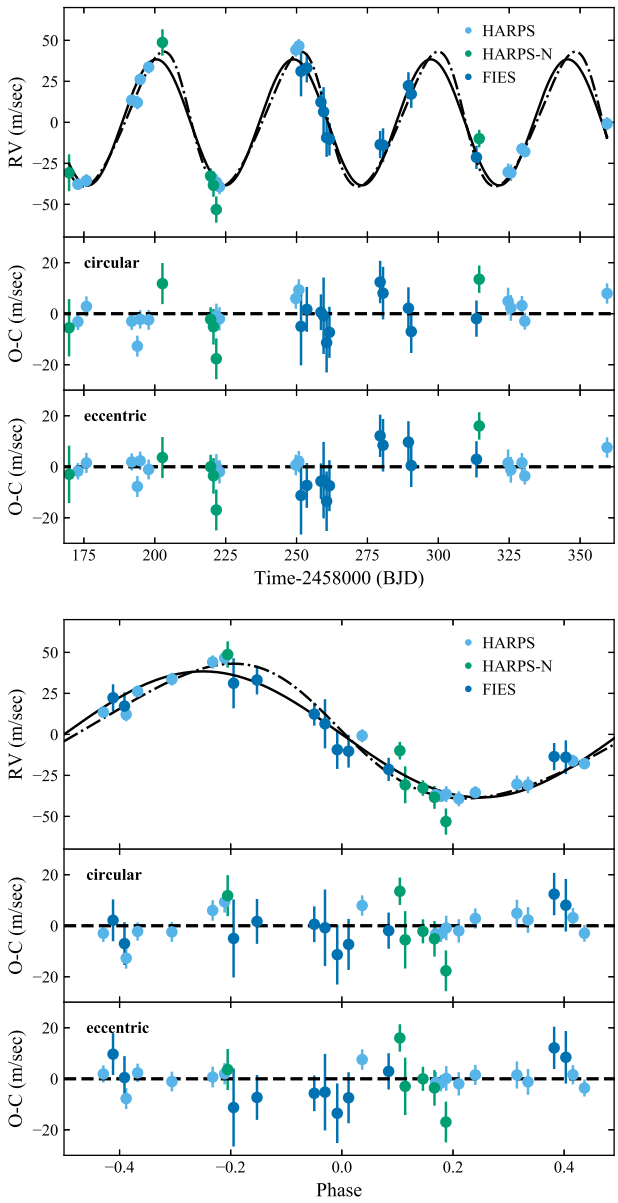

Figure 5.5: RV measurements of K2-290c from the HARPS, HARPS-N and FIES spectrographs, together with the best-fitting circular model from the joint analysis of the photometry and spectroscopy (solid line) and the corresponding model for an eccentric orbit (dash-dotted line). Upper: The RVs as a function of time. Lower: The phasefolded RV. The bottom panels in both plots show the residuals between the observations and best-fitting model for the circular and eccentric case. The eccentricity from the eccentric analysis is most likely overestimated and we therefore consider the circular model to be a better description of the data (see Sec. 5.5.5). The values of the corresponding parameters are displayed in Table 5.4 (Table 5.5 for the eccentric case), and the data points are presented in Table A3.

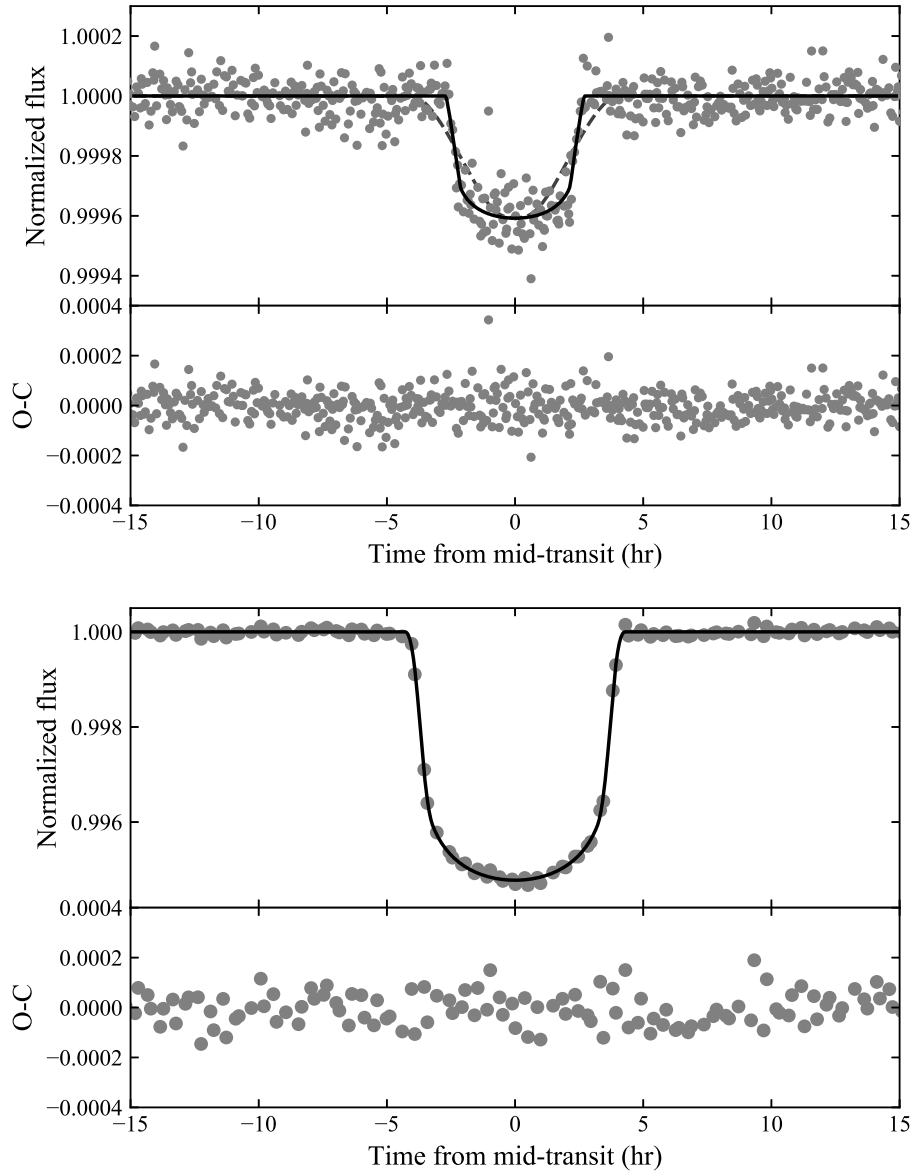

Figure 5.6: Phasefolded transit light curves of K2-290b (upper) and K2-290c (lower) observed with K2, together with the best-fitting model from the joint analysis of the photometry and spectroscopy (solid line). The bottom plot shows the residuals. The values of the corresponding best-fit parameters are displayed in Table 5.4. The dashed line on the upper plot indicates the modelled light curve in the case of the shallow transit signal being a false positive caused by star B. In order to reproduce the observed depth in the combined light of star A and B, this would require star B to be an eclipsing binary diluting star A with a transit depth of 15% – 30%. This would lead to a very V-shaped transit, which is not what we observe. For the deep transit (lower plot), even a total eclipse of star B is not sufficient to reproduce the signal.

Table 5.4: System parameters for K2-290. **Notes:** *We both investigate a circular and eccentric solution. From the eccentric analysis we obtain $e = 0.144^{+0.033}_{-0.032}$ and $\omega = 70.0 \pm 9.0$ deg. With ω close to 90 deg the eccentricity from the eccentric analysis is most likely overestimated and we suspect that the circular model is a better description of the data (see Sec. 5.5.5). Here we therefore only report the parameter values from the circular analysis, together with the one-sided 3σ upper limit on e from the eccentric analysis. The complete set of parameter values of the eccentric solution is given in Table 5.5. †Upper limit (3σ) value obtained by including planet b in the RV analysis and allowing e and ω for both planets to vary as well. The 1σ results are given in the text in Sec. 5.5.5. ‡The values of the equlibrium temperatures assume a Bond albedo of 0 and no recirculation of heat. The errors only represent propagated internal errors.

Host star parameters (fixed)		
Stellar mass $M_\star$ ($M_\odot$)	$1.194^{+0.067}_{-0.077}$	
Stellar radius $R_\star$ ($R_\odot$)	$1.511^{+0.075}_{-0.072}$	
Stellar density $\rho_\star$ (g cm^{-3})	$0.485^{+0.074}_{-0.064}$	
Effective temperature $T_{\rm eff,\star}$ (K)	6302 ± 120	
Surface gravity $\log g_\star$ (cgs)	4.23 ± 0.10	
Projected rotation speed $v \sin i_\star$ (km s^{-1})	6.5 ± 1.0	
Metallicity (Fe/H)	-0.06 ± 0.10	
Age (Gyr)	$4.0^{+1.6}_{-0.8}$	
Parameters from RV and transit MCMC analysis	**Planet b**	**Planet c (circular)***
Quadratic limb darkening parameter c_1	0.330 ± 0.044	
Quadratic limb darkening parameter c_2	0.219 ± 0.067	
Noise term K2 $\sigma_{\rm K2}$	$0.0000209^{+0.0000044}_{-0.0000052}$	
Jitter term FIES $\sigma_{\rm jit,FIES}$ (m s^{-1})	$3.1^{+3.5}_{-2.2}$	
Jitter term HARPS $\sigma_{\rm jit,HARPS}$ (m s^{-1})	$4.0^{+1.8}_{-1.7}$	
Jitter term HARPS-N $\sigma_{\rm jit,HARPS\text{-}N}$ (m s^{-1})	$11.6^{+5.3}_{-8.6}$	
Systemic velocity FIES $\gamma_{\rm FIES}$ (km s^{-1})	$19.6323^{+0.0031}_{-0.0030}$	
Systemic velocity HARPS $\gamma_{\rm HARPS}$ (km s^{-1})	19.7594 ± 0.0014	
Systemic velocity HARPS-N $\gamma_{\rm HARPS\text{-}N}$ (km s^{-1})	$19.7590^{+0.0056}_{-0.0062}$	
Orbital period P (days)	$9.21165^{+0.00033}_{-0.00034}$	$48.36685^{+0.00041}_{-0.00040}$
Time of midttransit T_0 (BJD)	$2457994.7725^{+0.0016}_{-0.0015}$	$2458019.17333 \pm 0.00029$
Scaled planetary radius $R_{\rm p}/R_\star$	0.01900 ± 0.00028	$0.06848^{+0.00042}_{-0.00047}$
Scaled orbital distance $a/R_\star$	$13.15^{+0.69}_{-0.66}$	43.5 ± 1.2
Orbital inclination i (deg)	$88.14^{+0.62}_{-0.50}$	$89.37^{+0.08}_{-0.07}$
RV semi-amplitude $K_\star$ (m s^{-1})	$< 6.6^\dagger$	38.4 ± 1.7
Derived parameters		
Orbital eccentricity e	0 (adopted)	0 (adopted, <0.241)
Argument of periastron ω (deg)	90 (adopted)	90 (adopted)
Impact parameter b	0.438 ± 0.023	0.474 ± 0.012
Total transit duration T_{14} (hr)	4.96 ± 0.31	8.14 ± 0.26
Full transit duration T_{23} (hr)	4.73 ± 0.40	6.82 ± 0.24
Planetary mass $M_{\rm p}$	$< 21.1\ M_\oplus{}^\dagger$	$0.774 \pm 0.047\ M_{\rm J}$
Planetary radius $R_{\rm p}$	$3.06 \pm 0.16 R_\oplus$	$1.006 \pm 0.050 R_{\rm J}$
Planetary mean density $\rho_{\rm p}$ (g cm^{-3})	$< 4.1^\dagger$	1.01 ± 0.16
semi-major axis a (AU)	0.0923 ± 0.0066	0.305 ± 0.017
Equlibrium temperature $T_{\rm eq}$ (K)	$1230 \pm 38^\ddagger$	$676 \pm 16^\ddagger$

5.5.5 Planet parameters

The parameter values corresponding to the median of the MCMC posterior distributions are reported in Table 5.4 together with their 1σ uncertainties. The RVs and phasefolded RVs for planet c is shown in Fig. 5.5, while the phasefolded lightcurves for planet b and c are displayed in Fig. 5.6.

To account for any long-term trend from a possible long-period unseen companion, we could also allow for a linear drift of the RV signal, $\dot{\gamma}$. Including this in the analysis, and selecting BJD 2458169.785818 – the time of the first RV observation – as our zeropoint in defining $\dot{\gamma}$, we find a linear drift of 0.02 ± 0.02 m s^{-1} d^{-1}. This shows that any possible RV trend is insignificant within 1σ. To further check whether we are justified in excluding a possible RV drift in our analysis, we compute the Bayesian Information Criterion (BIC). This is done for both an analysis including and excluding $\dot{\gamma}$. With 768 total RV and photometry measurements (as well as 3 priors), and 22 (23) model parameters excluding (including) the linear drift, we obtain a difference in BIC of 8. It favours the model *excluding* $\dot{\gamma}$, but we note that there are no significant differences in parameter values between the two models. The parameters values reported in Table 5.4 are for an analysis excluding the drift.

Because of the non-detection of K2-290b in the RV data (see Sec. 5.3.2 and Fig. 5.1), it was not possible to confidently determine the mass of the planet. However, using the mass-radius relationship from Weiss and Marcy (2014), the mass is estimated to be $\sim 7.6 M_\oplus$. This is consistent with the smaller, close-in planet being a mini-Neptune. The mass translates into an RV semi-amplitude of ∼2-3 m s^{-1}. Indeed, such signal would be hidden in the RVs, given the noise level of the data. Doing an analysis which includes planet b in the RV fit and allows for varying e and ω for the small planet, would indicate an RV semi-amplitude $K = 1.6^{+1.7}_{-1.1}$ m s^{-1}, an eccentricity $e = 0.119^{+0.201}_{-0.083}$ and a mass of $M_p = 5.8 \pm 5.1 M_\oplus$. Using the 3σ result of this analysis, we obtain upper limits of $K < 6.6$ m s^{-1} and $M_p < 21.1 M_\oplus$. We note that the phase coverage of the RVs of planet b is not ideal, with a large gap at phases ∼0.1-0.3. However, repeating the frequency analysis of Sec. 5.3.2 but including noise-adjusted simulated data in this region with injected K-amplitudes up to 6.6 m s^{-1}, still does not reveal signals above the 0.1% FAP at the frequency of planet b (see Figure 5.7).

For K2-290c we find a mass of $0.774 \pm 0.047 M_J$ and a radius of $1.006 \pm 0.050 R_J$. Together with its period of $48.36685^{+0.00041}_{-0.00040}$ days, this makes the planet a warm Jupiter.

For the eccentric solution of planet c, the posteriors of the eccentricity e and argument of periastron ω is displayed in Fig. 5.8 (black), and indicates that the planetary orbit is mildly eccentric with $e = 0.144^{+0.033}_{-0.032}$ and $\omega = 70.0 \pm 9.0$ deg. If we were not careful when removing the blended light from star B, the eccentricity value could be biased. But, using no prior on the stellar density $\rho_\star$ – and thereby

[11] http://astroutils.astronomy.ohio-state.edu/exofast/limbdark.shtml

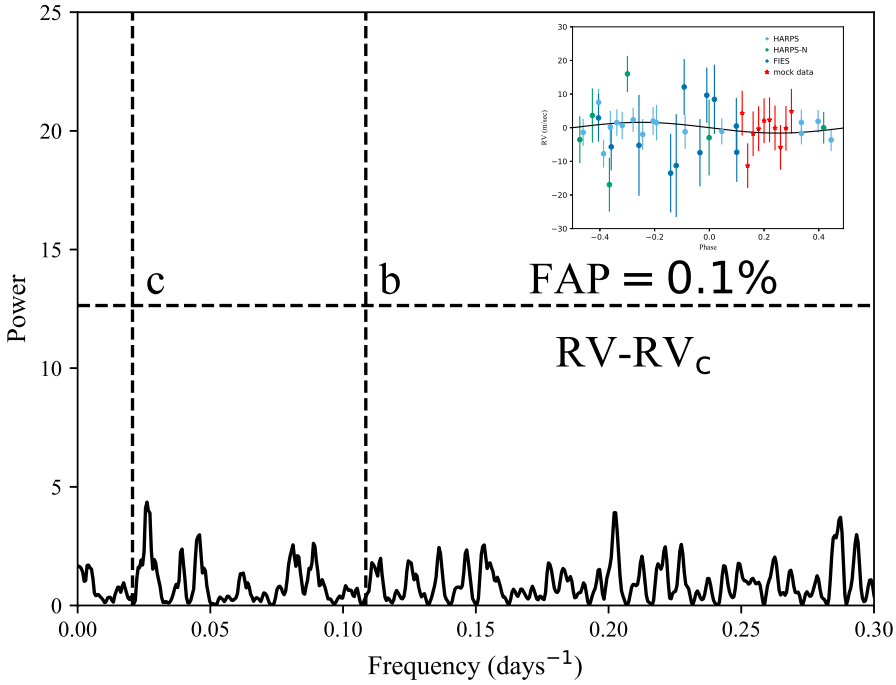

Figure 5.7: Same as the right part of figure 5.1, but where the frequency analysis includes simulated data in planet b's spotty phase region of 0.1-0.3. The mock data were created by adding Gaussian noise equal to the mean noise value of the real data, 6.7 m s^{-1}, to a Keplerian model. The simulated data in this specific LS periodogram is done with $K = 1.6$ m s^{-1}, and can be seen as the inset in the right corner (with this specific Keplerian model shown as a black line). The analysis was repeatedly performed for values of K up to the upper limit of 6.6 m s^{-1}. In neither of these, the planet was detected above the FAP threshold of 0.1%.

essentially *only* obtaining information on the eccentricity from the RV data alone – recovers an eccentricity $e = 0.130^{+0.037}_{-0.028}$, consistent with the previous analysis.

Doing the analysis for a circular orbit, and calculating the BIC of both the eccentric and circular fits, we can test whether we are justified in including e and ω as two additional degrees of freedom. We obtain a difference in BIC of 16 in favour of the eccentric solution, suggesting that the eccentricity of planet c is well determined.

However, we note that $\omega = 70.0 \pm 9.0$ deg is close to 90 deg. This warrants some further scrutiny as the RV method is better at constraining $\sqrt{e}\cos(\omega)$ than $\sqrt{e}\sin(\omega)$. Therefore larger confidence intervals for the eccentricity are allowed for orbital orientations near -90 deg or $+90$ deg than near 0 deg or ± 180 deg. Combined with an uneven phase coverage and the use of different

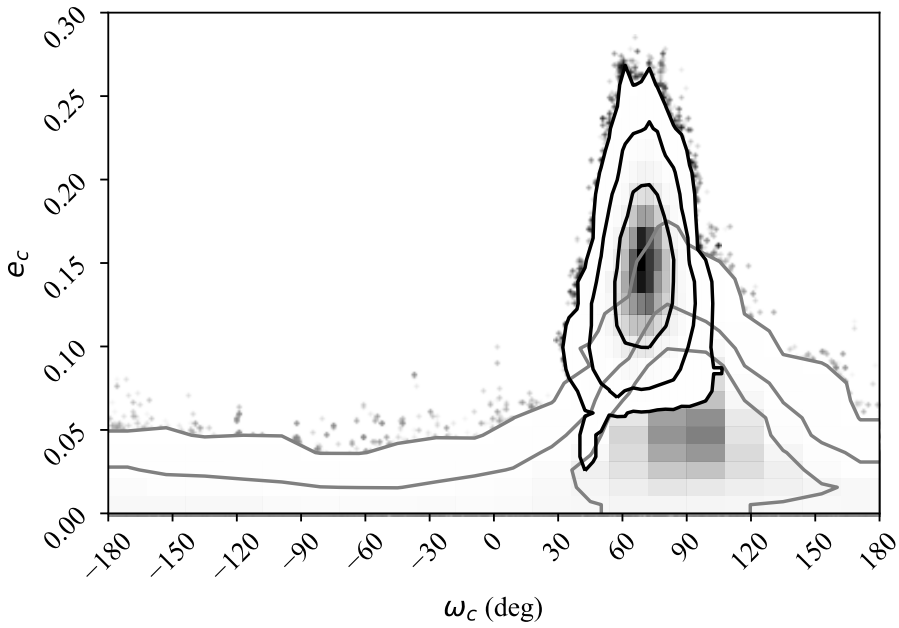

Figure 5.8: The 2D 68%, 95% and 99.7% posterior distribution from the eccentric analysis described in Sec. 5.5.4 (black) and from an analysis of RVs from a simulated circular orbit with added Gaussian noise corresponding to the real RV errors (grey). The analysis on the mock circular data allows for moderate eccentricities – with its confidence limits overlapping near $\omega = 90$ deg – suggesting that with the data at hand we are not able to confirm a non circular orbit.

instruments this could lead to an erroneous detection of a seemingly significant eccentricity (e.g. Laughlin et al., 2005; Albrecht et al., 2012), similar to the bias in low S/N cases towards the antisymmetric Rossiter-McLaughlin signal discussed in Chapter 3. We investigated this here by creating a mock data set, where we used the parameters of the circular solution from Table 5.4. With this circular model we now created for each of the original RV time stamp an RV "data point" adding random Gaussian noise corresponding to the RV uncertainties of the original data. Finally we run our analysis on this simulated data set just as we did for the real measurements. We repeated this experiment several times, using different seeds for the Gaussian noise. A typical example of the posterior of e and ω for the simulated circular data is shown in Fig. 5.8 (grey), together with the posterior from the eccentric analysis on the real data (black). We find that the uncertainty intervals for e are largest around $\omega = +90$ deg, and indeed the 2D confidence intervals between the mock and real data do overlap. This suggests that the eccentricity we find from the eccentric analysis of the real data is suspicious and should serve as an upper bound on the eccentricity only. We therefore adopt the circular solution, which parameters are reported in Table 5.4, and note that from the eccentric analysis the one-sided 3σ upper limit on

the eccentricity is $e < 0.241$. Nonetheless, varying e and ω only reveals minor changes in the rest of the system parameters, with almost all being within 1σ of the circular values (see Table 5.5).

Table 5.5: Same as Table 5.4, but with the eccentric solution of planet c's orbit. **Notes:** *Because of $\omega = 70.0 \pm 9.0$ deg being close to 90 deg, we regard this solution as highly suspicious (se Sec. 5.5.5).

Parameters from RV and transit MCMC analysis	Planet c (eccentric)*
Quadratic limb darkening parameter c_1	0.329 ± 0.037
Quadratic limb darkening parameter c_2	0.219 ± 0.067
Noise term K2 $\sigma_{\rm K2}$	$0.0000209^{+0.0000044}_{-0.0000052}$
Jitter term FIES $\sigma_{\rm jit,FIES}$ (m s^{-1})	$4.1^{+4.4}_{-2.8}$
Jitter term HARPS $\sigma_{\rm jit,HARPS}$ (m s^{-1})	$1.5^{+1.6}_{-1.0}$
Jitter term HARPS-N $\sigma_{\rm jit,HARPS\text{-}N}$ (m s^{-1})	$11.1^{+7.2}_{-4.8}$
Systemic velocity FIES $\gamma_{\rm FIES}$ (km s^{-1})	$19.6316^{+0.0032}_{-0.0033}$
Systemic velocity HARPS $\gamma_{\rm HARPS}$ (km s^{-1})	19.7612 ± 0.0013
Systemic velocity HARPS-N $\gamma_{\rm HARPS\text{-}N}$ (km s^{-1})	$19.7611^{+0.0057}_{-0.0059}$
Orbital period P (days)	$48.36692^{+0.00040}_{-0.00042}$
Time of midttransit T_0 (BJD)	$2458019.17336 \pm 0.00029$
Scaled planetary radius $R_{\rm p}/R_\star$	0.06758 ± 0.00057
Scaled orbital distance $a/R_\star$	40.1 ± 1.5
Orbital inclination i (deg)	$89.41^{+0.17}_{-0.14}$
RV semi-amplitude $K_\star$ (m s^{-1})	41.1 ± 1.7
$\sqrt{e}\sin(\omega)$	$0.354^{+0.043}_{-0.050}$
$\sqrt{e}\cos(\omega)$	$0.130^{+0.052}_{-0.059}$
Derived parameters	
Orbital eccentricity e	$0.144^{+0.033}_{-0.032}$
Argument of periastron ω (deg)	70.0 ± 9.0
Impact parameter b	0.358 ± 0.018
Total transit duration T_{14} (hr)	8.09 ± 0.47
Full transit duration T_{23} (hr)	6.92 ± 0.46
Planetary mass $M_{\rm p}$ ($M_{\rm J}$)	0.819 ± 0.048
Planetary radius $R_{\rm p}$ ($R_{\rm J}$)	0.993 ± 0.050
Planetary mean density $\rho_{\rm p}$ (g cm^{-3})	1.11 ± 0.18
semi-major axis a (AU)	0.281 ± 0.017
Equlibrium temperature $T_{\rm eq}$ (K)	704 ± 19

5.6 Discussion

5.6.1 *Properties and composition of the planets*

Planet b is exposed to intense radiation from the host star. With a distance to the star of 0.0923 ± 0.0066 AU or $13.15^{+0.69}_{-0.66} R_\star$, it receives an incident flux of $\sim 400 F_\oplus$. This puts it outside of the super-Earth desert (Lundkvist et al.,

2016). It also resides above the radius valley (Fulton et al., 2017; Van Eylen et al., 2018), suggesting that the planet is not undergoing photo-evaporation of its outer envelope.

Given the relatively low incident flux of planet c of $\sim 0.6 \cdot 10^8$ erg s^{-1} cm^{-2}, the planet lies below the threshold of $2 \cdot 10^8$ erg s^{-1} cm^{-2}, where irradiation might inflate it (Demory and Seager, 2011). The planetary radius may therefore be directly compared to the models presented by Fortney et al. (2007), revealing a mass of the planetary core of about $\sim 25 - 50 M_\oplus$[12]. However, in these models all solids are assumed to be located in the core. The models of Thorngren et al. (2016) allow for metal enrichment and for solid materials to be located in the planet's gaseous envelope. Using these semi-empirical models, we retrieve a planetary bulk metallicity $Z = 0.133 \pm 0.036$ and a heavy elements mass of $49.5 \pm 6.4 M_\oplus$, with $10 M_\oplus$ distributed inside the core and the remaining mixed in the envelope.

5.6.2 Formation

We find that the orbit of the warm Jupiter K2-290c has an eccentricity $e < 0.241$, and the existing RV data are compatible with a circular orbit. This is consistent with the picture presented in Dawson and Murray-Clay (2013), where warm Jupiters with low eccentricities orbit metal-poor stars ([Fe/H] $= -0.06 \pm 0.1$). The orbital eccentricity is too small for the planet to be a proto hot Jupiter undergoing migration through tidal friction (Dawson and Johnson, 2018, Fig. 4). This does not rule out high-eccentricity migration through secular gravitational interactions, causing the planetary eccentricity to undergo oscillations excited by a nearby mutually inclined third body (Petrovich and Tremaine, 2016). For this to happen, a solar-mass perturber needs to be within a distance of ~ 30 AU, and a Jupiter-mass perturber within ~ 3 AU (Dong et al., 2014), for a warm Jupiter 0.2 AU away. With a projected distance of 113 ± 2 AU even star B – the closest companion – is too far away. Neither from the AO images nor the transit light curve do we find evidence for an additional close-by companion. Furthermore, it seems unlikely that the warm Jupiter and mini-Neptune would remain coplanar following these orbital perturbations, which is likely to produce higher mutual inclinations (Pu and Lai, 2018). However seeing both planets in transit do not necessarily guarantee coplanar orbits, as we might have observed them along the line of nodes. It should also be noted, that even though the distances between the host star and its two stellar companions are in agreement with the outcome of simulated high-eccentricity migration of Jupiters in triple star systems in Hamers (2017), these simulations fail to produce warm Jupiters in any significant number.

With an eccentricity < 0.4 and with the presence of its mini-Neptune sibling, K2-290c fits the picture presented in Huang et al. (2016): low eccentricity warm Jupiter systems have inner low-mass companions with low mutual inclinations. They argue that this suggests that warm Jupiter might originate from two different formation mechanisms: 1) high-eccentricity systems ($e > 0.4$) are formed

[12] From the extended webtable of Fortney et al. (2007).

through high-eccentricity migration and 2) low-eccentricity systems form *in situ*, since disk migration would clear out any companions in the warm Jupiter neighbourhood. The latter is consistent with the core mass of $\sim 10 - 50 M_{\oplus}$, which is sufficient for the run-away accretion phase of *in situ* gas giant formation at distances of 0.1-1.0 AU from the host star (Rafikov, 2006). However, as noted in Dawson and Johnson (2018), disk migration should not be ruled out as the origin channel of the warm Jupiter in these kind of systems, as the migration of the giant planet might have occured before the *in situ* creation of its small sibling. This suggests that K2-290c originate from either *in situ* formation or disk migration.

A way to further test the origin of K2-290c would be to measure the system's spin-orbit angle, which is the subject of the next chapter. K2-290 is an excellent target for measuring the spin-orbit angle through observations of the Rossiter-McLaughlin effect: From Eq. 3.9 and the values of $v \sin i_{\star} \sim 6.5 \pm 1.0$ km s^{-1} and $R_p/R_{\star} \sim 0.07$, we expect an amplitude of the Rossiter-McLaughlin signal of about $\sim$19 m s^{-1}, taking limb darkening and the eccentricity into account. The host star is relatively bright ($V = 11.11$), allowing for a high S/N ratio and small RV errors, which makes the effect easily detectable with high resolution fiber-fed stabilised spectrographs. In addition, with an impact parameter of ~ 0.5, there should be no degeneracy between the spin-orbit angle and $v \sin i_{\star}$.

6

A multi transiting planet system with retrograde co-planar orbits and primordial misalignment.

Throughout my PhD studies, I continually hoped to expand the small obliquity sample of multi-planet and warm Jupiter systems which have measured spin-orbit angles. This was done by closely examining candidates applicable to Rossiter-McLaughlin measurements and with the right transit timing, in an attempt to obtain the spin-orbit angle through their spectroscopic transit. Of the few suitable targets, I managed to get observing time for a couple. However, a combination of bad weather, technical problems and pure bad luck, meant that with half a year left of the PhD, I still had not made any progress. This all changed with the detection of K2-290 presented in the previous chapter. Here we had discovered a system which not only had multiple planets of which one was a warm Jupiter; it also had the perfect velocity anomaly amplitude and transit timing in regards to conducting the observations before the end of my PhD. Armed with this, I applied for observing time for the second and first half of the transit of the warm Jupiter, to be carried out in April 2019 at TNG and in June 2019 at HDS. Though there were problems during the April observations with a temporary gravity wave interruption, the night in June went smoothly and resulted in very precise Rossiter-McLaughlin data. These measurements were so promising, that a subsequent Director Discretion Time proposal for ESPRESSO was also successful, granting meter-precision Rossiter-McLaughlin data of the mini-Neptune. These datasets clearly established the system to be retrograde, and subsequent analyses found the misalignment to stem from a primordial tilt of the protoplanetary disk. Me and my collaborators had for the first time obtained Rossiter-McLaughlin measurements of two planets in the same system, as well as found the first retrograde multi-planet system and at the same time discovered the first evidence of a planetary system originating from primordial misalignment. In this chapter I present the observations, analysis and consequences of

these measurements. The manuscript[1] presented in this chapter is still in the preparation phase, but is expected to soon be ready for submission. I have performed most of the work and written the majority of the manuscript presented here, with the notably exception of parts of section 6.7 and the entirety of 6.8 involving the calculations of N-body co-planarship, secular resonance and primordial disk misalignment by co-authors Dawson and Zanazzi (where I however took the liberty of performing minor edits in order for the text to fit with the thesis layout). In addition, the autocorrelation and stellar rotation period was calculated by co-author Winn, while the RV extraction from HDS was performed by co-author Hirano.

6.1 Summary

This chapter reports the retrograde orbits of the mini-Neptune K2-290b and warm Jupiter K2-290c. This is the only known retrograde multi-planetary systems as well as the first example of Rossiter-McLaughlin measurements of several planets orbiting the same star. Most importantly it provides the first direct evidence of primordial misalignment of planetary orbits. The discovery has wide ranging implication for planet formation theories: it confirms that primordial disk misalignment plays a role in establishing stellar spin-orbit angles, suggesting that planetary systems having misaligned orbits is not always evidence they originate from dynamical perturbations instead of disk migration.

6.2 Introduction

Planetary systems having misaligned orbits with respect to their host star's spin have been seen as evidence they originate from dynamical perturbations instead of disk-driven migration. This conclusion assumes primordial disk alignment, consistent with measurements of multi transiting planet systems showing either low spin-orbit angles (Albrecht et al., 2013) or high spin-orbit angles excited after planet formation (Huber et al., 2013; Otor et al., 2016). Though the possibility of primordial misalignment has been theorised as a natural consequence of gravitational torques in the presence of additional stellar companions (Batygin, 2012), such planetary systems have remained elusive. Here we present the retrograde orbits of the mini-Neptune K2-290b and the warm Jupiter K2-290c (Hjorth et al., 2019); the first direct evidence of primordial misalignment in a planetary system and the first successful Rossiter-McLaughlin measurements of several planets in the same system. The co-planar inner mini-Neptune and the lack of an outer massive planet, implies that the retrograde orbits are due to the protoplanetary disk becoming misaligned previous to planet formation through torques from its nearby stellar companion. The existence of planetary systems showing primordial misalignments confirms that primordial disk misalignment plays a role in establishing stellar obliquities.

[1] Authors: Hjorth, M., Albrecht, S., Hirano, T., Winn, J. N., Dawson, R. I., Zanazzi, J. J., Knudstrup, E., Sato, B.

6.3 Observations

6.3.1 Observations of K2-290c

Two subsequent spectroscopic transits of K2-290c were observed on 25 April 2019 with HARPS-N@TNG (Cosentino et al., 2012) and on 12 June 2019 with HDS@Subaru (Noguchi et al., 2002). To securely establish a baseline, an additional three measurements were obtained outside of transit with HDS on 11 June 2019. The HARPS-N measurements partly covers the second half of the transit, while the HDS observations encompass 3/4th, beginning just around ingress. The first two observations on the HDS transit night were taken during nautical twilight, and the third suffered technical problems related to the CCD read-out. These three data points are therefore not included in our analysis. In total we secured 37 radial velocity (RV) data points, with exposures ranging from 900 – 1800 s on the two transit nights. The radial velocities are given in Table A4 for HARPS-N and in Table A5 for the HDS data.

During the HDS observations, K2-290's spectra were obtained with Image Slicer #2 and the Iodine (I_2) cell for precision wavelength calibrations. Usually, an I_2-free spectrum is obtained as a template for the RV analysis, but due to the lack of observing time on the transit night, we decided to skip this step. Instead, we used the combined high SNR HARPS/HARPS-N spectrum as a template for the RV analysis of HDS data. Except for this step to construct the RV template spectrum for K2-290, we followed the standard procedure to reduce the HDS data and extract RVs by the "forward modeling" technique (Sato et al., 2002).

6.3.2 Observations of K2-290b

In addition to the HARPS-N and HDS observations, we also secured Rossiter-McLaughlin observations of the small mini-Neptune using ESPRESSO@VLT. The transit happened on the night of the 20^{th} of July 2019. We were able to collect pre-ingress and in-transit data, though we experienced bad weather during the second part of the transit: clouds began obscuring the target, leading to low SNR and large offsets in the RVs. We therefore excluded the data points which were affected by the cloud coverage. The radial velocities were extracted from the spectra using the EsoReflex pipeline tool (Freudling et al., 2013). In total, we obtained 14 RV data points; five before ingress, and nine during the first part of the transit. The radial velocity data are given in Table A6.

6.4 Obtaining the spin-orbit angle of K2-290c

The change in radial velocities during transit is a consequence of the Rossiter-McLaughlin effect: the planetary occultation of the stellar disk leads to absorption line distortions, manifesting as radial velocities anomalies. The shape of the Rossiter-McLaughlin curve depends on the projected stellar rotational velocity $v \sin i_\star$ and the projected spin-orbit angle λ_c.

6.4.1 The projected spin-orbit angle:

To obtain the projected spin-orbit angle λ_c, we analysed the HARPS-N and HDS data. Including the previously published data (Hjorth et al., 2019) presented in Chapter 5, the analysis was performed simultaneous on the photometry, out-of-transit radial velocities, the HDS and HARPS-N data, based on the approach presented in that chapter. Both Rossiter-McLaughlin datasets were included in the likelihood function, and seven new parameters were added to describe the model: an RV offset for HDS γ, a jitter term for HDS $\sigma_{\rm jit,HDS}$, quadratic limb darkening parameters in the V-band $c_{1,\rm V}$ and $c_{2,\rm V}$, a micro- and macroturbulence parameter $v_{\rm mic}$ and $v_{\rm mac}$, the projected stellar rotational velocity $v \sin i_\star$ and the projected spin-orbit angle of the warm Jupiter λ_c. For $v \sin i_\star$, $c_{1,\rm V}$ and $c_{2,\rm V}$ we imposed Gaussian priors of 6.5 ± 1.0 km s^{-1}, 0.37 ± 0.1 and 0.31 ± 0.1 (Eastman et al., 2013). We maximised the likelihood and retrieved the posteriors by deploying an MCMC analysis (Foreman-Mackey et al., 2013) with 200 walkers for 10,000 steps, of which the first 5,000 steps were discarded, where convergence was reached. The posteriors and best-fit results (Fig. 6.1, Table 6.1) confirm the planetary orbit to be retrograde, with $v \sin i_\star = 6.77^{+0.66}_{-0.67}$ km s^{-1} and $\lambda_c = 145 \pm 10$ deg.

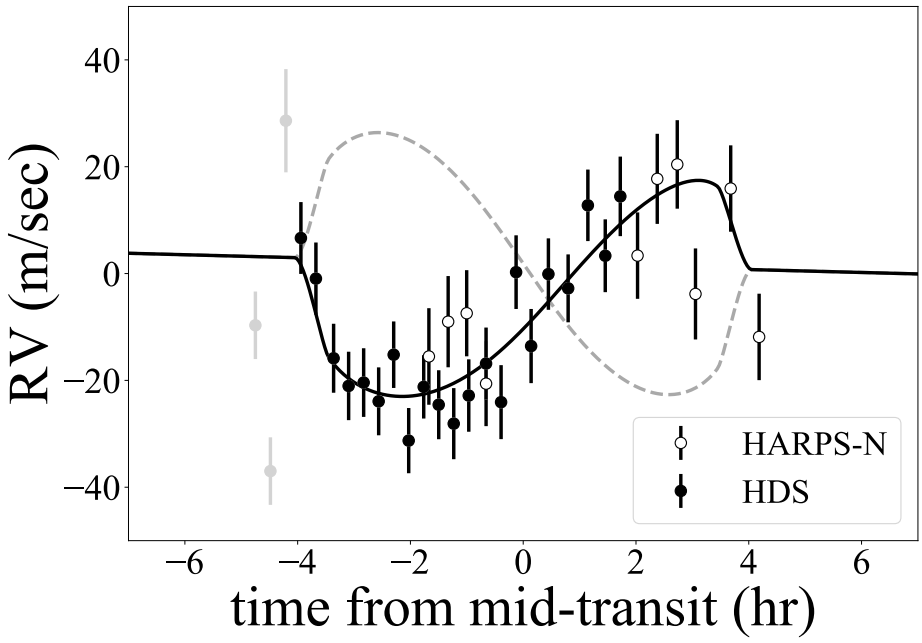

Figure 6.1: A plot of the radial velocity during transit of K2-290c centred around the mid-transit times. Open circles are the HARPS-N data (night of 25 April 2019), while solid circles are the HDS data (night of 12 June 2019). The grey points were obtained during twilight or had offsets caused by technical difficulties at the telescope. The dashed grey line shows a model with a 0 deg. alignment. The solid line shows the best-fit model to the data, with $v \sin i_\star = 6.77^{+0.66}_{-0.67}$ km s^{-1} and $\lambda_c = 145 \pm 10$ deg.

Table 6.1: Selected parameters for K2-290c, K2-290b and their host star. The projected stellar rotation and spin-orbit angles were obtained from a combined MCMC analysis on the photometry, radial velocities and Rossiter-McLaughlin data sets. The stellar rotation period was extracted from computing the autocorrelation of the photometry. The stellar inclination was derived from this, and the 3D spin-orbit angles were determined by combining these results with the orbital inclinations of the planets.

Parameter	Value
Stellar rotation period $P_{\rm rot}$ (days)	6.63 ± 0.06
Stellar inclination $i_\star$ (deg)	36 ± 5
Proj. stellar rotation velocity $v \sin i_\star$ (km s^{-1})	$6.77^{+0.66}_{-0.67}$
Proj. spin-orbit angle of planet c λ_c (deg)	145 ± 10
3D spin-orbit angle of planet c ψ_c (deg)	118 ± 5
Proj. spin-orbit angle of planet b λ_b (deg)	166^{+52}_{-67}
3D spin-orbit angle of planet b ψ_b (deg)	123^{+10}_{-12}

To investigate the robustness of our results, we repeated several different versions of the analysis. One important variant was to check whether the addition of the three excluded HDS data points would make a difference. Furthermore, since K2-290c has an orbit consistent with an eccentricity of zero, we also tested whether demanding a circular orbit made significant changes to the result. In addition, we tested whether we could recover the spin-orbit angle, by examining only the HDS Rossiter-McLaughlin data, only the HARPS-N Rossiter-McLaughlin data or only both. This was done with an orbital semi-amplitude K_c kept fixed through a Gaussian prior, but also with it set completely free, in order to take any short-term stellar noise into account. In all our different test cases, we recovered $v \sin i_\star$ and λ_c within 1σ of the original analysis. This makes K2-290 the only known retrograde multi-transiting planet system.

6.4.2 The 3D spin-orbit angle:

For projected obliquities larger than 90 deg the projection gives an upper limit on the obliquity ψ_c itself. We probed the stellar spin inclination $i_\star$ by computing the auto-correlation of the *K2* photometry. From this we established the stellar rotation period to be 6.63 ± 0.06 days. By combining the rotation period with the radius of the star, and assuming rigid-body rotation, we were able to calculate the stellar inclination $i_\star$:

$$\sin i_\star = \frac{v \sin i_\star}{v} = \frac{v \sin i_\star}{(2\pi R_\star)/P_{\rm rot}} \tag{6.1}$$

We used this value, in addition to the projected spin-orbit angle λ_c and the planet's orbital inclination $i_{\rm orb}$, to calculate the three-dimensional spin-orbit angle ψ_c (Fabrycky and Winn, 2009):

$$\cos \psi_c = \sin i_\star \sin i_{\rm orb} \cos \lambda_c + \cos i_\star \cos i_{\rm orb} \tag{6.2}$$

Assuming rigid body rotation, this translates into $i_\star = 36 \pm 5$ deg, resulting in the 3D spin-orbit angle $\psi_c = 118 \pm 5$ deg.

6.5 Obtaining the spin-orbit angle of K2-290b

With K2-290 being a multi-transiting system, we are either seeing it along the line of nodes or the two planets share the same orbital plane. If the two planets are located in the same orbital plane, K2-290b is either retrograde to a similar degree as K2-290c, or prograde with a shift of ~ 180 deg. These three cases can be seen in Fig. 6.2.

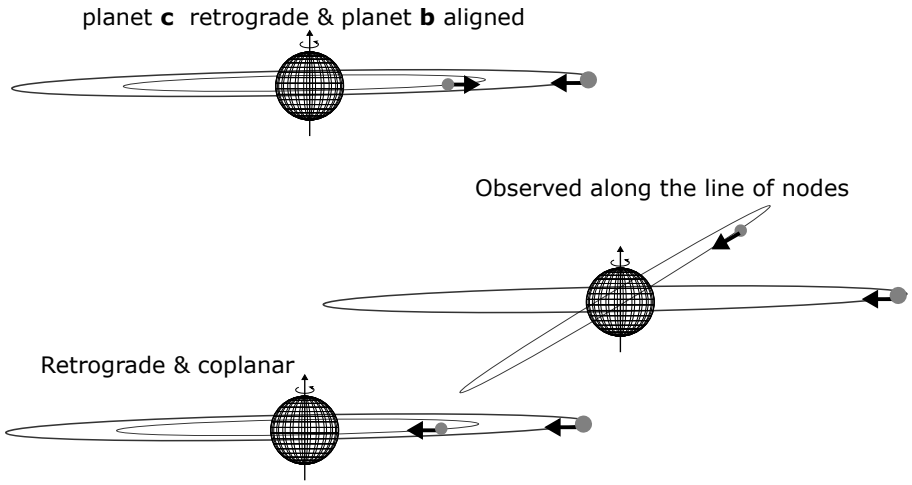

Figure 6.2: The three possible configurations for the orbits of planet b and planet c in K2-290. Top: planet b is prograde and planet c is retrograde. Middle: we are seeing the planets along the line of nodes. Bottom: both planets are retrograde.

We simulated the longterm evolution of the system, assuming circular orbits for both planets. Both a coplanar configuration and a configuration in which planet b's orbit is aligned with the host star's spin are stable over long timescales of at least 27 Myr. In the former case, both planets always transit; in the latter case, at times when at least one planet transits, the other planet transits too 15% of the time. We simulate transit time and duration variations using our custom-built code (e.g., (Dawson et al., 2014)) and find that in both the coplanar and non-coplanar case, they are too small to be detectable with the current dataset and unlikely to be detectable in future datasets without a huge increase in precision and/or baseline. Therefore we cannot rule out non-coplanar solutions solely on the basis of the expected dynamical interactions between planet b and c.

However, creating a retrograde outer planet with $M = 0.774\ M_{\rm Jup}$ through planet-planet scattering (Rasio and Ford, 1996), without destabilising a prograde, inner small $M < 21.1\ M_\oplus$ sibling, seems highly unlikely. Furthermore,

the orbital solution for the warm Jupiter is consistent with circular, conflicting with its spin-orbit angle being enhanced through Kozai-Lidov excitations (Naoz, 2016). In addition, since planet b and c are tightly coupled, the M-dwarf binary companion cannot cause a mutual inclination between them. All of these considerations points towards the mini-Neptune moving in the same direction as the warm Jupiter.

In order to determine whether the mini-Neptune is pro- or retrograde, we analysed the ESPRESSO data obtained during the spectroscopic transit of planet b. As mentioned previously, the weather turned bad during the second part of the transit, and we therefore did not include data points which were affected by the cloud coverage. The remaining RVs were analysed simultaneous to the photometric, radial velocities and additional Rossiter-McLaughlin data from HDS and HARPS-N for planet c, in the same way as described in section 6.4. During this we introduced an RV offset and jitter term for ESPRESSO as additional parameters, as well as the projected obliquity for planet b λ_b. The data and best-fit model is shown in Fig. 6.3, where we obtained a projected spin-orbit angle of $\lambda_b = 166^{+52}_{-67}$ deg, translating into a 3D spin-orbit angle of $\psi_b = 123^{+10}_{-12}$ deg. This means that planet b and c are both retrograde, and is the first example of successful Rossiter-McLaughlin measurements of several planets in the same exoplanetary system.

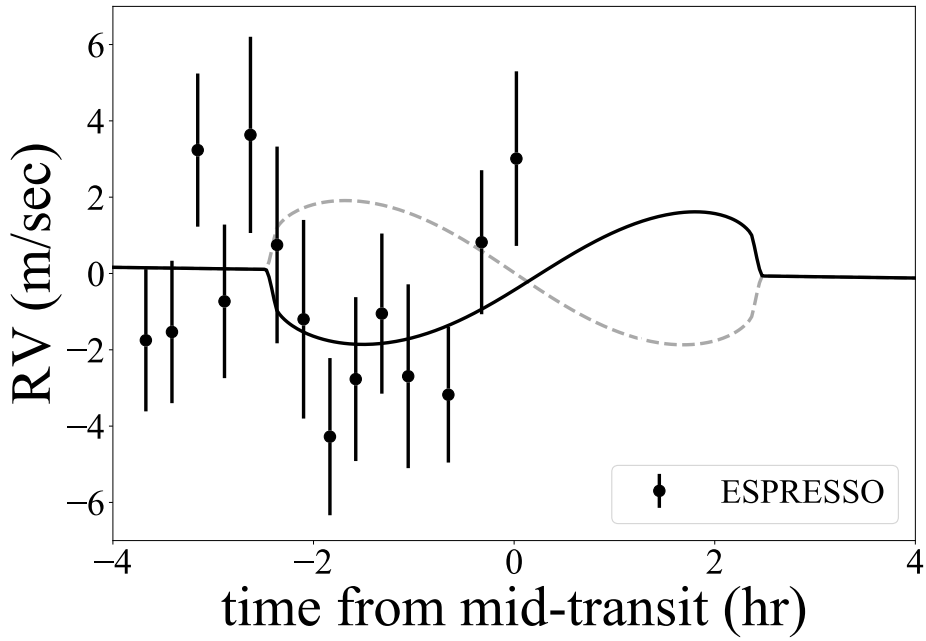

Figure 6.3: The Rossiter-McLaughlin effect of K2-290b. Same as Fig. 1, but for the mini-Neptune K2-290b. The data are obtained through ESPRESSO on the night of 20 July 2019. The solid line shows the best-fit model to the data with $\lambda_b = 166^{+52}_{-67}$ deg.

In addition to the analysis above, we tried to use Doppler Tomography on the ESPRESSO data, but were unable to extract the Doppler shadow. However, this absence of signal is consistent with simulations of the shadow, using the noise level achieved with ESPRESSO and a macroturbulence of 5 km s^{-1} from the best fit to the combined data. Before submitting the manuscript, we will try to enhance the shadow signal using the concentration method as described in Chapter 3.4.

6.6 Formation scenarios of K2-290

Having secured measurements of the spin-orbit angles of K2-290b and K2-290c, we can interpret its implications for the formation history of the system. Planet-planet scattering is most likely not the cause of the large spin-orbit angles; It is hard to produce warm Jupiters with retrograde obliquities this way (Beaugé and Nesvorný, 2012), and warm Jupiters produced with planet-planet scattering tend to have significant eccentricities (Anderson et al., 2019), inconsistent with the circular nature of K2-290c. Another misalignment mechanism that can take place after planet formation, is torques exerted onto tightly-coupled planets by an inclined external companion. This scenario is behind the moderate misalignment of Kepler-56 (Huber et al., 2013) and the polar orbit of HD 3167c (Dalal et al., 2019), the only other multi transiting systems with a large spin-orbit angle. However, the origin behind the inclination of these unseen third companions is unknown.

In the discovery analysis of K2-290, the linear RV trend was consistent with zero, but on a short baseline of ∼200 days. To expand this, we acquired two new RV points from HARPS-N in June 2019, increasing the time span to ∼ 500 days. This revealed a linear trend of $\dot{\gamma} = 11 \pm 7$ m s^{-1} yr^{-1}. With a projected distance of 113 ± 2 au, we expect the nearby M-dwarf to contribute approximately $5 - 6$ m s^{-1} yr^{-1}, consistent within 1σ with the linear trend.

6.7 Secular resonance

The M-dwarf companion induces a similar precession frequency of planet c's orbit and of the oblate primary's spin. This secular resonance can cause a large amplitude misalignment. We model the secular evolution of the orbits of the coupled planet b, planet c, M-dwarf companion, and primary star (Lai et al., 2018), using the 1σ value of $M_b = 5.8 M_\oplus$ from the analysis in the previous chapter. We find that the secular resonance could turn on either after the dissipation of the gas disk and/or turn on or off as the stellar radius evolves. Planet b and c remain strongly coupled and co-planar with each other. The misalignment through a late-stage resonance crossing requires a sufficiently low mass for planet b (to avoid coupling the planets too strongly to the stellar spin) and small semi-major axis for the M-dwarf. An example of the variations in spin-orbit angles of planet c over time can be seen in Fig. 6.4.

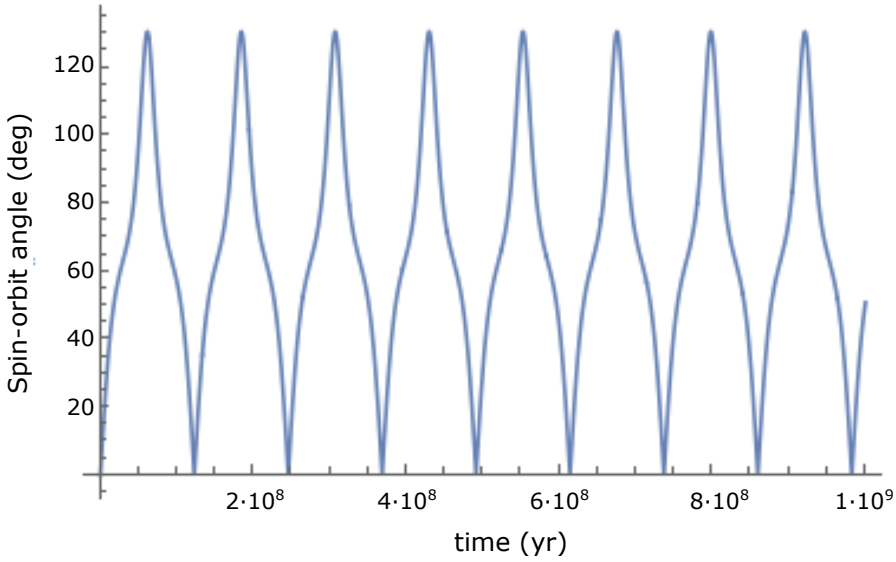

Figure 6.4: An example of variations in planet c's spin-orbit angle near the resonance frequency if we assume the M-dwarf companion to have been born with a 50 deg mutual inclination at a distance of 125 au.

Through secular resonances we therefore have two scenarios that could have lead to the retrograde orbits: 1) a primordial misalignment of the proto-planetary disk due to a resonance crossing between the disk-primary precession frequency and disk-companion precession frequency or 2) late-stage co-planar flipping of the planets due to a resonance crossing between the primary-M-dwarf precession frequency and the planets-M-dwarf precession frequency. One way to distinguish between these would be to get a better constraint on planet b's mass or the orbit of the M-dwarf companion. Since this cannot be done with the current data at hand, we will alternatively in the next section show that the disk *not* becoming misaligned is highly unlikely.

6.8 Primordial disk misalignment

A natural explanation for the retrograde orbit of K2-290c is primordial misalignment of the proto-planetary disk by the nearby stellar companion (Batygin, 2012).

A point in favour of primordial misalignment comes from eccentricity (Dong et al., 2014) and companionship (Huang et al., 2016) studies of warm Jupiter systems: low eccentricity warm Jupiters have inner low-mass planetary companions, suggesting an *in situ* or disk migration origin (Dawson and Johnson, 2018), and incompatible with high-eccentricity migration (Mustill et al., 2015).

Through primordial disk misalignment, a range of spin-orbit angles may be excited for moderate inclinations between the disk and binary orbital planes (Batygin and Adams, 2013; Lai, 2014) ($\theta_{\rm dB} \sim 30$ deg – 60 deg): such inclinations are not uncommon for circumstellar disks in proto-stellar binary systems (Stapelfeldt et al., 1998; Jensen and Akeson, 2014). To test if the binary companion could have produced disk misalignment, we calculated the system's secular evolution due to mutual gravitational torques between the planets, oblate star, disk, and the nearby M-dwarf companion, assuming the planets formed early and in-situ. More detailed models including migration and photo-evaporation typically give larger primordial misalignments at the end of the proto-planetary disk's lifetime (Zanazzi and Lai, 2018b). For details on the model and justifications of parameter values, see Lai (2014); Zanazzi and Lai (2018b). Consider a host star of mass $M_\star$, radius $R_\star$, rotation frequency $\Omega_\star$, with a (circular) inclined binary companion of mass $M_{\rm B}$ and semi-major axis $a_{\rm B}$, surrounded by a circumstellar disk with inner (outer) truncation radii $r_{\rm in} = 4R_\star$ ($r_{\rm out} = 50$ au), and surface density profile (assuming $r_{\rm in} \ll r_{\rm out}$)

$$\Sigma(r,t) \simeq \frac{M_{\rm d}(t)}{2\pi r_{\rm out} r}, \tag{6.3}$$

where

$$M_{\rm d}(t) = \frac{M_{\rm d0}}{1 + t/t_{\rm v}} \tag{6.4}$$

is the disk mass, $t_{\rm v} = 0.5$ Myr is the viscous time, and $M_{\rm d0} = 0.1$ $M_\odot$ is the initial disk mass. We assume planets b,c with masses $M_{\rm b}, M_{\rm c}$ and semi-major axis $a_{\rm b}, a_{\rm c}$ form with the disk (at $t = 0$) at the locations we observe them today. We take $M_{\rm B}$, $M_{\rm c}$, $a_{\rm b}$, and $a_{\rm c}$ to be equal to their observationally inferred values, with $R_\star = 2$ $R_\odot$ and $\bar\Omega_\star = \Omega_\star/\sqrt{GM_\star/R_\star^3} = 0.1$ during the host star's pre-main sequence phase. We assume the binary's semi-major axis is greater than the projected separation ($a_{\rm B} > 113$ au (Lai et al., 2018)), and the mass of planet b to be equal to the 3σ upper limit from RV measurements ($M_{\rm b} = 21.1$ $M_\oplus$ (Lai et al., 2018)).

We use the secular equations for the dynamical evolution of planet-forming star-disk-binary systems (Zanazzi and Lai, 2018b) to model the excitation of primordial misalignments by the binary's gravitational torque. The difference of this calculation is to add the gravitational influence of both planets b and c to the star-disk $\tilde\omega'_{\rm sd}$ and disk-star $\tilde\omega'_{\rm ds}$ precession frequencies (see eqs. 65-66 in (Zanazzi and Lai, 2018b)):

$$\tilde\omega'_{\rm sd} = \tilde\omega_{\rm sd} + \omega_{\rm sb} + \omega_{\rm sc}, \tag{6.5}$$

$$\tilde\omega'_{\rm ds} = \tilde\omega_{\rm ds} + (L_{\rm b}/L_{\rm d})\omega_{\rm bs} + (L_{\rm c}/L_{\rm d})\omega_{\rm cs}, \tag{6.6}$$

where $L_{\rm d} \simeq (2/3)M_{\rm d}\sqrt{GM_\star r_{\rm out}}$ is the total disk orbital angular momentum, $L_i = M_i\sqrt{GM_\star a_i}$ are the planets' orbital angular momentum ($i =$ b, c), and

the precession frequencies

$$\omega_{\,\mathrm{s}i} = \frac{3k_q}{2k_\star}\bar{\Omega}_\star \left(\frac{M_i}{M_\star}\right)\frac{\sqrt{GM_\star R_\star^3}}{a_i^3}, \tag{6.7}$$

$$\omega_{i\,\mathrm{s}} = \frac{3k_q}{2}\bar{\Omega}_\star^2 \left(\frac{R_\star}{a_i}\right)^2 \sqrt{\frac{GM_\star}{a_i^3}}\,. \tag{6.8}$$

The stellar rotation/inertia parameters $k_q \simeq 0.1$ and $k_\star \simeq 0.2$ during the pre-main sequence phase, and we neglect the torque on the planets from star B ($\tilde{\omega}'_{\mathrm{dB}} \simeq \tilde{\omega}_{\,\mathrm{dB}}$).

Figure 6.5 displays the main result of the these calculation, showing the time evolution and excitation of primordial misalignments or mutual star-disk inclinations $\theta_{\,\mathrm{sd}} = \cos^{-1}(\hat{\boldsymbol{s}}\cdot\hat{\boldsymbol{l}}_{\,\mathrm{d}})$ excited by the binary companion, for different initial disk-binary mutual inclinations $\theta_{\,\mathrm{db}} = \cos^{-1}[\hat{\boldsymbol{l}}_{\,\mathrm{d}}(0)\cdot\hat{\boldsymbol{l}}_{\,\mathrm{B}}]$ ($\hat{\boldsymbol{s}}$ is the host star's stellar spin axis, $\hat{\boldsymbol{l}}_{\,\mathrm{d}}$ is the disk's orbital angular momentum unit vector, $\hat{\boldsymbol{l}}_{\,\mathrm{B}}$ is the binary's orbital angular momentum unit vector) and binary semi-major axis values $a_{\,\mathrm{B}}$. We see after secular resonance occurs in the system (Batygin and Adams, 2013; Lai, 2014) ($\tilde{\omega}'_{\mathrm{sd}} \sim \tilde{\omega}_{\,\mathrm{dB}}$), large primordial misalignments are generated by star-disk-binary interactions, consistent with the measured stellar obliquity $\psi_c = 118 \pm 5$ deg for a range of parameter values. Since we took the inner planet's mass to be the 3σ upper limit obtained from RV measurements, the suppression of primordial misalignments by short-period, massive planets will not occur for this system (Zanazzi and Lai, 2018b) (for the parameter values investigated).

All in all, we find for a range of disk-binary inclinations and binary semi-major axis values, the measured 3D spin-orbit angle ψ_c can be produced primordially. Additional effects, such as planetary migration or photo-ionization of the disk, will not affect our principal conclusions (Zanazzi and Lai, 2018b). It is possible to have a disk which does not undergo secular resonance and get retrograde stellar obliquities through the late-stage secular resonances. But, for the disk to not get misaligned it would need a very fast dissipation timescale, or a lot of mass near the host star, both of which are not supported by observations. It is much more likely that star-disk-companion interactions have generated primordial misalignments in this system.

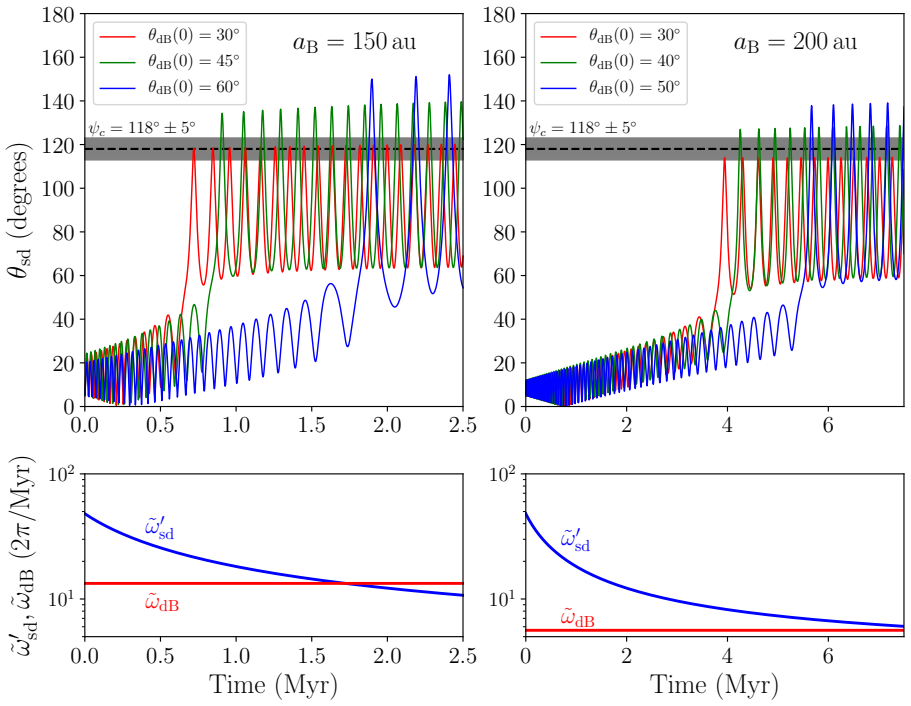

Figure 6.5: Primordial Misalignments from planet-star-disk-binary interactions in K2-290. Top panel shows the mutual inclination between the host star's equatorial plane and disk orbital plane (θ_{sd}) with time for the initial disk-binary inclinations $\theta_{dB}(0)$ and binary semi-major axis a_B indicated, which will become the 3D spin-orbit angle ψ_c (dashed black line with errors in grey band) after the disk dissipates. A range of parameter values can excite θ_{sd} to the observed 3D spin-orbit angle ψ_c. Bottom panel shows the star-disk $\tilde{\omega}'_{sd}$ and disk-binary $\tilde{\omega}_{dB}$ precession frequencies with time. Large primordial misalignments θ_{sd} are excited when secular resonance occurs in the proto-stellar system ($\tilde{\omega}'_{sd} \sim \tilde{\omega}_{dB}$).

6.9 Conclusion

With most post-formation scenarios ruled out, and late-stage co-planar resonance flipping disfavoured over a primordial tilt of the disk, the above analyses gives a clear picture of the formation history of K2-290: the stellar companion acted to primordially misalign the proto-planetary disk of the host star. This misalignment was followed by the formation and possibly disk migration of its two planets. Their misaligned birthplace ensued they were created in retrograde orbits. Depending on whether planet b has a large or small mass, the system then either 1) remained misaligned due to the inefficiency of late-stage resonance crossing for a large planet combined with the large stellar-Jupiter distance and tidal interactions from hot host stars being presumably weak, or 2) went through secular resonance cycles, where we now see it near its retrograde stage. The

existence of primordial misaligned planets has wide-ranging implications for our understanding of planet formation. E.g., observations of large spin-orbit angles of hot Jupiters (Albrecht et al., 2012), have been seen as evidence for a high-eccentricity migration origin, as opposed to disk migration. However, this relies on the assumption that the stellar equator and proto-planetary disk were originally aligned. Though our observations do not directly apply to hot Jupiters, they do provide evidence for the existence of primordial misaligned proto-planetary disks, suggesting that the assumption of primordial alignment is not always valid.

7

Pushing the limits: the spin-orbit of Trappist-1

With its very small amplitude, the Rossiter-McLaughlin measurements of K2-290b was a great example of how the limits of current astronomy are continuously pushed in order to explore a wider parameter space of spin-orbit observations. However, so far no such measurements have been published on Earth-sized planets. One of the most promising targets for achieving Rossiter-McLaughlin obliquities for such small worlds are M-dwarfs planetary systems. In connection to this, and as part of the authors research stay at Tokyo Institute of Technology, it was examined whether our current models are feasible for describing the velocity anomaly in these kind of systems. This is the topic of this chapter. The entire project is lead by Prof. Teruyuki Hirano, who will also be the lead author of the future publication of the data presented here. We caution that the test cases on the following pages is still a work in progress, and might not be a part of the final publication of the Trappist-1 data. However, even without these data, the velocity anomaly models constructed for solar-like stars deserve scrutiny in itself before mindlessly being adapted to M-dwarf systems. I have written the entirety of this Chapter, and done most of the work described here, with the exception of the analysis behind and making of the original version of Fig. 7.1.

7.1 Rossiter-McLaughlin measurements of small planets

As is apparent from eq. 3.9, large planets have higher Rossiter-McLaughlin velocity anomaly amplitudes than small planets, due to their transit depths being shallower. Likewise, the Doppler shadow for small planets is also narrower and harder to detect. This has resulted in only a few sub-Saturn sized planets having spin-orbit angles measured through the Rossiter-McLaughlin technique (with some of these being disputed): the three Neptune-sized HAT-P-11 (e.g Winn et al., 2010), 55 Cnc e (Bourrier and Hébrard, 2014; López-Morales et al., 2014) and GJ 432c (Bourrier et al., 2018), and also the mini-Neptune K2-290b presented in the previous chapter. Though the sample size is small, the prospect of measuring the spin-orbit angle for small planets is exciting. Not only might the knowledge of the obliquity of small planets be useful in the case of examin-

ing co-planarity in multi-planet systems (as we saw in the case of K2-290), the spin-orbit angle for small planet system might in itself reveal clues about the evolution of planetary systems in general.

The reason for the modest sample size of small planets is a combination of the shallow transit depth and the precision limit of accessible telescopes. In the previous chapter we saw how to circumvent this by using one of the best-precision spectrographs currently available. Another approach is to observe planetary systems with deep transits. To combine this with the goal of examining small planets, we need to target systems containing small host stars, e.g. planets orbiting M-dwarfs.

To obtain precise Rossiter-McLaughlin measurements for this kind of star, we need to go to the infrared. Instrument-wise, a suitable telescope for the job is e.g. the 8.2m SUBARU telescope attached with the IRD (Infrared Doppler Instrument, Kotani et al., 2018), which strives to reach a 1 m s^{-1} uncertainty. While this kind of telescope makes observations of M-dwarf hosts possible, another issue lies on the theoretical side: though several analytical models have been produced to recreate measurements of the the velocity anomaly caused by the Rossiter-McLaughlin effect (see Chapter 3), these were made with solar-type stars in mind. But, M-dwarfs have numerous absorption lines due to their atmospheres larger metal content, resulting in many of the lines being blended with each other. This might change the way we need to model the velocity change, as e.g. the model of Hirano et al. (2011) assumes non-blended lines.

7.2 Testing velocity anomalies of Trappist-1

Arguably the two most famous M-dwarf planetary systems are Proxima b (Anglada-Escudé et al., 2016) and Trappist-1 (Gillon et al., 2017). The latter contains seven transiting Earth-like planets orbiting a slow rotating M-dwarf with $J = 11.4$. The feasibility of measuring the Rossiter-McLaughlin effect for this system immediately caught the eye of many astronomers working on obliquities, e.g. Cloutier and Triaud (2016) which estimated the amplitude of the signal to be $\sim 40 - 50$ m s^{-1} for the largest planets. Extracting the spin-orbit angle for this system would illuminate our understanding of planet formation for Earth-sized planets, as we expect alignment for terrestrial-planet systems, assuming a well-aligned protoplanetary disk.

On the night of August 30th 2018 the Trappist-1 planets e, f and b all occulted their star within a time span of seven hours. The spectroscopic transits were observed with the IRD@SUBARU by PI Prof. Teruyuki Hirano. The resulting radial velocities are shown in Fig. 7.1, with the black line showing a tentative best fitted model assuming no blended lines. From the data, the approximated amplitude of Cloutier and Triaud (2016) seems to be overestimated by an order of magnitude, possibly due to Reiners and Basri (2010) reporting a too large projected stellar velocity. This is in agreement with an inspection of the spectroscopic data which suggests a $v \sin i_\star$ closer to a value of $1 - 2$ km s^{-1}, as

opposed to the literature value of 6 ± 2 km s^{-1}. Assuming the three planets are all completely co-planar, results in a joint best-fit spin-orbit angle of -9^{+33}_{-29} deg and a projected rotation $v \sin i_\star = 1.30^{+0.37}_{-0.36}$ km s^{-1}.

To make sure the comparison between the model and data is correct, we examine the possibilities of testing whether the model presented in Hirano et al. (2011) is a good description for M-dwarfs. However, it is difficult to analytically take the blending of lines into account when constructing a model for the velocity deviation. Instead, an alternative approach is to follow the procedure of early days Rossiter-McLaughlin measurements of planets and do the model calculations numerically on simulated results (se e.g. Winn et al., 2005). This is done following the same procedure described in Hirano et al. (2011) for originally testing the model, with the macroturbulence and rotational-macroturbulence kernels being given there.

First, an M-dwarf spectrum matching the physics of Trappist-1 is artificially created. This is done by obtaining a spectrum from the PHOENIX synthetic library (Husser et al., 2013) with $T_{\rm eff} = 2500$ K, $\log g = 5.0$, [Fe/H] $= 0.0$ and [α/M] $= 0.0$, which are the grid parameters closest to the system parameters from Gillon et al. (2016). The spectrum is then normalised by creating a spline function to the 95th percentile of each spectra values in bins of a certain size. The normalised spectrum is subsequently broadened by a rotational-macroturbulence kernel in order to obtain a realistic representation of the Trappist-1 stellar spectrum. Here we selected parameter values of $v \sin i_\star = 2$ km s^{-1}, $\beta = 1$ km s^{-1} and $\zeta = 2$ km s^{-1} as a best guess for the stellar broadening by inspecting the line shape.

As a starting point, the testing of the feasibility of the velocity anomaly model on M-dwarfs were done on planet b in the Trappist-1 system, with system parameters from the discovery paper. The next step is then to insert the effect of a planetary transit into the spectrum of the star, for certain epochs around an occultation. To include the planet in the spectrum, a copy of the original unbroadened normalised spectrum is Doppler-shifted by the sub-planet velocity at each observational epoch. This sub-planet spectrum is then multiplied by the instantaneous decrease in flux given by eq. 3.13 and convolved with a macroturbulence kernel. The total spectrum can then be obtained by subtracting the sub-planetary spectrum from the stellar spectrum.

To extract the velocity anomaly from the created spectra, we cross-correlate each individual spectrum at each epoch with the out-of-transit synthetic stellar spectrum. This cross-correlation is then fitted a Gaussian function in order to obtain the radial velocity. Fig. 7.2 displays the simulated radial velocities for planet b obtained in this way, together with the analytical model for a cross-correlated spectrum, as presented in Chapter 3. From this preliminary analysis, we see only a very small difference in the analytical and numerical values of the Rossiter-McLaughlin velocity deviations, much smaller than the current achievable instrument precision. However, it should be noted that we are still testing

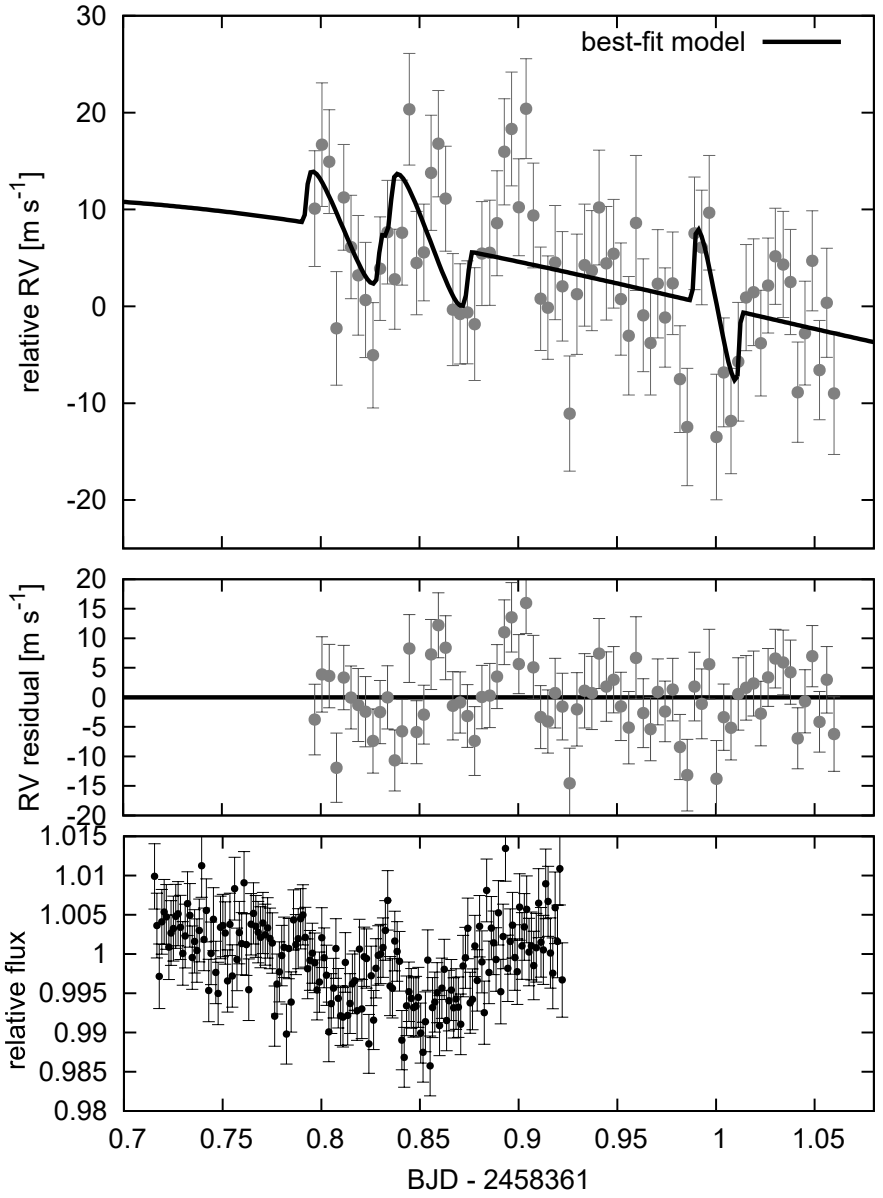

Figure 7.1: The three transits of the Trappist-1 planets e, f and b on the night of August 30th 2018 as observed from IRD@SUBARU. The top panel shows the spectroscopic transit with a preliminary best-fit using the Rossiter-McLaughlin model described in Hirano et al. (2011). The middle panel shows the residual between the data and best fit model. The bottom panels shows the photometric data at the beginning of the night, with observations unfortunately cut short due to bad weather. These were obtained using the 1m telescope at the McDonald Observatory.

whether our original normalisation of the simulated spectra are sufficient, as this process proved to be difficult due to the many absorption lines. For future work we would also like to repeat these tests using the different system parameters, to see whether changing e.g. $v \sin i_\star$ might impact the results. These kinds of tests will not only be important for studying the Rossiter-McLaughlin effect in Trappist-1, but also for the examination of the slew of new M-dwarf planetary systems which will be detected with *TESS*.

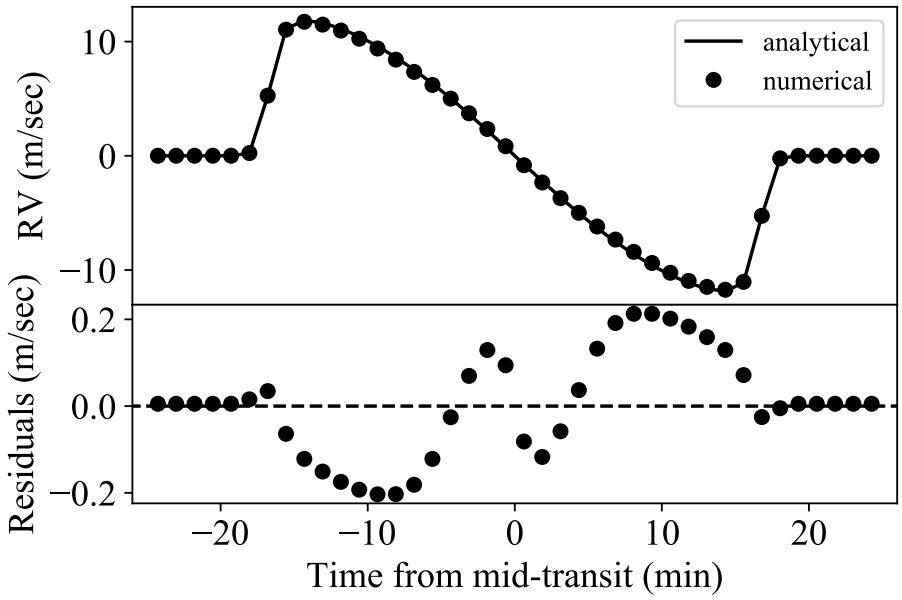

Figure 7.2: The preliminary results of the Rossiter-McLaughlin velocity deviations from numerical simulated data and analytical calculations.

8

Conclusion

This thesis has been a presentation of the work carried out during my PhD studies. A general introduction has been given to the current state of research into planet formation and hot Jupiters origin, together with a description of how measurements of the spin-orbit angle of multi-planet systems or systems containing warm Jupiters can probe different migration scenarios. In connection to this, several of my first-author research manuscripts were presented. In this chapter a brief summary of the thesis will be given. I will also discuss the implications of the research presented here as well as possibilities for the future of spin-orbit observations and origin studies.

8.1 Summary and conclusions

The focus of this PhD has been to expand the knowledge on planet formation and the orbital orientation of different configurations of planetary systems, particular in connection with studying the origin of gas giants. This is an ever-evolving research field, with a large amount of information obtained through spin-orbit investigations conducted within the last decade. In Chapters 1 and 2 I explained my interest in this topic, and justified the current consensus on the origin of giant exoplanets in the exoplanet community: Jupiters form far-out in their disk, and then move inwards by either disk and/or high-eccentricity migration. I explained how it might be possible to distinguish by conducting observations of the spin-orbit angle of either multi- or warm Jupiter systems. I also explained the possibility of both migration channels being at play, by examining the distribution of aligned and misaligned hot host star systems. Chapter 3 dealt with how to measure the spin-orbit angle using the Rossiter-McLaughlin effect. Here I presented the two techniques connected to this; measuring the velocity anomaly or observing the Doppler shadow. In connection to this, I gave a detailed explanation of the physics behind the stellar line-shape, and how it deviates during a spectroscopic transit.

Armed with these two techniques to observe obliquities, I presented an example of the utilisation of both in Chapter 4. This chapter is about the discovery and characterisation of MASCARA-3, a hot Jupiter in an aligned system. The host star is bright with a rotation velocity of $v \sin i_\star \sim 20$ km s^{-1}. This creates the

perfect conditions for acquiring both the Doppler shadow and measuring radial velocities, both of which my collaborators and I obtained using the SONG telescope. Due to this, we were able to both get information on the planetary radius and mass as well as establishing the alignment of the orbit. The temperature of the host star suggested a slow tidal timescale. Together with it's low obliquity, this was consistent with the hot Jupiter originating from disk migration. This was the first time SONG was proved capable of measuring the radial velocity anomalies during transit, but with the constant arrival of new, bright *TESS* targets, it certainly will not be the last.

In order to examine and expand the sample of multi-planet systems and warm Jupiters, I turned my attention to K2-290; a triple-star system containing a warm Jupiter and mini-Neptune. Chapter 5 was about the discovery and characterisation of this system. It's multiplicity and low eccentricity implied *in situ* formation or a disk migration origin. To examine this further, I set out to retrieve it's obliquity together with my collaborators; the subject of Chapter 6. Here the HDS and HARPS-N measurements of K2-290c were presented, revealing the first known retrograde multi-planet system. We also obtained meter-precision ESPRESSO data for K2-290b, making this the first case of getting Rossiter-McLaughlin measurements for two planets in the same system. Through simulations of the impact of the close-by stellar companion on the orbital architecture, we were able to establish the retrograde nature being of primordial origin – the first case of direct evidence for the spin-orbit angle of a system stemming from the primordial misalignment of it's proto-planetary disk. Though this result is not directly applicable to hot Jupiters, the mere existence of such a planetary system opens the door for disk migration being a valid alternative interpretation to explain large spin-orbit angles.

In Chapter 7 I continued my efforts in pushing the observational limits for Rossiter-McLaughlin measurements, by presenting the spectroscopic transit of three planets in the seven-Earths system of Trappist-1 – all observed in the same night. Here I examined whether our current velocity anomaly models hold true for M-dwarfs system, and presented preliminary results suggesting they do. This is not only important for these particular observations, but will also be applicable to follow-up observations through e.g. the CARMENES instrument and Hobby-Eberly Telescope of the many M-dwarf systems *TESS* will discover. In the future I would like to study the results in more detail by making sure these preliminary simulations are correctly performed and by examining the effect of changing different stellar parameters such as the metallicity.

Combining the results of this thesis, I have measured the orbital architecture of three very interesting systems, and have uncovered a few more pieces to the puzzle of planet formation. The scientific field of exoplanets is now one step closer to having unlocked the secret behind warm and hot Jupiters' origin. In particular, planet formation in a tilted disk is no longer just a hypothesis, but have actually been inferred in the case of K2-290. This opens the possibilities of planets in other system being born in primordial misaligned disks, which might be an alternative

explanation for some Jupiters with large spin-orbit angles. In the context of some planetary systems being believed to originate from dynamical interactions, this might imply that hot Jupiters originate from both disk and high-eccentricity migration. In addition, with the arrival of new planetary systems combined with the constant improvement in observing capabilities, the parameters-space of which the spin-orbit angle is known is being progressively extended.

Important contributions from this PhD

- **SONG radial velocities during transit:** SONG will be an important tool in follow-up and spin-orbit studies of bright *TESS* targets. In this thesis it was shown how the telescope has been able to deliver spectroscopic transit data, both in the form of the Doppler shadow, but for the first time also as radial velocity anomalies, as was the case for MASCARA-3.
- **First Rossiter-McLaughlin of two planets in one system:** In this thesis, the discovery and characterisation of the multi-planet triple star system K2-290 was presented. With the help of HARPS-N, HDS and ESPRESSO, it became the first example of obtaining multiple successful Rossiter-McLaughlin observations for several planets in the same planetary system.
- **First retrograde multi:** K2-290 is the only known retrograde multi-planet system, and one of three known misaligned multis.
- **First direct evidence of primordial misalignment:** The retrograde orbits of K2-290 is shown to originate from the misalignment of the primordial disk; the first example where this mechanism has been shown to cause the misalignment. This could have consequences for planet formation theories, as some of the other misaligned planetary systems might have suffered the same fate.
- **Trappist-1 Rossiter-McLaughlin:** The Rossiter-McLaughlin effect from the transit of three planets in the same night was shown for the M-dwarf seven-planet system of Trappist-1.
- **M-dwarf Rossiter-McLaughlin model works:** Numerical simulation of the Rossiter-McLaughlin effect in an M-dwarf has shown to match with the analytical expression. We caution that this is a preliminary result.

8.2 A bright outlook: Prospects in probing new spin-orbit regions and the future of origin studies

While the number of planets with observed spin-orbit angles have soared in the last decade, most of them have been of hot Jupiters. However, increasing the number of these kind of systems is still warranted: for example, more observations of hot Jupiters orbiting hot hosts might improve our understanding of the primordial spin-orbit distribution, since these are not expected to have been sculpted by tidal interactions (see Chapter 1). As discussed in this thesis, an additional approach when studying planet origins is to extend the region of other kind of systems. One of the main obstacles in achieving the obliquity for multi-planet systems and warm Jupiters have been the small amount of bright, candidate targets. With the launch of *TESS* (Ricker et al., 2015), the entire sky is now being probed, and the mission has already revealed many new planet candidates. The brightness of many of these means that it will be easier to do spectroscopic follow-up. The next year *TESS* will cover the northern hemisphere, making it possible for northern telescopes such as SONG to characterise these new worlds. I believe the coming years will offer a substantial increase in the sample size of these kind of systems.

Besides expanding the above-mentioned sample size, I also showed in this thesis the capability of e.g. ESPRESSO to probe the obliquity for uncovered regions of the parameter space. As mentioned previously, this is already achievable for small exo-Earths in systems such as Trappist-1. Personally I think it could be very interesting to expand the limits of the observations even further by e.g. discovering and characterising exomoons via the Rossiter-McLaughlin effect (see e.g. Triaud, 2018, for a short review of future capabilities) or to explore the obliquity between the planetary orbit and the planetary spin. The latter is the main reason for seasons on Earth, and might have similar impacts on an Earth-like world. If we would like to quantify the climate of a specific planet and it's capability to sustain life, this will certainly be an important factor. With the release of GAIA planetary data as well as the arrival of PLATO and the ongoing construction of 30 meter optical telescopes, I expect the coming decade to be even more exciting and plentiful than the preceding in terms of obliquity observations.

While this thesis has focused on spin-orbit measurements, looking outside of obliquity research will also be fruitful to explore planet formation in general and the past of hot Jupiters in particular. As summarised in Dawson and Johnson (2018) different studies might hold the key to reveal the origin of gas giants, especially if combined with spin-orbit examinations. In my opinion, the most promising of these would be to perform more elaborate eccentricity follow-up of giant planets via radial velocity studies or to further constrain observations of proto-planetary disks.

There is still a great deal to learn about planets beyond the Solar System: what is the history of these foreign worlds? Are they habitable? Do any contain life? In my opinion, the future looks bright for the research field of extra-solar

planets. With the introduction of new space and ground-based missions focused on exoplanets in the coming decades, our knowledge on these foreign worlds will only expand. With the ongoing hot Jupiter studies, spin-orbit measurements and related examinations of planetary characteristics, we are very close to answering one of the oldest questions in exoplanetary science; the origin of hot Jupiters.

Appendices

Tables of observations

Table A1: MASCARA-3 (Ch. 4): Radial velocities at times outside of transit for MASCARA-3 using the SONG telescope. We list the barycentric time of mid-exposure and the RVs corrected for barycentric motion. All spectra were taken with the iodine cell as reference. Though the individual uncertainties have some dependence on the flux level (being near 30 m sec^{-1} at the highest and 60 m sec^{-1} at the lowest flux level) the overall instrumental uncertainty ($\sigma_{\rm RV}$) is estimated to be $\sim$ 40 m sec^{-1}. To account for the possibility of underestimating this error, we introduce an additional jitter term during the fitting procedure (see Table 4.4).

Time (BJD)	RV+6,000 (m s^{-1})	Time (BJD)	RV+6,000 (m s^{-1})
2458223.357685	613.1	2458280.423224	17.1
2458224.382018	183.3	2458283.600292	812.6
2458225.434460	67.3	2458418.763646	161.4
2458233.607846	704.9	2458426.556824	222.3
2458234.418452	770.2	2458434.627715	639.1
2458235.720058	234.6	2458439.611331	713.9
2458236.641036	32.2	2458448.692687	285.5
2458237.678446	153.1	2458449.708606	658.2
2458238.692052	603.9	2458450.690659	709.9
2458241.674223	-70.7	2458453.742034	106.8
2458243.368995	265.3	2458454.745732	493.1
2458245.410918	805.6	2458586.621310	20.0
2458246.571993	240.1	2458594.703421	710.9
2458247.398019	-31.2	2458598.446201	150.2
2458248.368253	82.6	2458600.395783	819.7
2458249.365280	470.8	2458602.394577	19.7
2458250.368275	844.0	2458604.398027	462.9
2458250.681785	837.2	2458606.403578	680.6
2458251.366037	687.0	2458608.402462	-36.2
2458251.666389	485.7	2458610.402961	656.7
2458252.366480	192.9	2458612.656473	323.0
2458253.365122	120.4	2458614.640588	99.4
2458254.365100	237.8	2458616.679269	892.4
2458255.374490	605.4	2458621.434468	611.2
2458256.384282	796.1	2458623.623973	586.7
2458257.382395	330.0	2458625.668018	199.2
2458259.383303	18.0	2458627.634024	974.2
2458263.567251	154.9	2458629.638527	312.8
2458265.589542	291.4	2458631.621685	345.4
2458267.372280	829.5	2458633.654485	949.8
2458268.609046	306.4	2458638.605001	913.8
2458270.572919	5.0	2458643.571329	579.7
2458274.379165	192.8		

Table A2: MASCARA-3 (Ch. 4): Radial velocities during transit on the night of May 29, 2018 for MASCARA-3 using the SONG telescope. We list the barycentric time of mid-exposure and the RVs corrected for barycentric motion. All spectra were taken with the ThAr cell as reference, causing the uncertainties to be larger than the RVs reported in Table A1, in addition to a different RV offset. The instrumental uncertainty (σ_{RVRM}) is estimated to be 50 m sec^{-1}.

Time (BJD)	$\mathrm{RV_{RM}}$+15,200 (m s^{-1})
2458268.353392	-14.0
2458268.361322	67.0
2458268.368937	65.0
2458268.376572	91.0
2458268.384095	124.0
2458268.391748	179.0
2458268.399454	73.0
2458268.407431	111.0
2458268.415063	240.0
2458268.422695	213.0
2458268.430603	126.0
2458268.446077	145.0
2458268.453711	116.0
2458268.461345	14.0
2458268.468981	44.0
2458268.476690	-27.0
2458268.484558	-2.0
2458268.492292	-14.0
2458268.500027	-87.0
2458268.507691	-108.0
2458268.515674	-67.0
2458268.523373	-111.0
2458268.531075	-73.0
2458268.538705	-16.0

Table A3: K2-290 (Ch. 5): Radial velocities and related values for K2-290 using the HARPS, HARPS-N and FIES spectrographs. We list the barycentric time of mid-exposure, the RVs, the instrumental RV uncertainties (σ_{RV}), the bisector span (BIS) and the FWHM of the CCFs, the exposure times (t_{exp}), the signal-to-noise ratios (S/N), and the instrument used for a specific observation. **Notes.** *S/N is per pixel and is calculated at 5500 Å.

Time (BJD_{TDB})	RV-19700 (m s^{-1})	σ_{RV} (m s^{-1})	BIS (m s^{-1})	FWHM (km s^{-1})	t_{exp} (s)	S/N*	Instr.
2458172.894740	21.7	3.2	55.1	10.9581	1800	72.3	HARPS
2458175.890871	23.9	3.9	35.0	10.9632	1500	60.8	HARPS
2458191.878876	73.0	3.4	35.3	10.9514	2100	68.6	HARPS
2458193.866635	71.5	4.1	44.4	10.9822	1500	53.4	HARPS
2458194.862556	85.6	3.6	53.7	10.9684	1800	65.3	HARPS
2458197.846021	93.1	3.9	53.7	10.9733	1800	59.2	HARPS
2458220.814348	22.7	4.0	45.4	10.9481	2400	56.6	HARPS
2458221.728938	23.0	4.8	60.5	10.9637	1800	46.7	HARPS
2458222.818965	20.2	4.6	34.4	10.9358	1800	50.9	HARPS
2458249.764215	103.6	4.1	44.9	10.9486	2300	57.5	HARPS
2458250.805571	106.0	4.2	47.6	10.9872	2100	55.9	HARPS
2458324.611686	29.1	5.3	9.7	10.9769	2400	45.1	HARPS
2458325.576369	28.6	5.1	39.6	10.9385	2400	47.4	HARPS
2458329.488931	43.2	3.8	34.4	10.9725	2100	58.5	HARPS
2458330.491675	41.6	3.3	42.0	10.9761	2100	68.6	HARPS
2458359.508754	58.6	4.0	38.6	10.9721	2400	56.7	HARPS
2458169.785818	28.2	11.2	68.0	11.0293	1200	25.7	HARPS-N
2458202.702616	107.7	8.0	83.0	10.9708	3600	34.0	HARPS-N
2458219.700532	26.3	4.7	60.4	10.9347	2100	52.8	HARPS-N
2458220.703092	20.6	7.0	61.0	10.9395	2100	38.0	HARPS-N
2458221.698890	5.8	8.0	95.4	10.9209	2100	33.6	HARPS-N
2458314.421992	49.0	5.4	42.4	10.9777	1800	47.2	HARPS-N
2458251.583280	-36.5	15.3	46.8	16.8868	3600	32.2	FIES
2458253.621643	-34.5	8.8	34.6	16.7709	3000	54.5	FIES
2458258.606573	-55.3	7.0	44.4	16.9018	3600	62.7	FIES
2458259.540916	-61.2	15.0	11.5	16.8045	3600	31.2	FIES
2458260.606755	-77.0	11.7	34.1	16.8718	3600	48.5	FIES
2458261.593343	-77.9	10.0	21.5	16.8944	3600	49.2	FIES
2458279.486551	-81.2	8.3	96.9	16.8609	3600	59.0	FIES
2458280.504146	-81.6	10.3	28.3	16.8988	3600	49.5	FIES
2458289.458960	-45.3	8.2	48.9	16.8567	3600	61.1	FIES
2458290.453468	-50.4	8.4	32.1	16.8290	3600	59.9	FIES
2458313.447528	-89.0	7.1	34.7	16.8713	3600	58.3	FIES

Table A4: The Rossiter-McLaughlin measurements of K2-290c with HARPS-N@TNG.

Time (BJD)	RV-19,760 (m s^{-1})	σ_{RV} (m s^{-1})
2458653.461391	-25.3	5.6
2458599.734446	16.1	8.1
2458599.708427	-3.7	8.5
2458599.525665	-8.9	8.5
2458599.755443	-11.7	8.1
2458599.511429	-15.5	9.0
2458599.665613	3.5	8.1
2458599.680174	17.9	8.4
2458599.539358	-7.4	8.1
2458599.553687	-20.5	8.0
2458662.439687	-33.4	6.7
2458599.694954	20.6	8.3

Table A5: The Rossiter-McLaughlin measurements of K2-290c with HDS@SUBARU.

Time (BJD)	RV+12,000 (m s^{-1})	σ_{RV} (m s^{-1})
2458646.904564	5.9	7.4
2458646.915414	17.8	7.0
2458646.926504	16.5	7.1
2458647.750561	-7.2	6.3
2458647.761661	-34.5	6.3
2458647.773090	31.1	9.7
2458647.784190	9.1	6.7
2458647.795279	1.5	6.8
2458647.808349	-13.4	6.5
2458647.819449	-18.6	6.4
2458647.830548	-18.0	6.4
2458647.841638	-21.5	6.3
2458647.852737	-12.8	6.2
2458647.863827	-28.9	6.1
2458647.874926	-18.8	5.9
2458647.886016	-22.2	6.5
2458647.897115	-25.7	6.6
2458647.908215	-20.5	6.8
2458647.921004	-14.5	6.7
2458647.932104	-21.7	6.9
2458647.943204	2.6	6.9
2458647.954303	-11.2	6.9
2458647.967083	2.2	6.7
2458647.981662	-0.5	6.3
2458647.996231	15.1	6.7
2458648.009101	5.6	6.8
2458648.020200	16.7	7.4

Table A6: The Rossiter-McLaughlin measurements of K2-290b obtained with ESPRESSO@VLT. A time with a * indicates excluded data points due to bad weather.

Time (BJD)	RV-19,670 (m s^{-1})	σ_{RV} (m s^{-1})
2458685.496193	-2.6	1.9
2458685.507030	-2.4	1.9
2458685.517732	2.4	2.0
2458685.528853	-1.6	2.0
2458685.539639	2.8	2.6
2458685.550695	-0.1	2.6
2458685.561700	-2.0	2.6
2458685.572653	-5.1	2.1
2458685.583376	-3.5	2.1
2458685.594217	-1.8	2.1
2458685.605165	-3.5	2.4
2458685.621852	-3.9	1.8
2458685.635662	0.1	1.9
2458685.650111	2.3	2.3
2458685.664976*	-4.4	2.5
2458685.679009*	-6.1	2.2
2458685.701177*	-4.8	3.0
2458685.728771*	-5.7	2.1
2458685.739713*	-12.8	2.3

List of Figures

List of Tables

Bibliography

Akiyama, E., Y. Hasegawa, M. Hayashi, and S. Iguchi (2016, Feb). Planetary System Formation in the Protoplanetary Disk around HL Tauri. *The Astrophysical Journal 818*(2), 158.

Albrecht, S., S. Reffert, I. Snellen, A. Quirrenbach, and D. S. Mitchell (2007, Nov). The spin axes orbital alignment of both stars within the eclipsing binary system V1143 Cyg using the Rossiter-McLaughlin effect. *Astronomy & Astrophysics 474*(2), 565–573.

Albrecht, S., J. N. Winn, R. P. Butler, J. D. Crane, S. A. Shectman, I. B. Thompson, T. Hirano, and R. A. Wittenmyer (2012, Jan). A High Stellar Obliquity in the WASP-7 Exoplanetary System. *The Astrophysical Journal 744*(2), 189.

Albrecht, S., J. N. Winn, J. A. Johnson, R. P. Butler, J. D. Crane, S. A. Shectman, I. B. Thompson, N. Narita, B. Sato, T. Hirano, K. Enya, and D. Fischer (2011, Sep). Two Upper Limits on the Rossiter-Mclaughlin Effect, with Differing Implications: WASP-1 has a High Obliquity and WASP-2 is Indeterminate. *The Astrophysical Journal 738*(1), 50.

Albrecht, S., J. N. Winn, J. A. Johnson, A. W. Howard, G. W. Marcy, R. P. Butler, P. Arriagada, J. D. Crane, S. A. Shectman, I. B. Thompson, T. Hirano, G. Bakos, and J. D. Hartman (2012, Sep). Obliquities of Hot Jupiter Host Stars: Evidence for Tidal Interactions and Primordial Misalignments. *The Astrophysical Journal 757*(1), 18.

Albrecht, S., J. N. Winn, G. W. Marcy, A. W. Howard, H. Isaacson, and J. A. Johnson (2013, Jul). Low Stellar Obliquities in Compact Multiplanet Systems. *The Astrophysical Journal 771*(1), 11.

ALMA Partnership, C. L. Brogan, L. M. Pérez, T. R. Hunter, W. R. F. Dent, A. S. Hales, R. E. Hills, S. Corder, E. B. Fomalont, C. Vlahakis, Y. Asaki, D. Barkats, A. Hirota, J. A. Hodge, C. M. V. Impellizzeri, R. Kneissl, E. Liuzzo, R. Lucas, N. Marcelino, S. Matsushita, K. Nakanishi, N. Phillips, A. M. S. Richards, I. Toledo, R. Aladro, D. Broguiere, J. R. Cortes, P. C. Cortes, D. Espada, F. Galarza, D. Garcia-Appadoo, L. Guzman-Ramirez, E. M. Humphreys, T. Jung, S. Kameno, R. A. Laing, S. Leon, G. Marconi, A. Mignano, B. Nikolic, L. A. Nyman, M. Radiszcz, A. Remijan, J. A. Rodón, T. Sawada, S. Takahashi, R. P. J. Tilanus, B. Vila Vilaro, L. C. Watson, T. Wiklind, E. Akiyama, E. Chapillon, I. de Gregorio-Monsalvo, J. Di Francesco, F. Gueth, A. Kawamura, C. F. Lee, Q. Nguyen Luong, J. Mangum,

V. Pietu, P. Sanhueza, K. Saigo, S. Takakuwa, C. Ubach, T. van Kempen, A. Wootten, A. Castro-Carrizo, H. Francke, J. Gallardo, J. Garcia, S. Gonzalez, T. Hill, T. Kaminski, Y. Kurono, H. Y. Liu, C. Lopez, F. Morales, K. Plarre, G. Schieven, L. Testi, L. Videla, E. Villard, P. Andreani, J. E. Hibbard, and K. Tatematsu (2015, Jul). The 2014 ALMA Long Baseline Campaign: First Results from High Angular Resolution Observations toward the HL Tau Region. *The Astrophysical Journal Letters 808*(1), L3.

Andersen, M. F., F. Grundahl, J. Christensen-Dalsgaard, S. Frandsen, U. G. Jørgensen, H. Kjeldsen, P. Pallé, J. Skottfelt, A. N. Sørensen, and E. Weiss (2014, December). Hardware and software for a robotic network of telescopes - SONG. In *Revista Mexicana de Astronomia y Astrofisica Conference Series*, Volume 45 of *Revista Mexicana de Astronomia y Astrofisica Conference Series*, pp. 83–86.

Andersen, M. F., R. Handberg, E. Weiss, S. Frand sen, S. Simón-Díaz, F. Grundahl, and P. Pallé (2019, Apr). Conducting the SONG: The Robotic Nature and Efficiency of a Fully Automated Telescope. *The Publications of the Astronomical Society of the Pacific 131*(998), 045003.

Anderson, D. R., A. Collier Cameron, C. Hellier, M. Lendl, P. F. L. Maxted, D. Pollacco, D. Queloz, B. Smalley, A. M. S. Smith, I. Todd, A. H. M. J. Triaud, R. G. West, S. C. C. Barros, B. Enoch, M. Gillon, T. A. Lister, F. Pepe, D. Ségransan, R. A. Street, and S. Udry (2011, January). WASP-30b: A 61 M $_{Jup}$ Brown Dwarf Transiting a V = 12, F8 Star. *The Astrophysical Journal Letters 726*, L19.

Anderson, K. R., D. Lai, and B. Pu (2019, Aug). In-Situ Scattering of Warm Jupiters and Implications for Dynamical Histories. *arXiv e-prints*, arXiv:1908.04300.

Anglada-Escudé, G., P. J. Amado, J. Barnes, Z. M. Berdiñas, R. P. Butler, G. A. L. Coleman, I. de La Cueva, S. Dreizler, M. Endl, B. Giesers, S. V. Jeffers, J. S. Jenkins, H. R. A. Jones, M. Kiraga, M. Kürster, M. J. López-González, C. J. Marvin, N. Morales, J. Morin, R. P. Nelson, J. L. Ortiz, A. Ofir, S.-J. Paardekooper, A. Reiners, E. Rodríguez, C. Rodríguez-López, L. F. Sarmiento, J. P. Strachan, Y. Tsapras, M. Tuomi, and M. Zechmeister (2016, August). A terrestrial planet candidate in a temperate orbit around Proxima Centauri. *Nature 536*, 437–440.

Anglada-Escudé, G., P. Arriagada, S. S. Vogt, E. J. Rivera, R. P. Butler, J. D. Crane, S. A. Shectman, I. B. Thompson, D. Minniti, N. Haghighipour, B. D. Carter, C. G. Tinney, R. A. Wittenmyer, J. A. Bailey, S. J. O'Toole, H. R. A. Jones, and J. S. Jenkins (2012, May). A Planetary System around the nearby M Dwarf GJ 667C with At Least One Super-Earth in Its Habitable Zone. *The Astrophysical Journal Letters 751*, L16.

Bakos, G., R. W. Noyes, G. Kovács, K. Z. Stanek, D. D. Sasselov, and I. Domsa (2004, March). Wide-Field Millimagnitude Photometry with the HAT: A Tool for Extrasolar Planet Detection. *The Publications of the Astronomical Society of the Pacific 116*, 266–277.

Barge, P., A. Baglin, M. Auvergne, H. Rauer, A. Léger, J. Schneider, F. Pont, S. Aigrain, J.-M. Almenara, R. Alonso, M. Barbieri, P. Bordé, F. Bouchy, H. J. Deeg, D. La Reza, M. Deleuil, R. Dvorak, A. Erikson, M. Fridlund, M. Gillon, P. Gondoin, T. Guillot, A. Hatzes, G. Hebrard, L. Jorda, P. Kabath, H. Lammer, A. Llebaria, B. Loeillet, P. Magain, T. Mazeh, C. Moutou, M. Ollivier, M. Pätzold, D. Queloz, D. Rouan,

A. Shporer, and G. Wuchterl (2008, May). Transiting exoplanets from the CoRoT space mission. I. CoRoT-Exo-1b: a low-density short-period planet around a G0V star. *Astronomy & Astrophysics 482*, L17–L20.

Barnes, J. W. (2009, Nov). Transit Lightcurves of Extrasolar Planets Orbiting Rapidly Rotating Stars. *The Astrophysical Journal 705*(1), 683–692.

Bate, M. R., G. Lodato, and J. E. Pringle (2010, Jan). Chaotic star formation and the alignment of stellar rotation with disc and planetary orbital axes. *Monthly Notices of the Royal Astronomical Society 401*(3), 1505–1513.

Batygin, K. (2012, Nov). A primordial origin for misalignments between stellar spin axes and planetary orbits. *Nature 491*(7424), 418–420.

Batygin, K. and F. C. Adams (2013, Dec). Magnetic and Gravitational Disk-Star Interactions: An Interdependence of PMS Stellar Rotation Rates and Spin-Orbit Misalignments. *The Astrophysical Journal 778*(2), 169.

Batygin, K., P. H. Bodenheimer, and G. P. Laughlin (2016, Oct). In Situ Formation and Dynamical Evolution of Hot Jupiter Systems. *The Astrophysical Journal 829*(2), 114.

Beaugé, C. and D. Nesvorný (2012, Jun). Multiple-planet Scattering and the Origin of Hot Jupiters. *The Astrophysical Journal 751*(2), 119.

Blanco-Cuaresma, S., C. Soubiran, U. Heiter, and P. Jofré (2014, September). Determining stellar atmospheric parameters and chemical abundances of FGK stars with iSpec. *Astronomy & Astrophysics 569*, A111.

Bonomo, A. S., S. Desidera, S. Benatti, F. Borsa, S. Crespi, M. Damasso, A. F. Lanza, A. Sozzetti, G. Lodato, F. Marzari, C. Boccato, R. U. Claudi, R. Cosentino, E. Covino, R. Gratton, A. Maggio, G. Micela, E. Molinari, I. Pagano, G. Piotto, E. Poretti, R. Smareglia, L. Affer, K. Biazzo, A. Bignamini, M. Esposito, P. Giacobbe, G. Hébrard, L. Malavolta, J. Maldonado, L. Mancini, A. Martinez Fiorenzano, S. Masiero, V. Nascimbeni, M. Pedani, M. Rainer, and G. Scandariato (2017, June). The GAPS Programme with HARPS-N at TNG . XIV. Investigating giant planet migration history via improved eccentricity and mass determination for 231 transiting planets. *Astronomy & Astrophysics 602*, A107.

Borucki, W. J., D. Koch, G. Basri, N. Batalha, T. Brown, D. Caldwell, J. Caldwell, J. Christensen-Dalsgaard, W. D. Cochran, E. DeVore, E. W. Dunham, A. K. Dupree, T. N. Gautier, J. C. Geary, R. Gilliland, A. Gould, S. B. Howell, J. M. Jenkins, Y. Kondo, D. W. Latham, G. W. Marcy, S. Meibom, H. Kjeldsen, J. J. Lissauer, D. G. Monet, D. Morrison, D. Sasselov, J. Tarter, A. Boss, D. Brownlee, T. Owen, D. Buzasi, D. Charbonneau, L. Doyle, J. Fortney, E. B. Ford, M. J. Holman, S. Seager, J. H. Steffen, W. F. Welsh, J. Rowe, H. Anderson, L. Buchhave, D. Ciardi, L. Walkowicz, W. Sherry, E. Horch, H. Isaacson, M. E. Everett, D. Fischer, G. Torres, J. A. Johnson, M. Endl, P. MacQueen, S. T. Bryson, J. Dotson, M. Haas, J. Kolodziejczak, J. Van Cleve, H. Chandrasekaran, J. D. Twicken, E. V. Quintana, B. D. Clarke, C. Allen, J. Li, H. Wu, P. Tenenbaum, E. Verner, F. Bruhweiler, J. Barnes, and A. Prsa (2010, February). Kepler Planet-Detection Mission: Introduction and First Results. *Science 327*, 977.

Boss, A. P., G. Basri, S. S. Kumar, J. Liebert, E. L. Martín, B. Reipurth, and H. Zinnecker (2003, Jun). Nomenclature: Brown Dwarfs, Gas Giant Planets, and ? In E. Martín (Ed.), *Brown Dwarfs*, Volume 211 of *IAU Symposium*, pp. 529.

Bourrier, V. and G. Hébrard (2014, Sep). Detecting the spin-orbit misalignment of the super-Earth 55 Cancri e. *Astronomy & Astrophysics 569*, A65.

Bourrier, V., C. Lovis, H. Beust, D. Ehrenreich, G. W. Henry, N. Astudillo-Defru, R. Allart, X. Bonfils, D. Ségransan, X. Delfosse, H. M. Cegla, A. Wyttenbach, K. Heng, B. Lavie, and F. Pepe (2018, Jan). Orbital misalignment of the Neptune-mass exoplanet GJ 436b with the spin of its cool star. *Nature 553*(7689), 477–480.

Brinch, C., J. K. Jørgensen, M. R. Hogerheijde, R. P. Nelson, and O. Gressel (2016, Oct). Misaligned Disks in the Binary Protostar IRS 43. *The Astrophysical Journal Letters 830*(1), L16.

Brown, D. J. A., A. H. M. J. Triaud, A. P. Doyle, M. Gillon, M. Lendl, D. R. Anderson, A. Collier Cameron, G. Hébrard, C. Hellier, C. Lovis, P. F. L. Maxted, F. Pepe, D. Pollacco, D. Queloz, and B. Smalley (2017, Jan). Rossiter-McLaughlin models and their effect on estimates of stellar rotation, illustrated using six WASP systems. *Monthly Notices of the Royal Astronomical Society 464*(1), 810–839.

Brown, T. M., D. W. Latham, M. E. Everett, and G. A. Esquerdo (2011, October). Kepler Input Catalog: Photometric Calibration and Stellar Classification. *The Astronomical Journal 142*, 112.

Bruno, G. (1584). *On the Infinite Universe and Worlds*.

Campante, T. L., T. Barclay, J. J. Swift, D. Huber, V. Z. Adibekyan, W. Cochran, C. J. Burke, H. Isaacson, E. V. Quintana, G. R. Davies, V. Silva Aguirre, D. Ragozzine, R. Riddle, C. Baranec, S. Basu, W. J. Chaplin, J. Christensen-Dalsgaard, T. S. Metcalfe, T. R. Bedding, R. Handberg, D. Stello, J. M. Brewer, S. Hekker, C. Karoff, R. Kolbl, N. M. Law, M. Lundkvist, A. Miglio, J. F. Rowe, N. C. Santos, C. Van Laerhoven, T. Arentoft, Y. P. Elsworth, D. A. Fischer, S. D. Kawaler, H. Kjeldsen, M. N. Lund, G. W. Marcy, S. G. Sousa, A. Sozzetti, and T. R. White (2015, February). An Ancient Extrasolar System with Five Sub-Earth-size Planets. *The Astrophysical Journal 799*, 170.

Carrera, D., S. R. Raymond, and M. B. Davies (2019, Mar). Planet-planet scattering as the source of the highest eccentricity exoplanets. *arXiv e-prints*, arXiv:1903.02564.

Casagrande, L. and D. A. VandenBerg (2014, October). Synthetic stellar photometry - I. General considerations and new transformations for broad-band systems. *Monthly Notices of the Royal Astronomical Society 444*, 392–419.

Casagrande, L. and D. A. VandenBerg (2018, April). Synthetic Stellar Photometry - II. Testing the bolometric flux scale and tables of bolometric corrections for the Hipparcos/Tycho, Pan-STARRS1, SkyMapper, and JWST systems. *Monthly Notices of the Royal Astronomical Society 475*, 5023–5040.

Chabrier, G., A. Johansen, M. Janson, and R. Rafikov (2014, Jan). Giant Planet and Brown Dwarf Formation. In H. Beuther, R. S. Klessen, C. P. Dullemond, and T. Henning (Eds.), *Protostars and Planets VI*, pp. 619.

Claret, A. (2000, Nov). A new non-linear limb-darkening law for LTE stellar atmosphere models. Calculations for -5.0 <= log[M/H] <= +1, 2000 K <= T_{eff} <= 50000 K at several surface gravities. *Astronomy & Astrophysics 363*, 1081–1190.

Claret, A. and S. Bloemen (2011, May). Gravity and limb-darkening coefficients for the Kepler, CoRoT, Spitzer, uvby, UBVRIJHK, and Sloan photometric systems. *Astronomy & Astrophysics 529*, A75.

Cloutier, R. and A. H. M. J. Triaud (2016, Nov). Prospects for detecting the Rossiter-McLaughlin effect of Earth-like planets: the test case of TRAPPIST-1b and c. *Monthly Notices of the Royal Astronomical Society 462*(4), 4018–4027.

Coelho, P., B. Barbuy, J. Meléndez, R. P. Schiavon, and B. V. Castilho (2005, Nov). A library of high resolution synthetic stellar spectra from 300 nm to 1.8 μm with solar and α-enhanced composition. *Astronomy & Astrophysics 443*(2), 735–746.

Collier Cameron, A., V. A. Bruce, G. R. M. Miller, A. H. M. J. Triaud, and D. Queloz (2010, Mar). Line-profile tomography of exoplanet transits - I. The Doppler shadow of HD 189733b. *Monthly Notices of the Royal Astronomical Society 403*(1), 151–158.

Cosentino, R., C. Lovis, F. Pepe, A. Collier Cameron, D. W. Latham, E. Molinari, S. Udry, N. Bezawada, M. Black, A. Born, N. Buchschacher, D. Charbonneau, P. Figueira, M. Fleury, A. Galli, A. Gallie, X. Gao, A. Ghedina, C. Gonzalez, M. Gonzalez, J. Guerra, D. Henry, K. Horne, I. Hughes, D. Kelly, M. Lodi, D. Lunney, C. Maire, M. Mayor, G. Micela, M. P. Ordway, J. Peacock, D. Phillips, G. Piotto, D. Pollacco, D. Queloz, K. Rice, C. Riverol, L. Riverol, J. San Juan, D. Sasselov, D. Segransan, A. Sozzetti, D. Sosnowska, B. Stobie, A. Szentgyorgyi, A. Vick, and L. Weber (2012, September). Harps-N: the new planet hunter at TNG. In *Ground-based and Airborne Instrumentation for Astronomy IV*, Volume 8446 of *Proceedings of the SPIE*, pp. 84461V.

Cutri, R. M., M. F. Skrutskie, S. van Dyk, C. A. Beichman, J. M. Carpenter, T. Chester, L. Cambresy, T. Evans, J. Fowler, J. Gizis, E. Howard, J. Huchra, T. Jarrett, E. L. Kopan, J. D. Kirkpatrick, R. M. Light, K. A. Marsh, H. McCallon, S. Schneider, R. Stiening, M. Sykes, M. Weinberg, W. A. Wheaton, S. Wheelock, and N. Zacarias (2003, June). VizieR Online Data Catalog: 2MASS All-Sky Catalog of Point Sources (Cutri+ 2003). *VizieR Online Data Catalog 2246*.

Dai, F. and J. N. Winn (2017, May). The Oblique Orbit of WASP-107b from K2 Photometry. *The Astronomical Journal 153*(5), 205.

Dai, F., J. N. Winn, D. Gandolfi, S. X. Wang, J. K. Teske, J. Burt, S. Albrecht, O. Barragán, W. D. Cochran, M. Endl, M. Fridlund, A. P. Hatzes, T. Hirano, L. A. Hirsch, M. C. Johnson, A. B. Justesen, J. Livingston, C. M. Persson, J. Prieto-Arranz, A. Vanderburg, R. Alonso, G. Antoniciello, P. Arriagada, R. P. Butler, J. Cabrera, J. D. Crane, F. Cusano, S. Csizmadia, H. Deeg, S. B. Dieterich, P. Eigmüller, A. Erikson, M. E. Everett, A. Fukui, S. Grziwa, E. W. Guenther, G. W. Henry, S. B. Howell, J. A. Johnson, J. Korth, M. Kuzuhara, N. Narita, D. Nespral, G. Nowak, E. Palle, M. Pätzold, H. Rauer, P. Montañés Rodríguez, S. A. Shectman, A. M. S. Smith, I. B. Thompson, V. Van Eylen, M. W. Williamson, and R. A. Wittenmyer (2017, December). The Discovery and Mass Measurement of a New Ultra-short-period Planet: K2-131b. *The Astronomical Journal 154*, 226.

Dalal, S., G. Hébrard, A. Lecavelier des Étangs, A. C. Petit, V. Bourrier, J. Laskar, P.-C. König, and A. C. M. Correia (2019, Jun). Nearly Polar orbit of the sub-Neptune HD3167 c: Constraints on a multi-planet system dynamical history. *arXiv e-prints*, arXiv:1906.11013.

Dawson, R. I. (2014, Aug). On the Tidal Origin of Hot Jupiter Stellar Obliquity Trends. *The Astrophysical Journal Letters 790*(2), L31.

Dawson, R. I. and J. A. Johnson (2018, Sep). Origins of Hot Jupiters. *Annual Review of Astronomy and Astrophysics 56*, 175–221.

Dawson, R. I., J. A. Johnson, D. C. Fabrycky, D. Foreman-Mackey, R. A. Murray-Clay, L. A. Buchhave, P. A. Cargile, K. I. Clubb, B. J. Fulton, L. Hebb, A. W. Howard, D. Huber, A. Shporer, and J. A. Valenti (2014, August). Large Eccentricity, Low Mutual Inclination: The Three-dimensional Architecture of a Hierarchical System of Giant Planets. *The Astrophysical Journal 791*, 89.

Dawson, R. I. and R. A. Murray-Clay (2013, April). Giant Planets Orbiting Metal-rich Stars Show Signatures of Planet-Planet Interactions. *The Astrophysical Journal Letters 767*, L24.

de Pater, I. and J. J. Lissauer (2015). *Planetary Sciences*.

Demory, B.-O. and S. Seager (2011, November). Lack of Inflated Radii for Kepler Giant Planet Candidates Receiving Modest Stellar Irradiation. *The Astrophysical Journal Supplement Series 197*, 12.

Dong, S., B. Katz, and A. Socrates (2014, Jan). Warm Jupiters Need Close "Friends" for High-eccentricity Migration—a Stringent Upper Limit on the Perturber's Separation. *The Astrophysical Journal 781*(1), L5.

Dorval, P., G. J. J. Talens, G. P. P. L. Otten, R. Brahm, A. Jordán, L. Vanzi, A. Zapata, T. Henry, L. Paredes, W. C. Jao, H. James, R. Hinojosa, G. A. Bakos, Z. Csubry, W. Bhatti, V. Suc, D. Osip, E. E. Mamajek, S. N. Mellon, A. Wyttenbach, R. Stuik, M. Kenworthy, J. Bailey, M. Ireland, S. Crawford, B. Lomberg, R. Kuhn, and I. Snellen (2019, April). MASCARA-4 b/bRing-1b - A retrograde hot Jupiter around the bright A3V star HD 85628. *arXiv e-prints*.

Dressing, C. D. and D. Charbonneau (2013, Apr). The Occurrence Rate of Small Planets around Small Stars. *The Astrophysical Journal 767*(1), 95.

Duffell, P. C., Z. Haiman, A. I. MacFadyen, D. J. D'Orazio, and B. D. Farris (2014, Sep). The Migration of Gap-opening Planets is Not Locked to Viscous Disk Evolution. *The Astrophysical Journal Letters 792*(1), L10.

Eastman, J., B. S. Gaudi, and E. Agol (2013, Jan). EXOFAST: A Fast Exoplanetary Fitting Suite in IDL. *The Publications of the Astronomical Society of the Pacific 125*(923), 83.

Fabrycky, D. C. and J. N. Winn (2009, May). Exoplanetary Spin-Orbit Alignment: Results from the Ensemble of Rossiter-McLaughlin Observations. *The Astrophysical Journal 696*(2), 1230–1240.

Feroz, F. and M. P. Hobson (2014, February). Bayesian analysis of radial velocity data of GJ667C with correlated noise: evidence for only two planets. *Monthly Notices of the Royal Astronomical Society 437*, 3540–3549.

Ford, E. B. (2006, May). Improving the Efficiency of Markov Chain Monte Carlo for Analyzing the Orbits of Extrasolar Planets. *The Astrophysical Journal 642*, 505–522.

Ford, E. B., M. Havlickova, and F. A. Rasio (2001, Apr). Dynamical Instabilities in Extrasolar Planetary Systems Containing Two Giant Planets. *Icarus 150*(2), 303–313.

Foreman-Mackey, D., D. W. Hogg, D. Lang, and J. Goodman (2013, Mar). emcee: The MCMC Hammer. *The Publications of the Astronomical Society of the Pacific 125*(925), 306.

Fortney, J. J., M. S. Marley, and J. W. Barnes (2007, April). Planetary Radii across Five Orders of Magnitude in Mass and Stellar Insolation: Application to Transits. *The Astrophysical Journal 659*, 1661–1672.

Freudling, W., M. Romaniello, D. M. Bramich, P. Ballester, V. Forchi, C. E. García-Dabló, S. Moehler, and M. J. Neeser (2013, November). Automated data reduction workflows for astronomy. The ESO Reflex environment. *Astronomy & Astrophysics 559*, A96.

Fulton, B. J., E. A. Petigura, A. W. Howard, H. Isaacson, G. W. Marcy, P. A. Cargile, L. Hebb, L. M. Weiss, J. A. Johnson, T. D. Morton, E. Sinukoff, I. J. M. Crossfield, and L. A. Hirsch (2017, September). The California-Kepler Survey. III. A Gap in the Radius Distribution of Small Planets. *The Astronomical Journal 154*, 109.

Gaia Collaboration (2018, Aug). Gaia Data Release 2. Summary of the contents and survey properties. *Astronomy & Astrophysics 616*, A1.

Gandolfi, D., H. Parviainen, M. Fridlund, A. P. Hatzes, H. J. Deeg, A. Frasca, A. F. Lanza, P. G. Prada Moroni, E. Tognelli, A. McQuillan, S. Aigrain, R. Alonso, V. Antoci, J. Cabrera, L. Carone, S. Csizmadia, A. A. Djupvik, E. W. Guenther, J. Jessen-Hansen, A. Ofir, and J. Telting (2013, September). Kepler-77b: a very low albedo, Saturn-mass transiting planet around a metal-rich solar-like star. *Astronomy & Astrophysics 557*, A74.

Gillon, M., E. Jehin, S. M. Lederer, L. Delrez, J. de Wit, A. Burdanov, V. Van Grootel, A. J. Burgasser, A. H. M. J. Triaud, C. Opitom, B.-O. Demory, D. K. Sahu, D. Bardalez Gagliuffi, P. Magain, and D. Queloz (2016, May). Temperate Earth-sized planets transiting a nearby ultracool dwarf star. *Nature 533*, 221–224.

Gillon, M., A. H. M. J. Triaud, B.-O. Demory, E. Jehin, E. Agol, K. M. Deck, S. M. Lederer, J. de Wit, A. Burdanov, J. G. Ingalls, E. Bolmont, J. Leconte, S. N. Raymond, F. Selsis, M. Turbet, K. Barkaoui, A. Burgasser, M. R. Burleigh, S. J. Carey, A. Chaushev, C. M. Copperwheat, L. Delrez, C. S. Fernand es, D. L. Holdsworth, E. J. Kotze, V. Van Grootel, Y. Almleaky, Z. Benkhaldoun, P. Magain, and D. Queloz (2017, Feb). Seven temperate terrestrial planets around the nearby ultracool dwarf star TRAPPIST-1. *Nature 542*(7642), 456–460.

Goldreich, P. and S. Tremaine (1980, Oct). Disk-satellite interactions. *The Astrophysical Journal 241*, 425–441.

Gratia, P. and D. Fabrycky (2017, Jan). Outer-planet scattering can gently tilt an inner planetary system. *Monthly Notices of the Royal Astronomical Society 464*(2), 1709–1717.

Gray, D. F. (1984, Jun). Measurements of rotation and turbulence in F, G and K dwarfs. *The Astrophysical Journal 281*, 719–722.

Gray, D. F. (2005). *The Observation and Analysis of Stellar Photospheres*. Cambridge University Press.

Green, G. M., E. F. Schlafly, D. Finkbeiner, H.-W. Rix, N. Martin, W. Burgett, P. W. Draper, H. Flewelling, K. Hodapp, N. Kaiser, R.-P. Kudritzki, E. A. Magnier, N. Metcalfe, J. L. Tonry, R. Wainscoat, and C. Waters (2018, July). Galactic reddening in 3D from stellar photometry - an improved map. *Monthly Notices of the Royal Astronomical Society 478*, 651–666.

Grundahl, F., M. Fredslund Andersen, J. Christensen-Dalsgaard, V. Antoci, H. Kjeldsen, R. Handberg, G. Houdek, T. R. Bedding, P. L. Pallé, J. Jessen-Hansen, V. Silva Aguirre, T. R. White, S. Frandsen, S. Albrecht, M. I. Andersen, T. Arentoft, K. Brogaard, W. J. Chaplin, K. Harpsøe, U. G. Jørgensen, I. Karovicova, C. Karoff, P. Kjærgaard Rasmussen, M. N. Lund, M. Sloth Lundkvist, J. Skottfelt, A. Norup Sørensen, R. Tronsgaard, and E. Weiss (2017, February). First Results from the Hertzsprung SONG Telescope: Asteroseismology of the G5 Subgiant Star μ Herculis. *The Astrophysical Journal 836*, 142.

Gustafsson, B., B. Edvardsson, K. Eriksson, U. G. Jørgensen, Å. Nordlund, and B. Plez (2008, August). A grid of MARCS model atmospheres for late-type stars. I. Methods and general properties. *Astronomy & Astrophysics 486*, 951–970.

Hamers, A. S. (2017, April). On the formation of hot and warm Jupiters via secular high-eccentricity migration in stellar triples. *Monthly Notices of the Royal Astronomical Society 466*, 4107–4120.

Hasegawa, Y. and S. Ida (2013, Sep). Do Giant Planets Survive Type II Migration? *The Astrophysical Journal 774*(2), 146.

Hayano, Y., H. Takami, S. Oya, M. Hattori, Y. Saito, M. Watanabe, O. Guyon, Y. Minowa, S. E. Egner, M. Ito, V. Garrel, S. Colley, T. Golota, and M. Iye (2010, July). Commissioning status of Subaru laser guide star adaptive optics system. In *Adaptive Optics Systems II*, Volume 7736 of *Proceedings of the SPIE*, pp. 77360N.

Heller, R. (2019, Aug). Formation of hot Jupiters through disk migration and evolving stellar tides. *Astronomy & Astrophysics 628*, A42.

Hidalgo, S. L., A. Pietrinferni, S. Cassisi, M. Salaris, A. Mucciarelli, A. Savino, A. Aparicio, V. Silva Aguirre, and K. Verma (2018, April). The Updated BaSTI Stellar Evolution Models and Isochrones. I. Solar-scaled Calculations. *The Astrophysical Journal 856*, 125.

Hirano, T. (2014). *Measurement of Spin-Orbit Angles for Transiting Systems: Toward an Understanding of the Migration History of Planets.*

Hirano, T., A. Fukui, A. W. Mann, R. Sanchis-Ojeda, E. Gaidos, N. Narita, F. Dai, V. Van Eylen, C.-H. Lee, H. Onozato, T. Ryu, N. Kusakabe, A. Ito, M. Kuzuhara, M. Onitsuka, M. Tatsuuma, G. Nowak, E. Pallè, I. Ribas, M. Tamura, and L. Yu (2016, March). The K2-ESPRINT Project III: A Close-in Super-Earth around a Metal-rich Mid-M Dwarf. *The Astrophysical Journal 820*, 41.

Hirano, T., G. Nowak, M. Kuzuhara, E. Palle, F. Dai, L. Yu, V. Van Eylen, Y. Takeda, T. D. Brandt, N. Narita, S. Velasco, J. Prieto Arranz, R. Sanchis-Ojeda, J. N. Winn, T. Kudo, N. Kusakabe, A. Fukui, B. Sato, S. Albrecht, I. Ribas, T. Ryu, and M. Tamura (2016, July). The K2-ESPRINT Project IV. A Hot Jupiter in a Prograde Orbit with a Possible Stellar Companion. *The Astrophysical Journal 825*, 53.

Hirano, T., Y. Suto, A. Taruya, N. Narita, B. Sato, J. A. Johnson, and J. N. Winn (2010, Jan). Analytic Description of the Rossiter-Mclaughlin Effect for Transiting Exoplanets: Cross-Correlation Method and Comparison with Simulated Data. *The Astrophysical Journal 709*(1), 458–469.

Hirano, T., Y. Suto, J. N. Winn, A. Taruya, N. Narita, S. Albrecht, and B. Sato (2011, Dec). Improved Modeling of the Rossiter-McLaughlin Effect for Transiting Exoplanets. *The Astrophysical Journal 742*(2), 69.

Hjorth, M., S. Albrecht, G. J. J. Talens, A. B. Justesen, G. P. P. L. Otten, V. Antoci, P. Dorval, E. Foxell, M. Fredslund Andersen, F. Grundahl, F. Murgas, E. Palle, R. Stuik, I. A. G. Snellen, and V. Van Eylen (2019, Jun). MASCARA-3b: A hot Jupiter transiting a bright F7 star in an aligned orbit. *arXiv e-prints*, arXiv:1906.05254.

Hjorth, M., A. B. Justesen, T. Hirano, S. Albrecht, D. Gandolfi, F. Dai, R. Alonso, O. Barragán, M. Esposito, M. Kuzuhara, K. W. F. Lam, J. H. Livingston, P. Montanes-Rodriguez, N. Narita, G. Nowak, J. Prieto-Arranz, S. Redfield, F. Rodler, V. Van Eylen, J. N. Winn, G. Antoniciello, J. Cabrera, W. D. Cochran, S. Csizmadia, J. de Leon, H. Deeg, P. Eigmüller, M. Endl, A. Erikson, M. Fridlund, S. Grziwa, E. Guenther, A. P. Hatzes, P. Heeren, D. Hidalgo, J. Korth, R. Luque, D. Nespral, E. Palle, M. Pätzold, C. M. Persson, H. Rauer, A. M. S. Smith, and T. Trifonov (2019, Apr). K2-290: a warm Jupiter and a mini-Neptune in a triple-star system. *Monthly Notices of the Royal Astronomical Society 484*(3), 3522–3536.

Høg, E., C. Fabricius, V. V. Makarov, S. Urban, T. Corbin, G. Wycoff, U. Bastian, P. Schwekendiek, and A. Wicenec (2000, March). The Tycho-2 catalogue of the 2.5 million brightest stars. *Astronomy & Astrophysics 355*, L27–L30.

Howell, S. B., C. Sobeck, M. Haas, M. Still, T. Barclay, F. Mullally, J. Troeltzsch, S. Aigrain, S. T. Bryson, D. Caldwell, W. J. Chaplin, W. D. Cochran, D. Huber, G. W. Marcy, A. Miglio, J. R. Najita, M. Smith, J. D. Twicken, and J. J. Fortney (2014, April). The K2 Mission: Characterization and Early Results. *The Publications of the Astronomical Society of the Pacific 126*, 398.

Huang, C., Y. Wu, and A. H. M. J. Triaud (2016, Jul). Warm Jupiters Are Less Lonely than Hot Jupiters: Close Neighbors. *The Astrophysical Journal 825*(2), 98.

Huber, D., J. A. Carter, M. Barbieri, A. Miglio, K. M. Deck, D. C. Fabrycky, B. T. Montet, L. A. Buchhave, W. J. Chaplin, S. Hekker, J. Montalbán, R. Sanchis-Ojeda, S. Basu, T. R. Bedding, T. L. Campante, J. Christensen-Dalsgaard, Y. P. Elsworth, D. Stello, T. Arentoft, E. B. Ford, R. L. Gilliland , R. Handberg, A. W. Howard, H. Isaacson, J. A. Johnson, C. Karoff, S. D. Kawaler, H. Kjeldsen, D. W. Latham, M. N. Lund, M. Lundkvist, G. W. Marcy, T. S. Metcalfe, V. Silva Aguirre, and J. N. Winn (2013, Oct). Stellar Spin-Orbit Misalignment in a Multiplanet System. *Science 342*(6156), 331–334.

Husser, T. O., S. Wende-von Berg, S. Dreizler, D. Homeier, A. Reiners, T. Barman, and P. H. Hauschildt (2013, May). A new extensive library of PHOENIX stellar atmospheres and synthetic spectra. *Astronomy & Astrophysics 553*, A6.

Jacob, W. S. (1855, June). On certain Anomalies presented by the Binary Star 70 Ophiuchi. *Monthly Notices of the Royal Astronomical Society 15*, 228.

Jensen, E. L. N. and R. Akeson (2014, Jul). Misaligned protoplanetary disks in a young binary star system. *Nature 511*(7511), 567–569.

Johnson, M., G. Zhou, B. C. Addison, D. R. Ciardi, D. Dragomir, Y. Hasegawa, E. J. Lee, S. Wang, and L. Weiss (2019, May). Tracing the Origins and Evolution of Small Planets using Their Orbital Obliquities. *Bulletin of the AAS 51*(3), 258.

Johnson, M. C., W. D. Cochran, S. Albrecht, S. E. Dodson-Robinson, J. N. Winn, and K. Gullikson (2014, Jul). A Misaligned Prograde Orbit for Kepler-13 Ab via Doppler Tomography. *The Astrophysical Journal 790*(1), 30.

Johnson, M. C., F. Dai, A. B. Justesen, D. Gandolfi, A. P. Hatzes, G. Nowak, M. Endl, W. D. Cochran, D. Hidalgo, N. Watanabe, H. Parviainen, T. Hirano, S. Villanueva, J. Prieto-Arranz, N. Narita, E. Palle, E. W. Guenther, O. Barragán, T. Trifonov, P. Niraula, P. J. MacQueen, J. Cabrera, S. Csizmadia, P. Eigmüller, S. Grziwa, J. Korth, M. Pätzold, A. M. S. Smith, S. Albrecht, R. Alonso, H. Deeg, A. Erikson, M. Esposito, M. Fridlund, A. Fukui, N. Kusakabe, M. Kuzuhara, J. Livingston, P. Montañes Rodriguez, D. Nespral, C. M. Persson, T. Purismo, S. Raimundo, H. Rauer, I. Ribas, M. Tamura, V. Van Eylen, and J. N. Winn (2018, November). K2-260 b: a hot Jupiter transiting an F star, and K2-261 b: a warm Saturn around a bright G star. *Monthly Notices of the Royal Astronomical Society 481*, 596–612.

Kley, W. and R. P. Nelson (2012, Sep). Planet-Disk Interaction and Orbital Evolution. *Annual Review of Astronomy and Astrophysics 50*, 211–249.

Kobayashi, N., A. T. Tokunaga, H. Terada, M. Goto, M. Weber, R. Potter, P. M. Onaka, G. K. Ching, T. T. Young, K. Fletcher, D. Neil, L. Robertson, D. Cook, M. Imanishi, and D. W. Warren (2000, August). IRCS: infrared camera and spectrograph for the Subaru Telescope. In M. Iye and A. F. Moorwood (Eds.), *Optical and IR Telescope Instrumentation and Detectors*, Volume 4008 of *Proceedings of the SPIE*, pp. 1056–1066.

Kotani, T., M. Tamura, J. Nishikawa, A. Ueda, M. Kuzuhara, M. Omiya, J. Hashimoto, M. Ishizuka, T. Hirano, H. Suto, T. Kurokawa, T. Kokubo, T. Mori, Y. Tanaka, K. Kashiwagi, M. Konishi, T. Kudo, B. Sato, S. Jacobson, K. W. Hodapp, D. B. Hall, W. Aoki, T. Usuda, S. Nishiyama, T. Nakajima, Y. Ikeda, T. Yamamuro, J.-I. Morino, H. Baba, K. Hosokawa, H. Ishikawa, N. Narita, E. Kokubo, Y. Hayano, H. Izumiura, E. Kambe, N. Kusakabe, J. Kwon, M. Ikoma, Y. Hori, H. Genda, A. Fukui, Y. Fujii, H. Kawahara, G. Olivier, N. Jovanovic, H. Harakawa, M. Hayashi, M. Hidai, M. Machida, T. Matsuo, T. Nagata, M. Ogihara, H. Takami, N. Takato, H. Terada, and D. Oh (2018, Jul). The infrared Doppler (IRD) instrument for the Subaru telescope: instrument description and commissioning results. In *Proceedings of the SPIE*, Volume 10702 of *Society of Photo-Optical Instrumentation Engineers (SPIE) Conference Series*, pp. 1070211.

Kovács, G., S. Zucker, and T. Mazeh (2002, August). A box-fitting algorithm in the search for periodic transits. *Astronomy & Astrophysics 391*, 369–377.

Kozai, Y. (1962, Nov). Secular perturbations of asteroids with high inclination and eccentricity. *The Astronomical Journal 67*, 591.

Kreidberg, L. (2015, November). batman: BAsic Transit Model cAlculatioN in Python. *The Publications of the Astronomical Society of the Pacific 127*, 1161.

Kuerster, M., J. H. M. M. Schmitt, G. Cutispoto, and K. Dennerl (1997, April). ROSAT and AB Doradus: the first five years. *Astronomy & Astrophysics 320*, 831–839.

Kurucz, R. L. (1993). *SYNTHE spectrum synthesis programs and line data.*

Lai, D. (2012, Jun). Tidal dissipation in planet-hosting stars: damping of spin-orbit misalignment and survival of hot Jupiters. *Monthly Notices of the Royal Astronomical Society 423*(1), 486–492.

Lai, D. (2014, Jun). Star-disc-binary interactions in protoplanetary disc systems and primordial spin-orbit misalignments. *Monthly Notices of the Royal Astronomical Society 440*(4), 3532–3544.

Lai, D., K. R. Anderson, and B. Pu (2018, Apr). How do external companions affect spin-orbit misalignment of hot Jupiters? *Monthly Notices of the Royal Astronomical Society 475*(4), 5231–5236.

Laughlin, G., G. W. Marcy, S. S. Vogt, D. A. Fischer, and R. P. Butler (2005, August). On the Eccentricity of HD 209458b. *The Astrophysical Journal Letters 629*, L121–L124.

Lin, D. N. C., P. Bodenheimer, and D. C. Richardson (1996, Apr). Orbital migration of the planetary companion of 51 Pegasi to its present location. *Nature 380*(6575), 606–607.

Lin, D. N. C. and J. Papaloizou (1986, Oct). On the Tidal Interaction between Protoplanets and the Protoplanetary Disk. III. Orbital Migration of Protoplanets. *The Astrophysical Journal 309*, 846.

Livingston, J. H., M. Endl, F. Dai, W. D. Cochran, O. Barragan, D. Gandolfi, T. Hirano, S. Grziwa, A. M. S. Smith, S. Albrecht, J. Cabrera, S. Csizmadia, J. P. de Leon, H. Deeg, P. Eigmüller, A. Erikson, M. Everett, M. Fridlund, A. Fukui, E. W. Guenther, A. P. Hatzes, S. Howell, J. Korth, N. Narita, D. Nespral, G. Nowak, E. Palle, M. Pätzold, C. M. Persson, J. Prieto-Arranz, H. Rauer, M. Tamura, V. Van Eylen, and J. N. Winn (2018, August). 44 Validated Planets from K2 Campaign 10. *The Astronomical Journal 156*, 78.

López-Morales, M., A. H. M. J. Triaud, F. Rodler, X. Dumusque, L. A. Buchhave, A. Harutyunyan, S. Hoyer, R. Alonso, M. Gillon, N. A. Kaib, D. W. Latham, C. Lovis, F. Pepe, D. Queloz, S. N. Raymond, D. Ségransan, I. P. Waldmann, and S. Udry (2014, Sep). Rossiter-McLaughlin Observations of 55 Cnc e. *The Astrophysical Journal Letters 792*(2), L31.

Lundkvist, M. S., H. Kjeldsen, S. Albrecht, G. R. Davies, S. Basu, D. Huber, A. B. Justesen, C. Karoff, V. Silva Aguirre, V. van Eylen, C. Vang, T. Arentoft, T. Barclay, T. R. Bedding, T. L. Campante, W. J. Chaplin, J. Christensen-Dalsgaard, Y. P. Elsworth, R. L. Gilliland, R. Handberg, S. Hekker, S. D. Kawaler, M. N. Lund, T. S. Metcalfe, A. Miglio, J. F. Rowe, D. Stello, B. Tingley, and T. R. White (2016, April). Hot super-Earths stripped by their host stars. *Nature Communications 7*, 11201.

Luri, X., A. G. A. Brown, L. M. Sarro, F. Arenou, C. A. L. Bailer-Jones, A. Castro-Ginard, J. de Bruijne, T. Prusti, C. Babusiaux, and H. E. Delgado (2018, Aug). Gaia Data Release 2. Using Gaia parallaxes. *Astronomy & Astrophysics 616*, A9.

Mandel, K. and E. Agol (2002, December). Analytic Light Curves for Planetary Transit Searches. *The Astrophysical Journal Letters 580*, L171–L175.

Marshall, D. J., A. C. Robin, C. Reylé, M. Schultheis, and S. Picaud (2006, July). Modelling the Galactic interstellar extinction distribution in three dimensions. *Astronomy & Astrophysics 453*, 635–651.

Masset, F. S. and J. C. B. Papaloizou (2003, May). Runaway Migration and the Formation of Hot Jupiters. *The Astrophysical Journal 588*(1), 494–508.

Mayor, M., F. Pepe, D. Queloz, F. Bouchy, G. Rupprecht, G. Lo Curto, G. Avila, W. Benz, J.-L. Bertaux, X. Bonfils, T. Dall, H. Dekker, B. Delabre, W. Eckert, M. Fleury, A. Gilliotte, D. Gojak, J. C. Guzman, D. Kohler, J.-L. Lizon, A. Longinotti, C. Lovis, D. Megevand, L. Pasquini, J. Reyes, J.-P. Sivan, D. Sosnowska, R. Soto, S. Udry, A. van Kesteren, L. Weber, and U. Weilenmann (2003, December). Setting New Standards with HARPS. *The Messenger 114*, 20–24.

Mayor, M. and D. Queloz (1995, Nov). A Jupiter-mass companion to a solar-type star. *Nature 378*(6555), 355–359.

Mazeh, T., H. B. Perets, A. McQuillan, and E. S. Goldstein (2015, Mar). Photometric Amplitude Distribution of Stellar Rotation of KOIs—Indication for Spin-Orbit Alignment of Cool Stars and High Obliquity for Hot Stars. *The Astrophysical Journal 801*(1), 3.

McLaughlin, D. B. (1924, Jul). Some results of a spectrographic study of the Algol system. *The Astrophysical Journal 60*, 22–31.

Murray, C. D. and A. C. M. Correia (2010). Keplerian Orbits and Dynamics of Exoplanets. In S. Seager (Ed.), *Exoplanets, edited by S. Seager. Tucson, AZ: University of Arizona Press, 2010, 526 pp. ISBN 978-0-8165-2945-2., p.15-23*, pp. 15–23.

Mustill, A. J., M. B. Davies, and A. Johansen (2015, July). The Destruction of Inner Planetary Systems during High-eccentricity Migration of Gas Giants. *The Astrophysical Journal 808*, 14.

Naoz, S. (2016, Sep). The Eccentric Kozai-Lidov Effect and Its Applications. *Annual Review of Astronomy and Astrophysics 54*, 441–489.

Naoz, S., W. M. Farr, Y. Lithwick, F. A. Rasio, and J. Teyssandier (2011, May). Hot Jupiters from secular planet-planet interactions. *Nature 473*(7346), 187–189.

Nelson, B. E., E. B. Ford, and F. A. Rasio (2017, Sep). Evidence for Two Hot-Jupiter Formation Paths. *The Astronomical Journal 154*(3), 106.

Nelson, R. P. (2018). Planetary Migration in Protoplanetary Disks. In *Handbook of Exoplanets, ISBN 978-3-319-55332-0. Springer International Publishing AG, part of Springer Nature, 2018, id.139*, pp. 139.

Newton, I. (1713). *The Principia.*

Noguchi, K., W. Aoki, S. Kawanomoto, H. Ando, S. Honda, H. Izumiura, E. Kambe, K. Okita, K. Sadakane, B. Sato, A. Tajitsu, T. Takada-Hidai, W. Tanaka, E. Watanabe, and M. Yoshida (2002, December). High Dispersion Spectrograph (HDS) for the Subaru Telescope. *The Publications of the Astronomical Society of Japan 54*, 855–864.

Ohta, Y., A. Taruya, and Y. Suto (2005, Apr). The Rossiter-McLaughlin Effect and Analytic Radial Velocity Curves for Transiting Extrasolar Planetary Systems. *The Astrophysical Journal 622*(2), 1118–1135.

Otor, O. J., B. T. Montet, J. A. Johnson, D. Charbonneau, A. Collier-Cameron, A. W. Howard, H. Isaacson, D. W. Latham, M. Lopez-Morales, and C. Lovis (2016, Dec). The Orbit and Mass of the Third Planet in the Kepler-56 System. *The Astronomical Journal 152*(6), 165.

Pepe, F., M. Mayor, F. Galland, D. Naef, D. Queloz, N. C. Santos, S. Udry, and M. Burnet (2002, June). The CORALIE survey for southern extra-solar planets VII. Two short- period Saturnian companions to <ASTROBJ>HD 108147</ASTROBJ> and <ASTROBJ>HD 168746</ASTROBJ>. *Astronomy & Astrophysics 388*, 632–638.

Pepper, J., R. W. Pogge, D. L. DePoy, J. L. Marshall, K. Z. Stanek, A. M. Stutz, S. Poindexter, R. Siverd, T. P. O'Brien, M. Trueblood, and P. Trueblood (2007, August). The Kilodegree Extremely Little Telescope (KELT): A Small Robotic Telescope for Large-Area Synoptic Surveys. *The Publications of the Astronomical Society of the Pacific 119*, 923–935.

Petrovich, C. (2015, May). Hot Jupiters from Coplanar High-eccentricity Migration. *The Astrophysical Journal 805*(1), 75.

Petrovich, C. and S. Tremaine (2016, Oct). Warm Jupiters from Secular Planet-Planet Interactions. *The Astrophysical Journal 829*(2), 132.

Petrovich, C., S. Tremaine, and R. Rafikov (2014, May). Scattering Outcomes of Close-in Planets: Constraints on Planet Migration. *The Astrophysical Journal 786*(2), 101.

Pietrinferni, A., S. Cassisi, M. Salaris, and F. Castelli (2004, September). A Large Stellar Evolution Database for Population Synthesis Studies. I. Scaled Solar Models and Isochrones. *The Astrophysical Journal 612*, 168–190.

Pollacco, D. L., I. Skillen, A. Collier Cameron, D. J. Christian, C. Hellier, J. Irwin, T. A. Lister, R. A. Street, R. G. West, D. R. Anderson, W. I. Clarkson, H. Deeg, B. Enoch, A. Evans, A. Fitzsimmons, C. A. Haswell, S. Hodgkin, K. Horne, S. R. Kane, F. P. Keenan, P. F. L. Maxted, A. J. Norton, J. Osborne, N. R. Parley, R. S. I. Ryans, B. Smalley, P. J. Wheatley, and D. M. Wilson (2006, October). The WASP Project and the SuperWASP Cameras. *The Publications of the Astronomical Society of the Pacific 118*, 1407–1418.

Pollack, J. B., O. Hubickyj, P. Bodenheimer, J. J. Lissauer, M. Podolak, and Y. Greenzweig (1996, Nov). Formation of the Giant Planets by Concurrent Accretion of Solids and Gas. *Icarus 124*(1), 62–85.

Pu, B. and D. Lai (2018, July). Eccentricities and inclinations of multiplanet systems with external perturbers. *Monthly Notices of the Royal Astronomical Society 478*, 197–217.

Queloz, D., A. Eggenberger, M. Mayor, C. Perrier, J. L. Beuzit, D. Naef, J. P. Sivan, and S. Udry (2000, Jul). Detection of a spectroscopic transit by the planet orbiting the star HD209458. *Astronomy & Astrophysics 359*, L13–L17.

Queloz, D., G. W. Henry, J. P. Sivan, S. L. Baliunas, J. L. Beuzit, R. A. Donahue, M. Mayor, D. Naef, C. Perrier, and S. Udry (2001, November). No planet for HD 166435. *Astronomy & Astrophysics 379*, 279–287.

Rafikov, R. R. (2006, September). Atmospheres of Protoplanetary Cores: Critical Mass for Nucleated Instability. *The Astrophysical Journal 648*, 666–682.

Rasio, F. A. and E. B. Ford (1996, Nov). Dynamical instabilities and the formation of extrasolar planetary systems. *Science 274*, 954–956.

Reiners, A. and G. Basri (2010, Feb). A Volume-Limited Sample of 63 M7-M9.5 Dwarfs. II. Activity, Magnetism, and the Fade of the Rotation-Dominated Dynamo. *The Astrophysical Journal 710*(2), 924–935.

Rice, W. K. M., P. J. Armitage, and D. F. Hogg (2008, Mar). Why are there so few hot Jupiters? *Monthly Notices of the Royal Astronomical Society 384*(3), 1242–1248.

Ricker, G. R., J. N. Winn, R. Vanderspek, D. W. Latham, G. Á. Bakos, J. L. Bean, Z. K. Berta-Thompson, T. M. Brown, L. Buchhave, N. R. Butler, R. P. Butler, W. J. Chaplin, D. Charbonneau, J. Christensen-Dalsgaard, M. Clampin, D. Deming, J. Doty, N. De Lee, C. Dressing, E. W. Dunham, M. Endl, F. Fressin, J. Ge, T. Henning, M. J. Holman, A. W. Howard, S. Ida, J. M. Jenkins, G. Jernigan, J. A. Johnson, L. Kaltenegger, N. Kawai, H. Kjeldsen, G. Laughlin, A. M. Levine, D. Lin, J. J. Lissauer, P. MacQueen, G. Marcy, P. R. McCullough, T. D. Morton, N. Narita, M. Paegert, E. Palle, F. Pepe, J. Pepper, A. Quirrenbach, S. A. Rinehart, D. Sasselov, B. Sato, S. Seager, A. Sozzetti, K. G. Stassun, P. Sullivan, A. Szentgyorgyi, G. Torres, S. Udry, and J. Villasenor (2015, January). Transiting Exoplanet Survey Satellite (TESS). *Journal of Astronomical Telescopes, Instruments, and Systems 1*(1), 014003.

Robert, C. M. T., A. Crida, E. Lega, H. Méheut, and A. Morbidelli (2018, Sep). Toward a new paradigm for Type II migration. *Astronomy & Astrophysics 617*, A98.

Robin, A. C., C. Reylé, S. Derrière, and S. Picaud (2003, October). A synthetic view on structure and evolution of the Milky Way. *Astronomy & Astrophysics 409*, 523–540.

Rodriguez, J. E., J. D. Eastman, G. Zhou, S. N. Quinn, T. G. Beatty, and K. Penev (2019, June). KELT-24b: A 5MJ Planet on a 5.6 day Well-Aligned Orbit around the Young V=8.3 F-star HD 93148. *arXiv e-prints*.

Rossiter, R. A. (1924, Jul). On the detection of an effect of rotation during eclipse in the velocity of the brigher component of beta Lyrae, and on the constancy of velocity of this system. *The Astrophysical Journal 60*, 15–21.

Rucinski, S. M. (2002, Sep). Radial Velocity Studies of Close Binary Stars. VII. Methods and Uncertainties. *The Astronomical Journal 124*(3), 1746–1756.

Safronov, V. S. (1972). *Evolution of the protoplanetary cloud and formation of the earth and planets.*

Sanchis-Ojeda, R., J. N. Winn, M. J. Holman, J. A. Carter, D. J. Osip, and C. I. Fuentes (2011, Jun). Starspots and Spin-orbit Alignment in the WASP-4 Exoplanetary System. *The Astrophysical Journal 733*(2), 127.

Santerne, A., C. Moutou, M. Tsantaki, F. Bouchy, G. Hébrard, V. Adibekyan, J. M. Almenara, L. Amard, S. C. C. Barros, I. Boisse, A. S. Bonomo, G. Bruno, B. Courcol, M. Deleuil, O. Demangeon, R. F. Díaz, T. Guillot, M. Havel, G. Montagnier, A. S. Rajpurohit, J. Rey, and N. C. Santos (2016, Mar). SOPHIE velocimetry of Kepler transit candidates. XVII. The physical properties of giant exoplanets within 400 days of period. *Astronomy & Astrophysics 587*, A64.

Sato, B., E. Kambe, Y. Takeda, H. Izumiura, and H. Ando (2002, Dec). Development of Iodine Cells for the Subaru HDS and the Okayama HIDES: II. New Software for Precise Radial Velocity Measurements. *The Publications of the Astronomical Society of Japan 54*, 873–882.

Schwarz, R., B. Funk, R. Zechner, and Á. Bazsó (2016, August). New prospects for observing and cataloguing exoplanets in well-detached binaries. *Monthly Notices of the Royal Astronomical Society 460*, 3598–3609.

Seager, S. and J. J. Lissauer (2010). Introduction to Exoplanets. In S. Seager (Ed.), *Exoplanets, edited by S. Seager. Tucson, AZ: University of Arizona Press, 2010, 526 pp. ISBN 978-0-8165-2945-2., p.3-13*, pp. 3–13.

Silva Aguirre, V., G. R. Davies, S. Basu, J. Christensen-Dalsgaard, O. Creevey, T. S. Metcalfe, T. R. Bedding, L. Casagrande, R. Handberg, M. N. Lund, P. E. Nissen, W. J. Chaplin, D. Huber, A. M. Serenelli, D. Stello, V. Van Eylen, T. L. Campante, Y. Elsworth, R. L. Gilliland, S. Hekker, C. Karoff, S. D. Kawaler, H. Kjeldsen, and M. S. Lundkvist (2015, September). Ages and fundamental properties of Kepler exoplanet host stars from asteroseismology. *Monthly Notices of the Royal Astronomical Society 452*, 2127–2148.

Snellen, I. A. G., R. J. de Kok, E. J. W. de Mooij, and S. Albrecht (2010, June). The orbital motion, absolute mass and high-altitude winds of exoplanet HD209458b. *Nature 465*, 1049–1051.

Spalding, C. and K. Batygin (2015, Oct). Magnetic Origins of the Stellar Mass-Obliquity Correlation in Planetary Systems. *The Astrophysical Journal 811*(2), 82.

Stapelfeldt, K. R., J. E. Krist, F. Ménard, J. Bouvier, D. L. Padgett, and C. J. Burrows (1998, Jul). An Edge-On Circumstellar Disk in the Young Binary System HK Tauri. *The Astrophysical Journal 502*(1), L65–L69.

Struve, O. (1952, Oct). Proposal for a project of high-precision stellar radial velocity work. *The Observatory 72*, 199–200.

Talens, G. J. J., S. Albrecht, J. F. P. Spronck, A. L. Lesage, G. P. P. L. Otten, R. Stuik, V. Van Eylen, H. Van Winckel, D. Pollacco, J. McCormac, F. Grundahl, M. Fredslund Andersen, V. Antoci, and I. A. G. Snellen (2017, Oct). MASCARA-1 b. A hot Jupiter transiting a bright $m_V = 8.3$ A-star in a misaligned orbit. *Astronomy & Astrophysics 606*, A73.

Talens, G. J. J., E. R. Deul, R. Stuik, O. Burggraaff, A. L. Lesage, J. F. P. Spronck, S. N. Mellon, J. I. Bailey, E. E. Mamajek, M. A. Kenworthy, and I. A. G. Snellen (2018, Nov). Data calibration for the MASCARA and bRing instruments. *Astronomy and Astrophysics 619*, A154.

Talens, G. J. J., A. B. Justesen, S. Albrecht, J. McCormac, V. Van Eylen, G. P. P. L. Otten, F. Murgas, E. Palle, D. Pollacco, R. Stuik, J. F. P. Spronck, A.-L. Lesage, F. Grundahl, M. Fredslund Andersen, V. Antoci, and I. A. G. Snellen (2018, April). MASCARA-2 b. A hot Jupiter transiting the $m_V = 7.6$ A-star HD 185603. *Astronomy & Astrophysics 612*, A57.

Talens, G. J. J., J. F. P. Spronck, A.-L. Lesage, G. P. P. L. Otten, R. Stuik, D. Pollacco, and I. A. G. Snellen (2017, May). The Multi-site All-Sky CAmeRA (MASCARA). Finding transiting exoplanets around bright ($m_V < 8$) stars. *Astronomy & Astrophysics 601*, A11.

Telting, J. H., G. Avila, L. Buchhave, S. Frandsen, D. Gandolfi, B. Lindberg, H. C. Stempels, S. Prins, and NOT staff (2014, January). FIES: The high-resolution Fiber-fed Echelle Spectrograph at the Nordic Optical Telescope. *Astronomische Nachrichten 335*, 41.

Thorngren, D. P., J. J. Fortney, R. A. Murray-Clay, and E. D. Lopez (2016, November). The Mass-Metallicity Relation for Giant Planets. *The Astrophysical Journal 831*, 64.

Torres, G. (2010, November). On the Use of Empirical Bolometric Corrections for Stars. *The Astronomical Journal 140*, 1158–1162.

Triaud, A. H. M. J. (2018). The Rossiter-McLaughlin Effect in Exoplanet Research. In *Handbook of Exoplanets, ISBN 978-3-319-55332-0. Springer International Publishing AG, part of Springer Nature, 2018, id.2*, pp. 1375–1401.

Triaud, A. H. M. J., A. Collier Cameron, D. Queloz, D. R. Anderson, M. Gillon, L. Hebb, C. Hellier, B. Loeillet, P. F. L. Maxted, M. Mayor, F. Pepe, D. Pollacco, D. Ségransan, B. Smalley, S. Udry, R. G. West, and P. J. Wheatley (2010, Dec). Spin-orbit angle measurements for six southern transiting planets. New insights into the dynamical origins of hot Jupiters. *Astronomy & Astrophysics 524*, A25.

Valenti, J. A. and D. A. Fischer (2005, Jul). Spectroscopic Properties of Cool Stars (SPOCS). I. 1040 F, G, and K Dwarfs from Keck, Lick, and AAT Planet Search Programs. *The Astrophysical Journal Supplement Series 159*(1), 141–166.

Van Eylen, V., C. Agentoft, M. S. Lundkvist, H. Kjeldsen, J. E. Owen, B. J. Fulton, E. Petigura, and I. Snellen (2018, October). An asteroseismic view of the radius valley: stripped cores, not born rocky. *Monthly Notices of the Royal Astronomical Society 479*, 4786–4795.

Van Eylen, V. and S. Albrecht (2015, Aug). Eccentricity from Transit Photometry: Small Planets in Kepler Multi-planet Systems Have Low Eccentricities. *The Astrophysical Journal 808*(2), 126.

Van Eylen, V., S. Albrecht, X. Huang, M. G. MacDonald, R. I. Dawson, M. X. Cai, D. Foreman-Mackey, M. S. Lundkvist, V. Silva Aguirre, I. Snellen, and J. N. Winn (2019, Feb). The Orbital Eccentricity of Small Planet Systems. *The Astronomical Journal 157*(2), 61.

Van Eylen, V., F. Dai, S. Mathur, D. Gandolfi, S. Albrecht, M. Fridlund, R. A. García, E. Guenther, M. Hjorth, A. B. Justesen, J. Livingston, M. N. Lund, F. Pérez Hernández, J. Prieto-Arranz, C. Regulo, L. Bugnet, M. E. Everett, T. Hirano, D. Nespral, G. Nowak, E. Palle, V. Silva Aguirre, T. Trifonov, J. N. Winn, O. Barragán, P. G. Beck, W. J. Chaplin, W. D. Cochran, S. Csizmadia, H. Deeg, M. Endl, P. Heeren, S. Grziwa, A. P. Hatzes, D. Hidalgo, J. Korth, S. Mathis, P. Montañes Rodriguez, N. Narita, M. Patzold, C. M. Persson, F. Rodler, and A. M. S. Smith (2018, August). HD 89345: a bright oscillating star hosting a transiting warm Saturn- sized planet observed by K2. *Monthly Notices of the Royal Astronomical Society 478*, 4866–4880.

Vanderburg, A. and J. A. Johnson (2014, October). A Technique for Extracting Highly Precise Photometry for the Two-Wheeled Kepler Mission. *The Publications of the Astronomical Society of the Pacific 126*, 948.

Weiss, L. M. and G. W. Marcy (2014, March). The Mass-Radius Relation for 65 Exoplanets Smaller than 4 Earth Radii. *The Astrophysical Journal Letters 783*, L6.

Winn, J. N. (2010). Exoplanet Transits and Occultations. In S. Seager (Ed.), *Exoplanets, edited by S. Seager. Published by University of Arizona Press, Tucson, AZ, 2010, 526 pp. ISBN 978-0-8165-2945-2., p.55-77*, pp. 55–77.

Winn, J. N., D. Fabrycky, S. Albrecht, and J. A. Johnson (2010, Aug). Hot Stars with Hot Jupiters Have High Obliquities. *The Astrophysical Journal Letters 718*(2), L145–L149.

Winn, J. N., J. A. Johnson, A. W. Howard, G. W. Marcy, H. Isaacson, A. Shporer, G. Á. Bakos, J. D. Hartman, and S. Albrecht (2010, Nov). The Oblique Orbit of the Super-Neptune HAT-P-11b. *The Astrophysical Journal Letters 723*(2), L223–L227.

Winn, J. N., R. W. Noyes, M. J. Holman, D. Charbonneau, Y. Ohta, A. Taruya, Y. Suto, N. Narita, E. L. Turner, J. A. Johnson, G. W. Marcy, R. P. Butler, and S. S. Vogt (2005, Oct). Measurement of Spin-Orbit Alignment in an Extrasolar Planetary System. *The Astrophysical Journal 631*(2), 1215–1226.

Wolszczan, A. and D. A. Frail (1992, Jan). A planetary system around the millisecond pulsar PSR1257 + 12. *Nature 355*(6356), 145–147.

Wu, Y. and Y. Lithwick (2011, Jul). Secular Chaos and the Production of Hot Jupiters. *The Astrophysical Journal 735*(2), 109.

Wu, Y. and N. Murray (2003, May). Planet Migration and Binary Companions: The Case of HD 80606b. *The Astrophysical Journal 589*(1), 605–614.

Yee, S. W., E. A. Petigura, and K. von Braun (2017, February). Precision Stellar Characterization of FGKM Stars using an Empirical Spectral Library. *The Astrophysical Journal 836*, 77.

Zahn, J. P. (1977, May). Reprint of 1977A&A....57..383Z. Tidal friction in close binary stars. *Astronomy & Astrophysics 500*, 121–132.

Zanazzi, J. J. and D. Lai (2018a, July). Effects of disc warping on the inclination evolution of star-disc-binary systems. *Monthly Notices of the Royal Astronomical Society 477*, 5207–5219.

Zanazzi, J. J. and D. Lai (2018b, Jul). Planet formation in discs with inclined binary companions: can primordial spin-orbit misalignment be produced? *Monthly Notices of the Royal Astronomical Society 478*(1), 835–851.

Zechmeister, M. and M. Kürster (2009, March). The generalised Lomb-Scargle periodogram. A new formalism for the floating-mean and Keplerian periodograms. *Astronomy & Astrophysics 496*, 577–584.

Zuckerman, B. (2015, Jun). Recognition of the First Observational Evidence of an Extrasolar Planetary System. In P. Dufour, P. Bergeron, and G. Fontaine (Eds.), *19th European Workshop on White Dwarfs*, Volume 493 of *Astronomical Society of the Pacific Conference Series*, pp. 291.